INFORMATION TO USERS

This manuscript has been reproduced from the microfilm master. UMI films the text directly from the original or copy submitted. Thus, some thesis and dissertation copies are in typewriter face, while others may be from any type of computer printer.

The quality of this reproduction is dependent upon the quality of the copy submitted. Broken or indistinct print, colored or poor quality illustrations and photographs, print bleedthrough, substandard margins, and improper alignment can adversely affect reproduction.

In the unlikely event that the author did not send UMI a complete manuscript and there are missing pages, these will be noted. Also, if unauthorized copyright material had to be removed, a note will indicate the deletion.

Oversize materials (e.g., maps, drawings, charts) are reproduced by sectioning the original, beginning at the upper left-hand corner and continuing from left to right in equal sections with small overlaps.

ProQuest Information and Learning
300 North Zeeb Road, Ann Arbor, MI 48106-1346 USA
800-521-0600

ASYMMETRIC MULTIPLE QUANTUM WELL LASERS

By

MICHAEL JAMES HAMP, B. Sc. Engineering Physics

A Thesis

Submitted to the School of Graduate Studies

in partial fulfilment of the requirements

for the degree

Doctor of Philosophy

McMaster University

DOCTOR OF PHILOSOPHY (2000) McMASTER UNIVERSITY

(Engineering Physics) Hamilton, Ontario

TITLE: Asymmetric Multiple Quantum Well Lasers

AUTHOR: Michael James Hamp, B.Sc. Engineering Physics (University of Alberta)

SUPERVISOR: Professor Daniel T. Cassidy

NUMBER OF PAGES: 149

Abstract

Asymmetric Multiple Quantum Well (AMQW) lasers have wells of varying thickness and/or composition within a single active region. The different wells emit at different wavelengths. The thesis begins with a description of the basic properties of AMQW lasers which have been discovered through experimentation. Next, an experimental technique is introduced which employs AMQW lasers to study experimentally the non-uniform carrier distribution in MQW lasers. Results of three studies carried out using this new technique are presented. A theoretical model is developed to explain some of our experimental results. The theoretical treatment of carrier capture and carrier escape is discussed in detail and different treatments are compared to experimental data taken from AMQW lasers. Finally, the application of AMQW lasers as broadly tunable lasers is discussed and the key design issues for designing broadly tunable AMQW lasers are presented.

Acknowledgments

The past four years have been a wonderful time of learning for me. I would like to thank the following people for helping me through this endeavor.

- Dan Cassidy, my supervisor. Dan foresaw the potential of AMQW lasers both as broadly tunable lasers and as a probe for studying the physics of MQW active regions. Dr. Cassidy's daily visits to the lab enable him to lend his experience and insight to the smallest details of his students' work. As a result Dr. Cassidy has made contributions to every aspect of this thesis. Dan is an outstanding graduate supervisor and a role model of the highest caliber. Thank you for the countless discussions. It was a pleasure.

- My colleagues who contributed directly to the work presented in this thesis. Xiang Zhu for initiating our group's interest in AMQW lasers and mentoring me when I started working in the lab. Q.C. Zhao for teaching me the art of processing devices and taking the photoluminescence data that appears in chapter 3. Brad Robinson for teaching me the critical growth considerations involved in designing devices. Dave Thompson and Brad Robinson who made this work possible by growing the AMQW wafers using McMaster's MBE facility. Mike Davies for the use of Lastip and his facilities at NRC as well as John Bewsher for processing and testing broad area devices at NRC.

- My lab mates who have made life in the sub-basement bareable, even fun. Sean Woodworth, the first friend I made in Hamilton. Thank you for filling my head with songs. Gord Morrison, my roomate, labmate, stopper, fellow cyclist, fellow skier... There is too much to say. Thank you for everything. Everything except the bagpipes. Dave Deforge, for being really tall

and friendly and patient enough to work through my code. An Nguyen for answering countless questions about my experimental aparatus and Hu Wang for the company.

- All my friends who made the past four years so interesting and fun. Special thanks to Mike O'Brien, Denis Germain, Brian Schaly (TBG), John Hazell, Sara Ednie, Sandra Janosik, Erin Niven, Horatiu Pop, Bill DaSilva, Marcy Lumsden, Jamal and Sabina, Peter and Doris. So many good times. Thank you Rachid OUYED for inspiring and encouraging me. You are a true intellectual and teacher. Thank you Kassia Johnson for putting up with me and making the past few months so enjoyable. Thank you Mike and Jen. You have been with me through my toughest times and my best. You are family.

- Sensei Phil McColl for starting me on the path to becoming a martial artist and contributing greatly to my learning experience at McMaster.

- Richard Feynman for writing his Lectures on Physics and explaining things to me.

- There is noone in the world like family. I'd like to thank my family here in Ontario who made this place so far from home feel not so far from home. My brother and sisters in Alberta who have supported me and looked out for me my whole life. Thank you Cathy, Diane, Dean and all your families. Lastly, thank you Dad for supporting me unconditionally, for holding education in such high regard, and for ingraining in me the love of knowledge – philosophy.

Dedication

The past four years of work, summarized in this thesis, are dedicated to the memory of my mom.

Elizabeth Lillian Hamp

(1939 – 1995)

Table of Contents

Table of Figures

1. CHAPTER 1 - INTRODUCTION

1.1 Introduction to Asymmetric Multiple Quantum Well Lasers

The problem of a particle trapped in a potential well is one of the elementary concepts of quantum mechanics and is discussed in most introductory quantum mechanics text books and university courses [1,2]. Quantum wells (QWs) play an integral role in the quantum mechanical description of the universe. Atoms are three dimensional quantum wells and the structure and behaviour of atoms can only be fully understood by studying the problem of QWs. The potential profile and energy levels of a one dimensional QW are shown in Fig. 1-1. A quantum well has discrete energy levels because only particles with certain energies can satisfy the Schrödinger equation at every location in space and time; a fundamental requirement of the laws of physics.

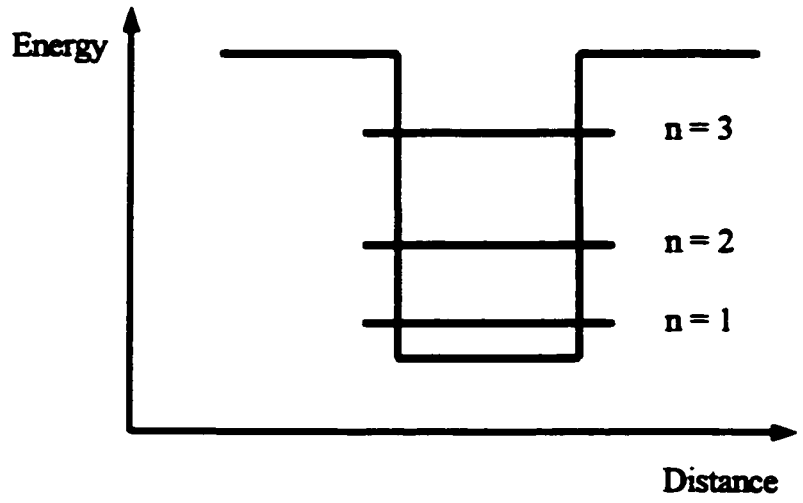

Fig. 1-1 A quantum mechanical potential well and its allowed energy levels.

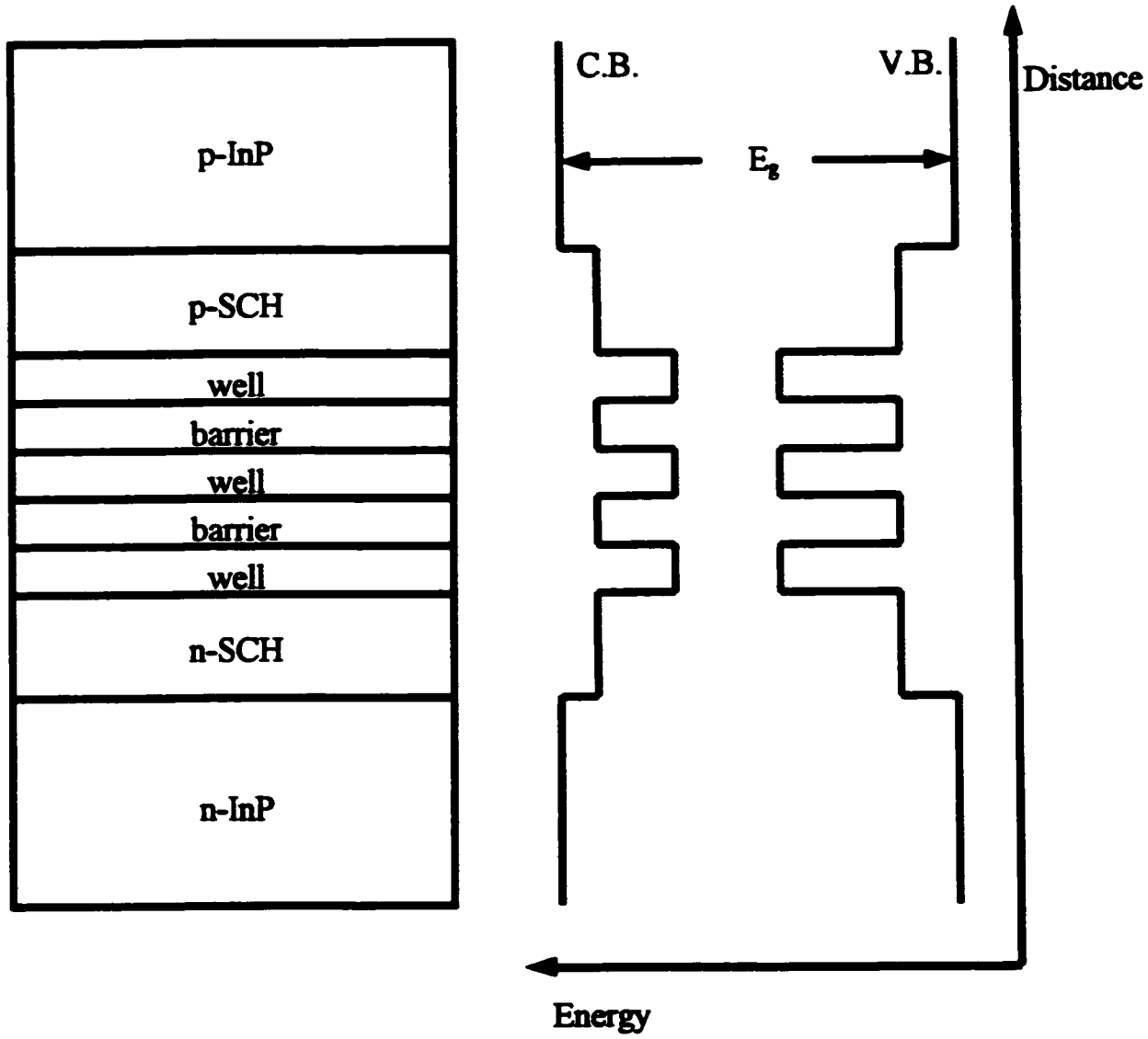

Fig. 1-2 Layer structure and corresponding energy band diagram for a typical multiple quantum well laser.

In the early to mid 1970s it was discovered that a quantum mechanical potential well could be constructed in semiconductor material by sandwiching a thin layer of low bandgap material between layers of high bandgap material. The band gap is changed by changing the composition of the material. Shortly after the first experimental realization of semiconductor QWs they were used to make quantum well semiconductor lasers. A review of this early work is given by C. Henry in chapter 1 of the text edited by Zory [3]. The layer structure and band diagram of a typical multiple quantum well (MQW) semiconductor diode laser structure are shown in Fig. 1-2.

Several quantum well layers of low energy gap are separated by quantum barrier layers of high energy gap. The wells and barriers make up the MQW active region. Above and below the active region are the separate confinement heterostructure (SCH) layers which form a vertical optical waveguide so that the laser light remains single mode in the vertical direction. For background information on the operation of lasers see [4] and for information on semiconductor diode lasers see [5].

As can be seen in Fig. 1-2, QWs are formed in the valence band and in the conduction band of a QW laser. Light is produced in a QW when an electron in an energy level of the conduction band QW recombines with a hole in the same energy level (i.e., n = 1) of the valence band QW as shown in Fig. 1-3. For a description of the production of light in a QW see chapter 2 of [3].

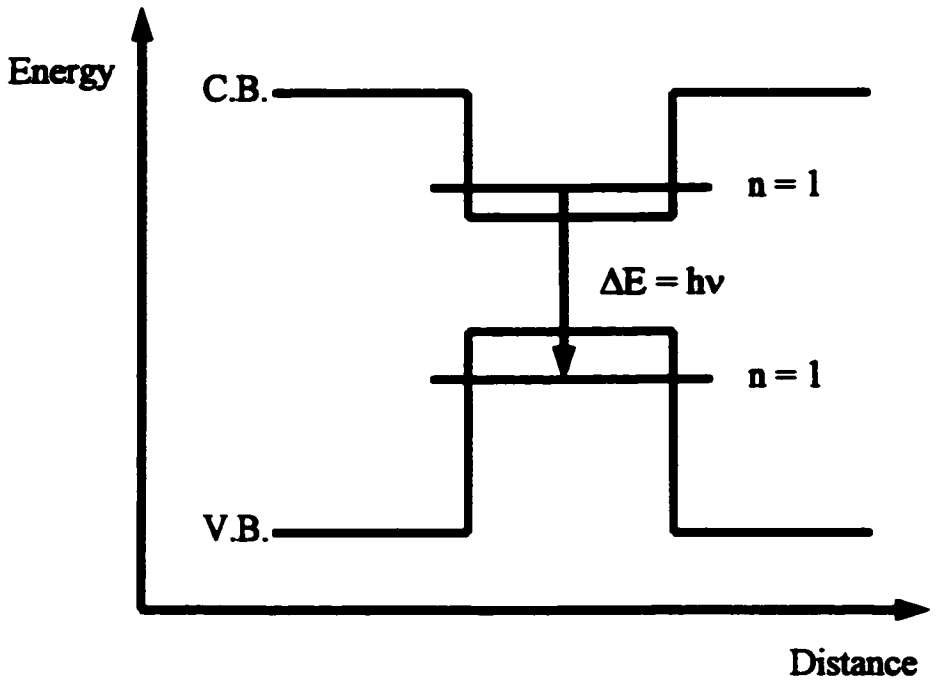

Fig. 1-3 Optical transition across the energy gap of a QW.

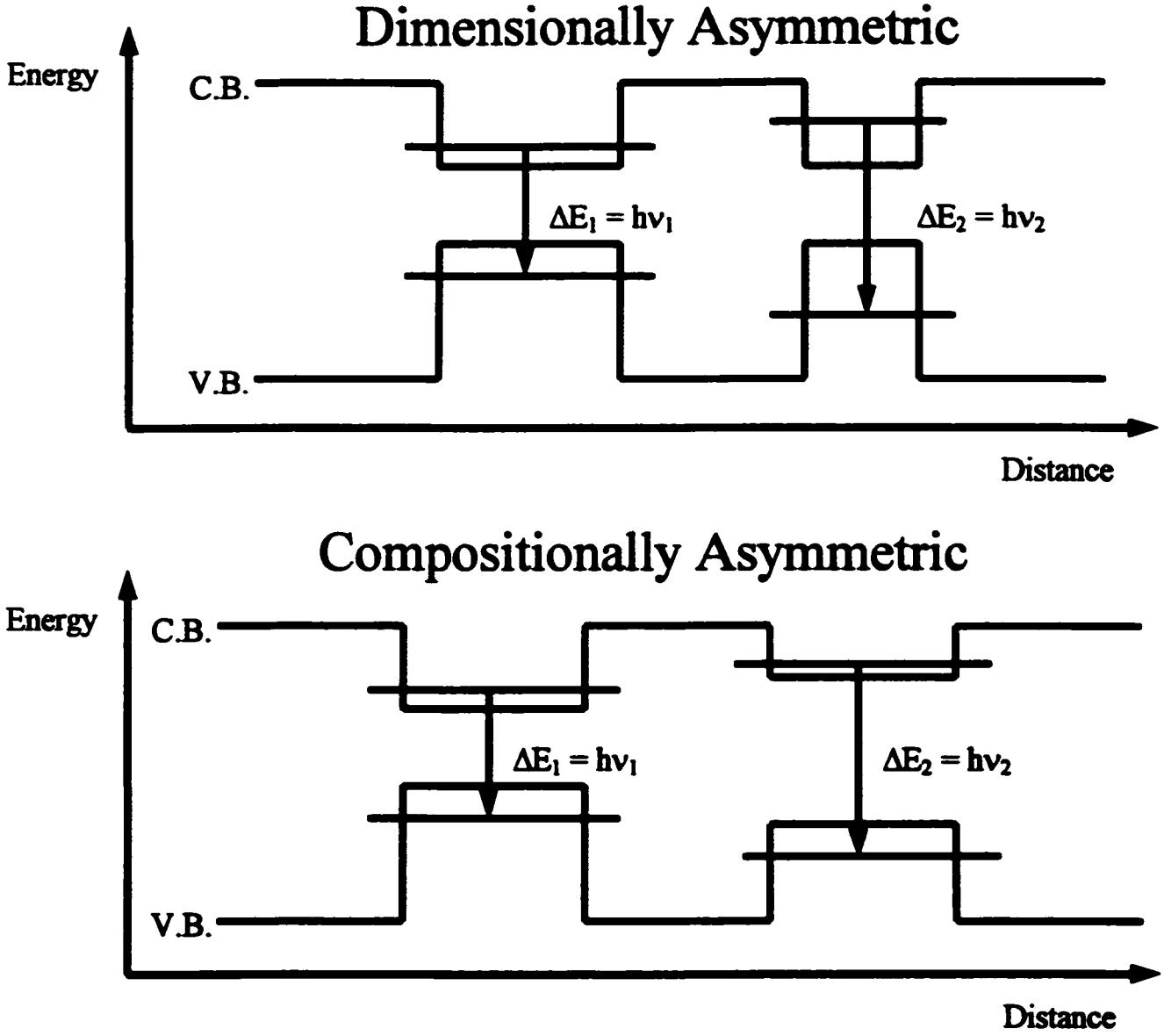

Fig. 1-4 Dimensionally and compositionally asymmetric multiple quantum well lasers.

The wavelengths of the optical transitions in a QW are primarily determined by the bandgap of the QW material (or composition of the QW) and the thickness of the QW. Asymmetric multiple quantum well (AMQW) lasers have QWs of different thicknesses and/or compositions in the same active region. I have defined AMQW devices with QWs of varying thickness as *dimensionally asymmetric* MQW (DAMQW) devices and AMQW devices with QWs of varying composition as *compositionally asymmetric* MQW (CAMQW) devices. Schematics of DAMQW and CAMQW active regions are shown in Fig. 1-4.

The QWs of different thickness and/or composition generally emit at different wavelengths which makes AMQW lasers of interest for two key reasons. First, they are potentially well suited to a variety of applications, and second, they may be used to study the physics of MQW laser operation. The different QWs in an AMQW structure contribute gain at different wavelengths and can, if designed properly, exhibit a broad gain peak. Broad gain peak lasers have applications such as broadly tunable lasers, mode locked ultra-short pulse lasers, and low temperature dependence distributed feedback (DFB) lasers. The spontaneous emission profile of AMQW lasers also has a broad spectral width and AMQW light emitting diodes (LEDs) or superluminescent diodes (SLDs) may be useful in applications which require a broadly emitting source.

AMQW lasers are also useful for studying the underlying physics of MQW laser operation. The different thickness or composition QWs emit at different wavelengths and hence are distinguishable. The relative rates of emission from the QWs of different thickness or composition can be measured experimentally. This feature of AMQW lasers can be used to study experimentally dependencies on position in the active region, QW thickness, and QW composition.

1.2 Literature Review of AMQW Lasers

In this section I present a chronological review of the published work on AMQW lasers. The published literature on AMQW lasers can be broken into two time periods. A series of papers were published on AMQW lasers between 1989 and 1992. The interest in AMQW lasers was renewed in 1996 and many papers have appeared in the past four years.

The first AMQW laser was reported by Ikeda *et al.* in 1989 [6]. In a series of papers Ikeda's group described the operating characteristics of two different AlGaAs AMQW structures each consisting of two quantum wells of different thicknesses and different compositions separated by a high, thick barrier layer [6-8]. They reported wavelength switching from one quantum well to another, simultaneous lasing on both quantum wells, and quasicontinuous tuning over a 22 nm range using split contact devices. These experimental papers were followed by two theoretical papers [9,10] published in 1991 and 1992 in which the lasers were modeled using a rate equation approach. In 1992 Evans *et. al.* [11] compared two mirror image AlGaAs AMQW structures for the purpose of studying the effects of the non-uniform carrier distribution. They studied their structures at a single cavity length.

The past few years have seen a renewed interest in AMQW lasers beginning with a theoretical paper by Huang *et. al.* in June 1996 [12]. Huang *et. al.* [12] theoretically studied the carrier capture competition between two QWs of different thickness using a phenomenological rate equation model and without comparing to experimental data. In February 1997 Gingrich *et. al.* [13] were the first to exploit the potential of AMQW lasers as broadly tunable lasers. Gingrich *et al.* [13] were able to wavelength tune an InGaAs/AlGaAs AMQW laser in a Littrow configuration external cavity over an 80 nm range. In March 1997 Kononenko *et. al.* [14] published a theoretical paper studying the gain and spontaneous emission spectra of an AMQW structure and predicted broad spectral properties. In May 1997 Krauss *et al.* [15] were able to wavelength tune a GaAs/AlGaAs AMQW laser over an 85 nm range using a grating external cavity. In August 1997 Yamazaki *et. al.* [16] compared two mirror image InGaAs/InGaAsP AMQW laser structures at a single cavity length to observe experimentally the effect of the non-uniform carrier distribution. In September 1997 Zhu *et. al.* [17] reported a 118 nm tuning range

using an InP/InGaAsP AMQW laser in a Littrow configuration external cavity. In March 1998 Lee *et al.* [18] reported a 90 nm tuning range using an InGaAs AMQW amplifier in a grating coupled ring external cavity.

At CLEO '98 both Hamp *et. al.* [19] and Lee *et. al.* [20] reported on mirror image AMQW structures showing the effect of the non-uniform carrier distribution. In October 1998 Hamp *et. al.* [21] introduced the concept of the transition cavity length and used it to perform a qualitative study of the non-uniform carrier distribution as a function of barrier height. In February 1999 Hamp *et. al.* [22] introduced the quantitative TCL method and used it to study the effect of the non-uniform carrier distribution on structures with different numbers of QWs. They also showed that comparing mirror image AMQW lasers at a single cavity length does not yield useful information about the non-uniform carrier distribution. In May 1999 Newell *et. al.* [23] compared mirror image AMQW structures at a single cavity length and measured the electroluminescence at different pump currents. In 1999 Kononenko *et. al.* [24] published a theoretical study of the tuning range of AMQW lasers. In February 2000 Hamp *et. al.* [25] used the quantitative TCL method to study the effect of barrier thickness on the non-uniform carrier distribution. In May 2000 Hamp *et. al.* [26] presented a physical explanation for the experimentally observed dependence of the non-uniform carrier distribution on barrier thickness. Also in May 2000 Wallace *et. al.* [27] presented the results of using an AMQW structure as the gain medium in a mode locked short pulse laser. In June 2000 Woodworth *et. al.* [28] were the first to demonstrate experimentally the use of an AMQW laser in trace gas detection applications. In August 2000 Hamp *et. al.* [29] provided a comprehensive experimental and theoretical study of the critical design parameters for producing broadly tunable AMQW lasers. Hamp *et. al.* [30]

have also presented an ambipolar rate equation and gain model which is capable of predicting the experimentally observed behaviour of 13 different AMQW laser structures.

1.3 Thesis Summary and Objectives

This thesis is organized into seven chapters. Chapter 2 introduces the general properties of AMQW lasers including the transition cavity length and the above threshold properties of AMQW devices at different cavity lengths and temperatures. Chapter 3 introduces the quantitative transition cavity length method for studying the non-uniform carrier distribution in MQW lasers using mirror image AMQW structures. The experimental results of three studies carried out using the transition cavity length method are presented. In chapter 4 an ambipolar rate equation and gain model is developed which is capable of predicting the experimentally observed dependence of the non-uniform carrier distribution on barrier thickness, a dependence that does not appear to be predicted by existing carrier transport models. The model is capable of fitting experimental data taken from thirteen different AMQW laser structures. Chapter 5 describes our treatment of the processes of carrier capture and carrier escape in a QW. The critical design parameters for making broadly tunable AMQW lasers are examined in Chapter 6. Chapter 7 contains a summary of the work reported in this thesis and a list of suggestion for future work.

2. CHAPTER 2 – PROPERTIES OF AMQW LASERS

2.1 Introduction

In this chapter the spectral properties of AMQW lasers are described. Several interesting and unique phenomena have been observed. These phenomena were exhibited by all of the AMQW structures grown and studied and hence are believed to be general properties of AMQW lasers.

The spectral properties of AMQW lasers vary strongly with cavity length. The first section of this chapter is devoted to defining and describing the transition cavity length (TCL). The spectral properties of AMQW lasers can be categorized with respect to the TCL. The remainder of the chapter examines the spectral behaviour of AMQW lasers. Fascinating above threshold spectral behavior has been observed for lasers with cavity lengths longer than the TCL but near the TCL. These lasers initially reach threshold on the thick QWs but with increasing current exhibit a large shift in wavelength towards the emission wavelength corresponding to the thin QWs. Increasing the current further causes the thin QWs to reach threshold and begin to lase; lasing on modes corresponding to both wells was observed. A transition from lasing on QWs of one thickness to QWs of another thickness was also observed with changing temperature. These phenomena were observed for c.w. and pulsed operation indicating that the effect is not thermal although it does have a temperature dependence. High speed measurements show that lasing on the thick wells and thin wells appears to occur simultaneously.

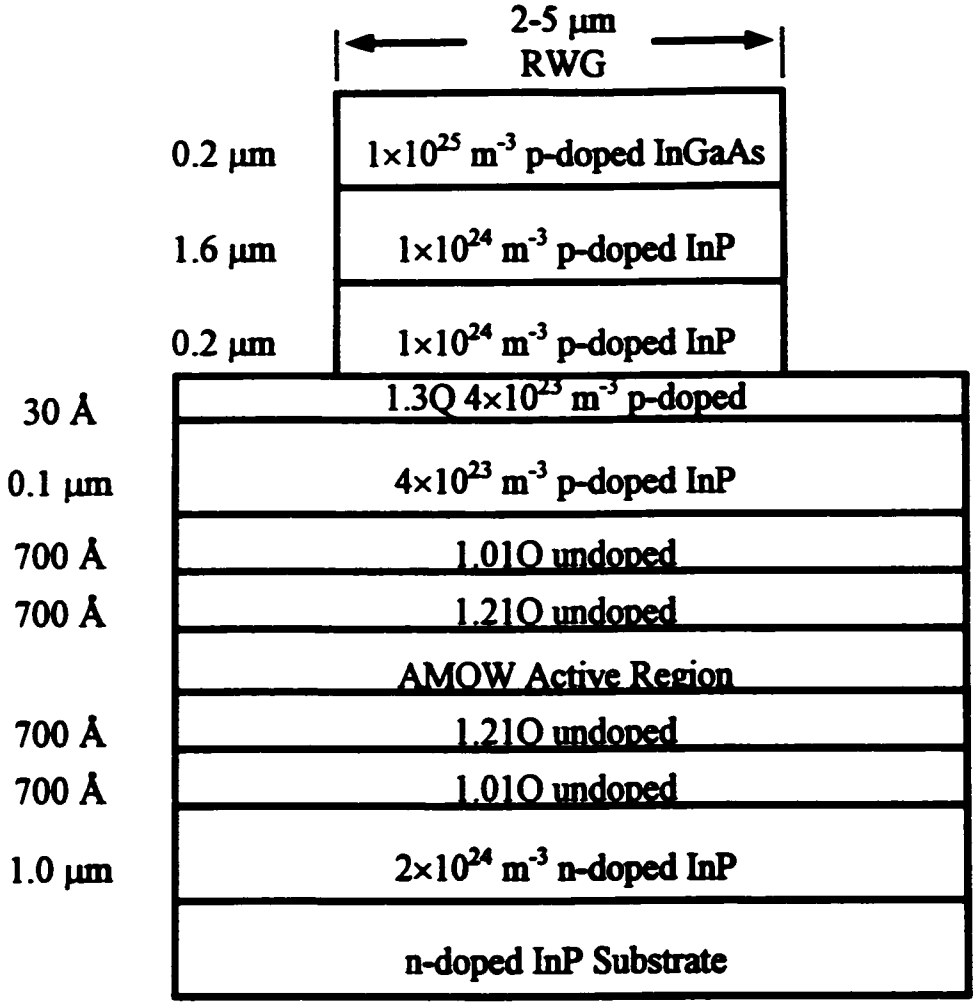

Fig. 2-1 Schematic of all laser structures. Each structure has a different active region.

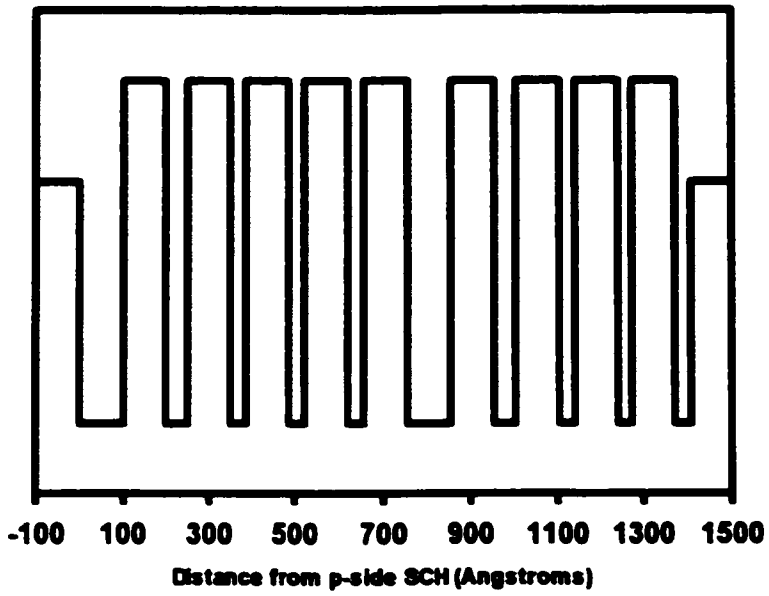

Fig. 2-2 Valence band energy diagram for the active region of structure 1.

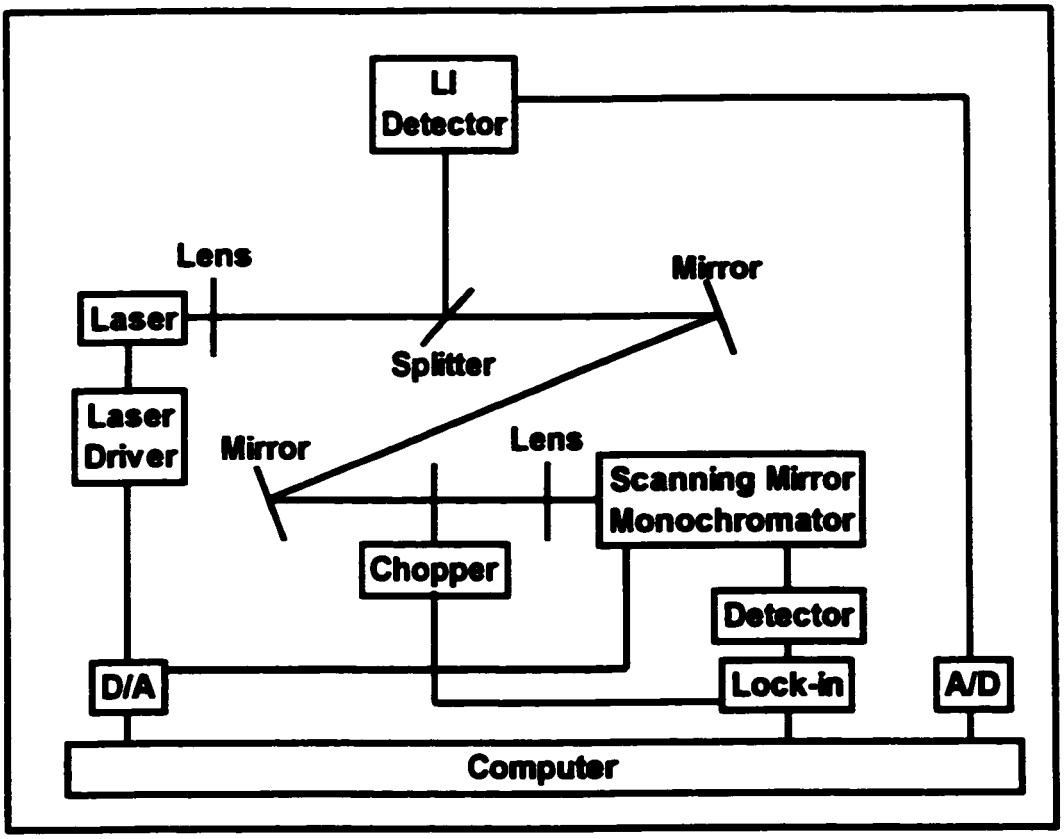

Fig. 2-3 Schematic of the experimental setup used to measure the spectra and LI curves of the devices.

2.2 Device Description and Experimental Setup

Thirteen different AMQW laser structures have been studied. The laser structures we have studied all have different active regions but are all set in the layer structure shown in Fig. 2-1. The characteristics described in this chapter have been observed in all of the AMQW laser structures we have grown but for convenience the behaviour of one structure is described in detail in this chapter. The structure studied in this chapter is labeled structure 1. The active region of structure 1 is shown schematically in Fig. 2-2. The structure contains two 100 Å wells, two 50 Å wells and six 35 Å wells of composition $In_{.775}Ga_{.225}As_{.780}P_{.220}$ separated by 100 Å barriers of composition $In_{.775}Ga_{.225}As_{.305}P_{.695}$. The QWs have 1 % compressive strain and the barriers have 0.6 % tensile strain. The structures were grown at McMaster University using gas source

molecular beam epitaxy. Layer thicknesses were controlled, for thin layers, to within ± 3 Å and material compositions are believed to be accurate to ± 1%. Ridge waveguide (RWG) devices with ridge widths of 2, 3, 4, and 5 μm and cavity lengths of 400 to 3000 μm ± 10 μm were processed. Eight to twelve lasers of each cavity length were tested.

The laser bars were mounted on copper blocks using silver paint. Thermistors were embedded in the copper blocks and the blocks were mounted on and thermally coupled to a thermoelectric cooler. A PID circuit was used in conjunction with the thermistor and cooler to set and stabilize the temperature. Current was delivered to the lasers through a spring loaded probe which was brought down onto the p-contact of the lasers using an x-y-z positioner stage. The n-contact was contacted to the copper block. Current was delivered to the devices using c.w. and pulsed driver circuits.

A schematic of the experimental setup used to measure laser spectra and LI curves is given in Fig. 2-3. Laser spectra were measured using a scanning monochromator. The scanning mirror allowed steps between measurements of 0.047 nm and the wavelength of the monochromator can be calibrated with an accuracy of ± 2 nm. The scanning mirror can only access a 20 nm range so to measure the wavelength range of the AMQW devices four separate scans were taken and pieced together to observe the complete wavelength range.

2.3 The Transition Cavity Length

Dimensionally AMQW lasers with QWs of two different thicknesses operate on the thick wells when the cavity length is long and on the thin wells when the cavity length is short. The cavity length above which a DAMQW laser with QWs of two different thicknesses operates on the thick wells and below which it operates on the thin wells we have defined to be the *Transition*

Cavity Length (TCL). For example, structure 1 lasers initially reached threshold at 23 °C on the 100 Å wells for cavity lengths ≥ 600 μm and on the 50 Å wells for cavity lengths ≤ 500 μm so we define the transition cavity length to be ≈ 550 μm.

The TCL is experimentally determined by plotting the lasing wavelength at laser threshold versus cavity length. Lasing wavelength at threshold is plotted versus cavity length for structure 1 in Fig. 2-4. The sharp decrease in lasing wavelength at threshold with decreasing cavity length marks the transition from lasing on the thick wells at long cavity lengths to lasing on the thin wells at short cavity lengths. From Fig. 2-4 the TCL for structure 1 was determined to be 550 ± 50 μm.

The physical origin of the TCL and the general properties of the TCL in all AMQW lasers are discussed in Chapter 4.

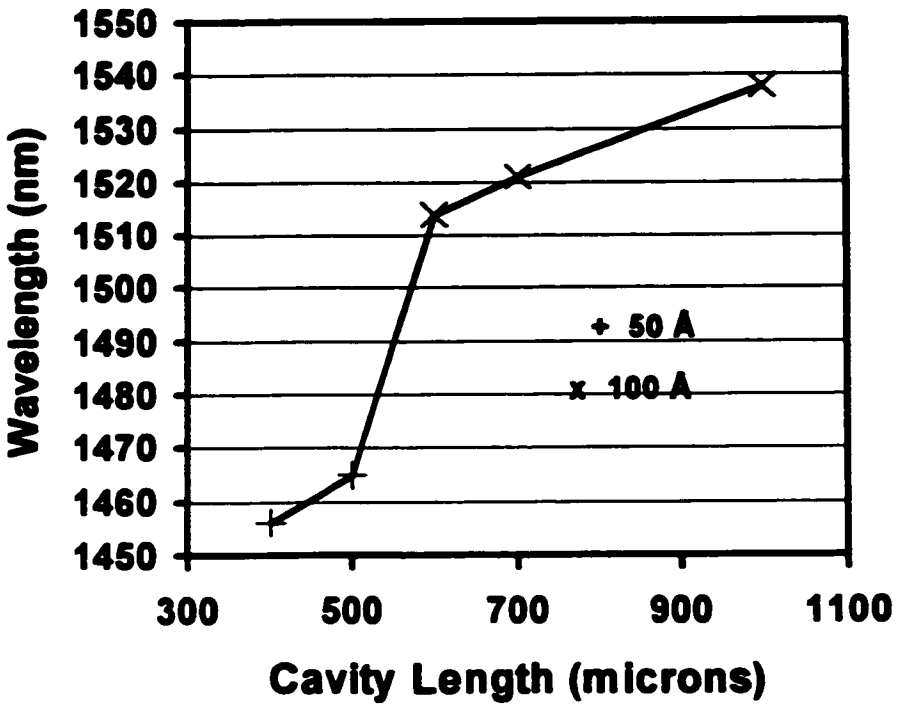

Fig. 2-4 Lasing wavelength at threshold versus cavity length for structure 1.

2.4 Spectral Properties of AMQW Lasers

In this section the spectral properties of AMQW lasers with cavity lengths near the TCL are described. The TCL marks the transition from operation on QWs of one thickness to QWs of another thickness and the spectral behaviour of devices near this transition is fascinating. For a range of cavity lengths longer than the TCL but still near the TCL AMQW devices lase at threshold on the thick QWs but with increasing current the lasing wavelength exhibits a large blue shift towards the lasing wavelength of the thin QWs. Further increasing the current causes the thin QWs to reach threshold and lase simultaneously with the thick QWs.

Ikeda *et al.* [6,8] reported switching from lasing on one thickness well to another and simultaneous lasing on two different thickness wells with changing current for AlGaAs devices. They stated that an unusually high and thick barrier layer between the different thickness wells was required to see these effects. We have found these effects to be very general properties of AMQW lasers and have observed them in a dozen different InP/InGaAsP AMQW laser structures with various barrier heights, barrier thicknesses and numbers of QWs.

We have studied the switching and simultaneous lasing phenomena as a function of temperature and cavity length. Using a pulsed laser drive current we have demonstrated that the switching effects do not appear to be thermal. Through the use of high speed measurements we have shown that wells of two different thicknesses appear to lase simultaneously.

2.4.1 Broad Wavelength Shifts and Simultaneous Lasing

The phenomena described in this section were observed for a range of cavity lengths longer than but near the TCL. Structure 1 lasers had a transition cavity length of 550 μm and these phenomena were observed in structure 1 lasers with cavity lengths ranging from 600 μm up

to 1000 μm. As the cavity length gets longer simultaneous lasing of the thick and thin wells no longer occurs and the amount of wavelength shift with changing current decreases until, for cavity lengths much longer than the TCL, no wavelength shift occurs at all and the devices operate as conventional MQW lasers. The range of cavity lengths over which the wavelength shift phenomena occur is relative to the TCL as can be seen in Appendix I and for a TCL near 600 μm is a few hundred μm above the TCL.

Fig. 2-5 shows the output spectra of a 600 μm structure 1 device at room temperature for drive currents of 65 mA, 120 mA, 140 mA, and 150 mA. The LI curve for the device at room temperature is shown in Fig. 2-6. The device reaches threshold at 60 mA and lases on the 100 Å well at a center wavelength of 1.537 μm. As can be seen in Fig. 2-5, at 65 mA the device behaves like a conventional MQW laser in which all the wells are 100 Å thick. The laser continues to behave like a conventional MQW laser until the current reaches 115 mA which corresponds to the beginning of the "kink" in the LI curve shown in Fig. 2-6. At 115 mA the spectrum begins to shift towards shorter wavelengths and broadens. Fig. 2-5 shows that at 120 mA the spectral range over which lasing modes exist is extremely broad. Modes with an appreciable fraction of the total output power exist from 1.535 μm to 1.505 μm covering a 30 nm range. This indicates that at 120 mA the gain peak is extremely flat over a 30 nm range. Increasing the current further causes the gain peak to shift to shorter wavelengths and become narrow. At 135 mA the 50 Å well reaches threshold and begins to lase simultaneously with the 100 Å well. As is shown in Fig. 2-5 at 140 mA the 50 Å well begins to lase at a center wavelength of 1.482 μm while the 100 Å well continues to lase over a range from 1.505 μm to 1.520 μm. Further increasing the current causes the lasing from the 50 Å and the 100 Å quantum wells to move towards each other. Note

that the emission wavelength of these devices could be changed by greater than 50 nm by changing the operating current or temperature.

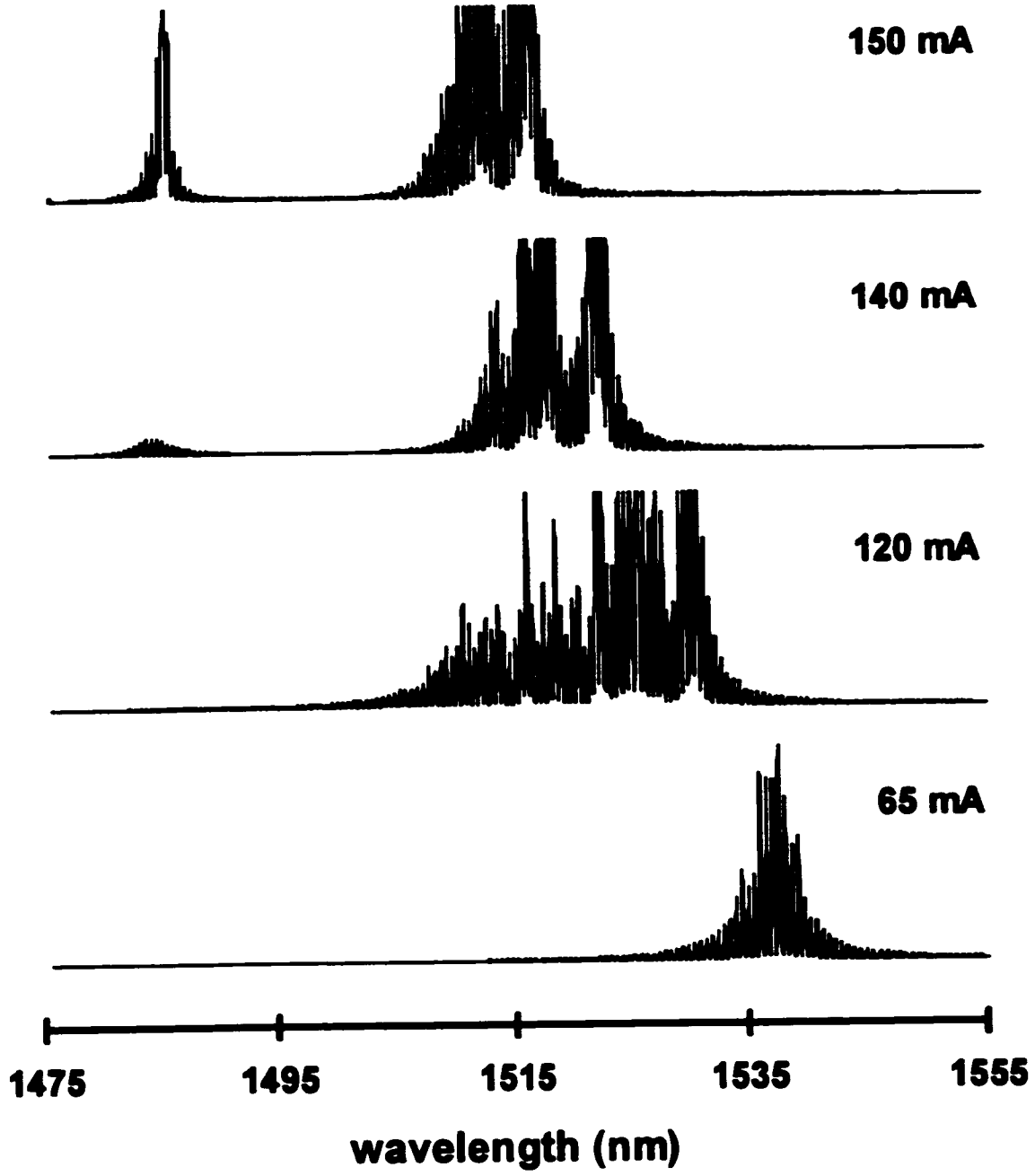

Fig. 2-5 Measured spectra for a structure 1 device with a 600 μm cavity length. The spectra were taken at 23 °C and at c.w. operating currents of 65, 120, 140, and 150 mA.

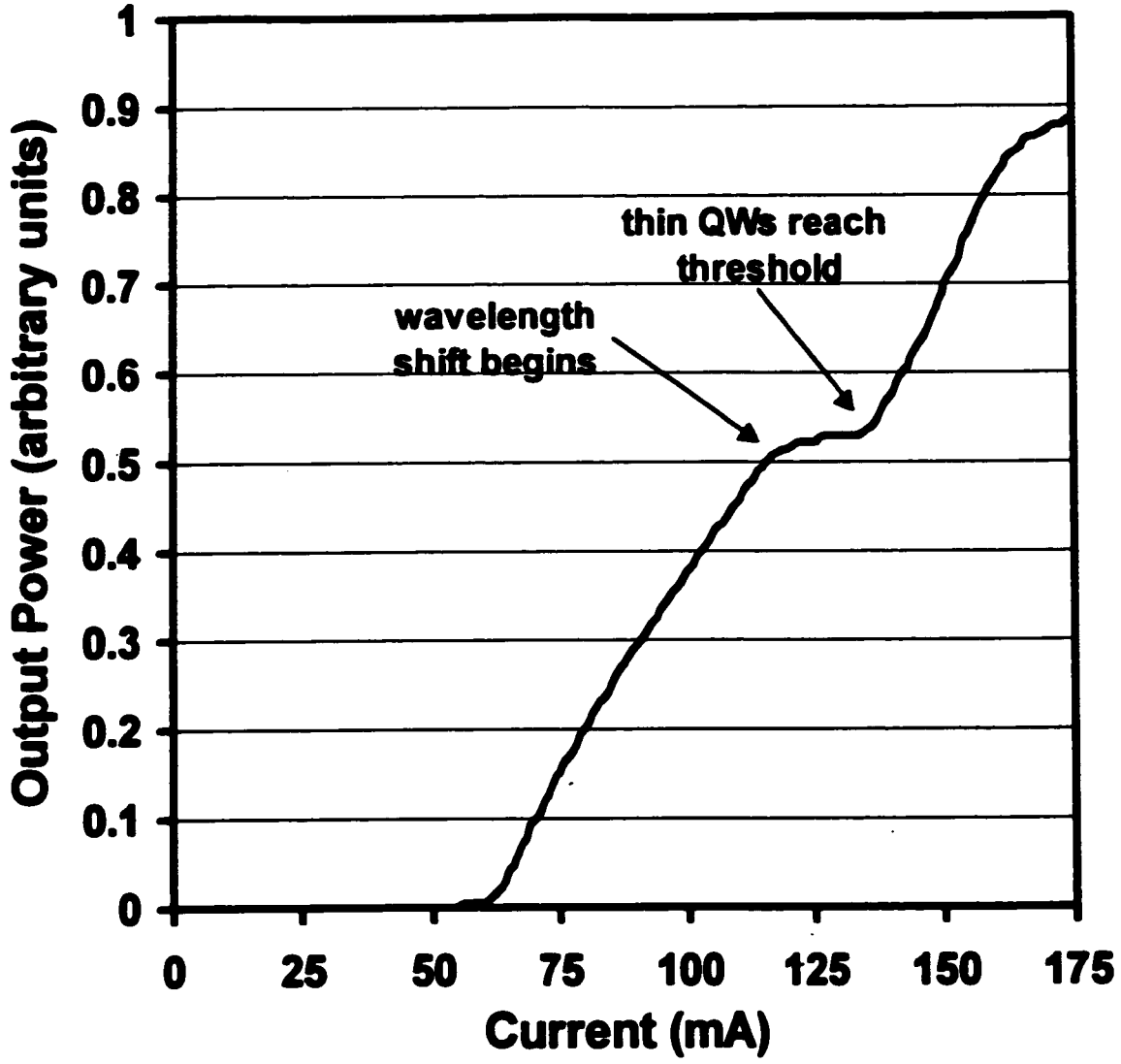

Fig. 2-6 LI curve for the 600 μm structure 1 device whose spectra are shown in Fig. 2-5.

2.4.2 Below and Far Above the TCL

The interesting broad wavelength shifts and simultaneous lasing reported in the previous section only occur for cavity lengths longer than, but near, the TCL. For cavity lengths substantially longer than the TCL the devices reach threshold on the thick wells and continue to lase on the thick wells for high current injection (a maximum current of 260 mA was used). No large wavelength shifts or contributions from the thin wells occur. The spectra of a structure 1

laser with a cavity length of 2000 μm is shown in Fig. 2-7 for currents of 70 mA (just above threshold) and 230 mA. The emission spectra broadens out for high current injection but no blue shift occurs and no contribution is seen at wavelengths corresponding to the thin wells. The LI curve of the 2000 μm structure 1 device is shown in Fig. 2-8. No "kink" occurs in the LI curve as was observed for the 600 μm structure 1 devices. The 2000 μm structure 1 device behaves like a conventional MQW laser with only the thick wells in the active region.

The spectra of a 500 μm structure 1 device are shown in Fig. 2-9 for currents below and above threshold. The 500 μm cavity length is just below the TCL for structure 1. Below threshold, for low currents, light is initially emitted from the thick wells. With increasing current the thin wells begin to produce light and eventually dominate the spectrum. The transition from the thick wells to the thin wells occurs entirely below threshold. The device reaches threshold on the thin wells and above threshold continues to lase on the thin wells. No wavelength shifts or contributions from the thick wells are observed above threshold. Above threshold the device behaves like a conventional MQW laser with only the thin wells in the active region. The LI curve of the 500 μm structure 1 device is shown in Fig. 2-10. Again, no "kink" occurs in the LI curve as was observed for the 600 μm structure 1 devices.

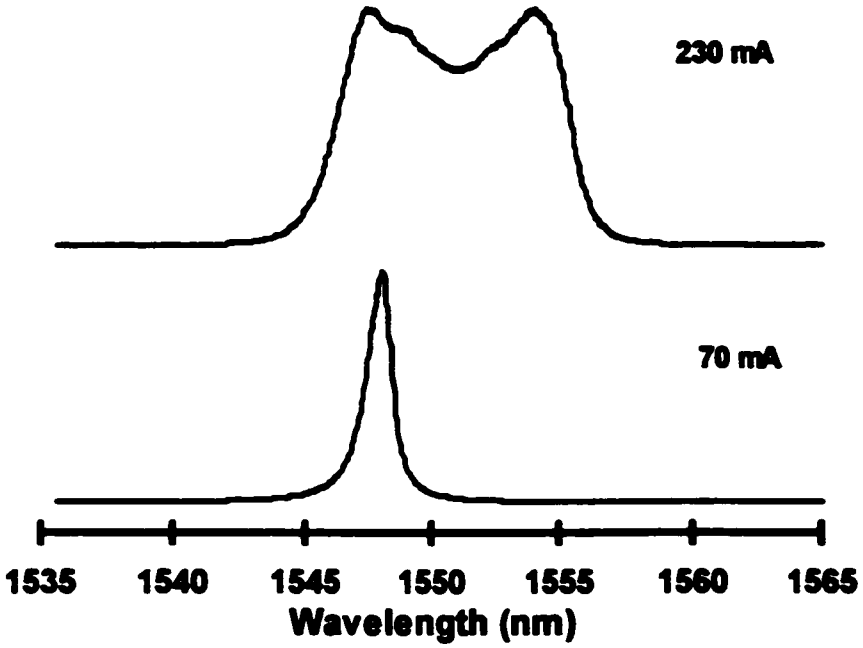

Fig. 2-7 Measured spectra for a structure 1 device with a 2000 μm cavity length. The spectra were taken at 23 °C and at c.w. operating currents of 70 and 230 mA.

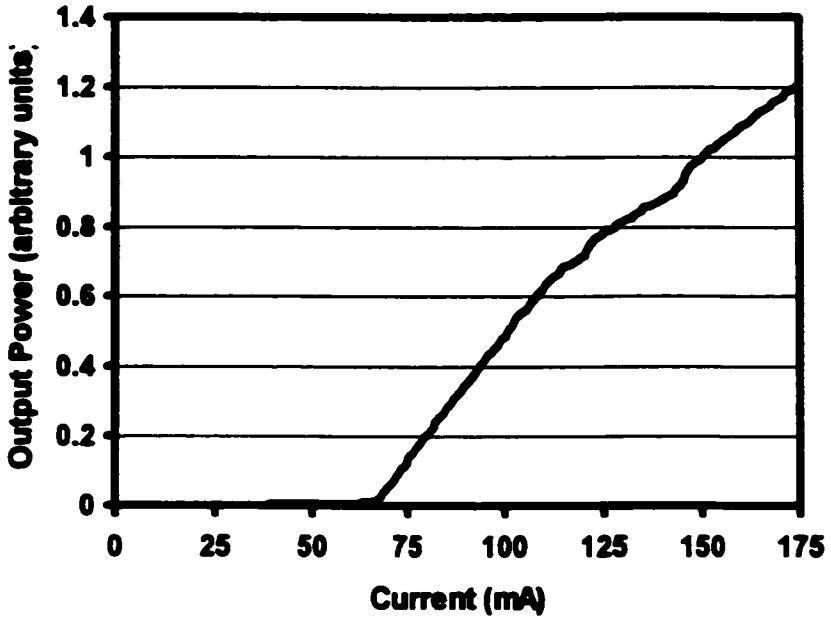

Fig. 2-8 LI curve for the 2000 μm structure 1 device whose spectra are shown in Fig. 2-7.

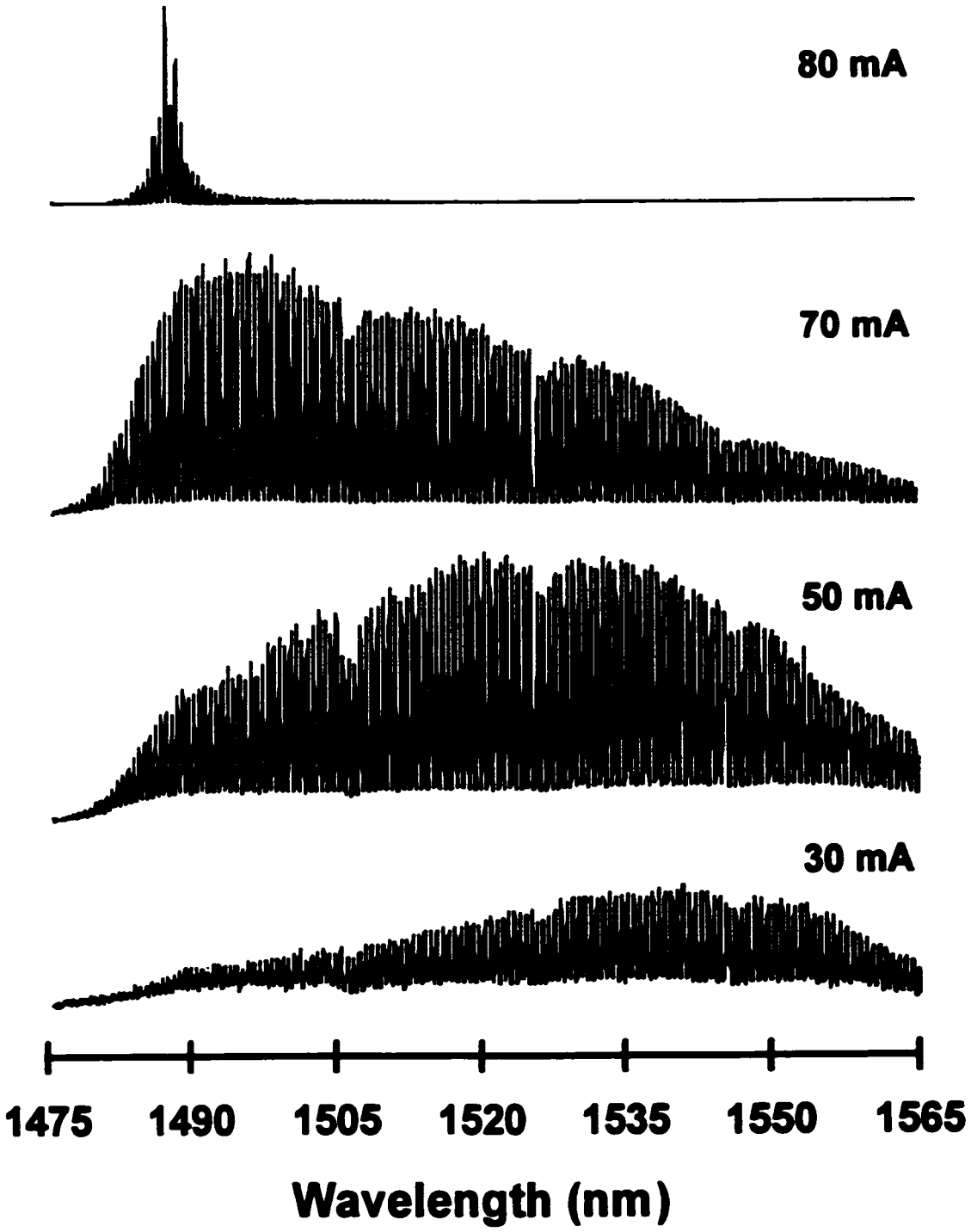

Fig. 2-9 Measured spectra for a structure 1 device with a 500 μm cavity length. The spectra were taken at 23 °C and at c.w. operating currents of 30, 50, 70, and 80 mA.

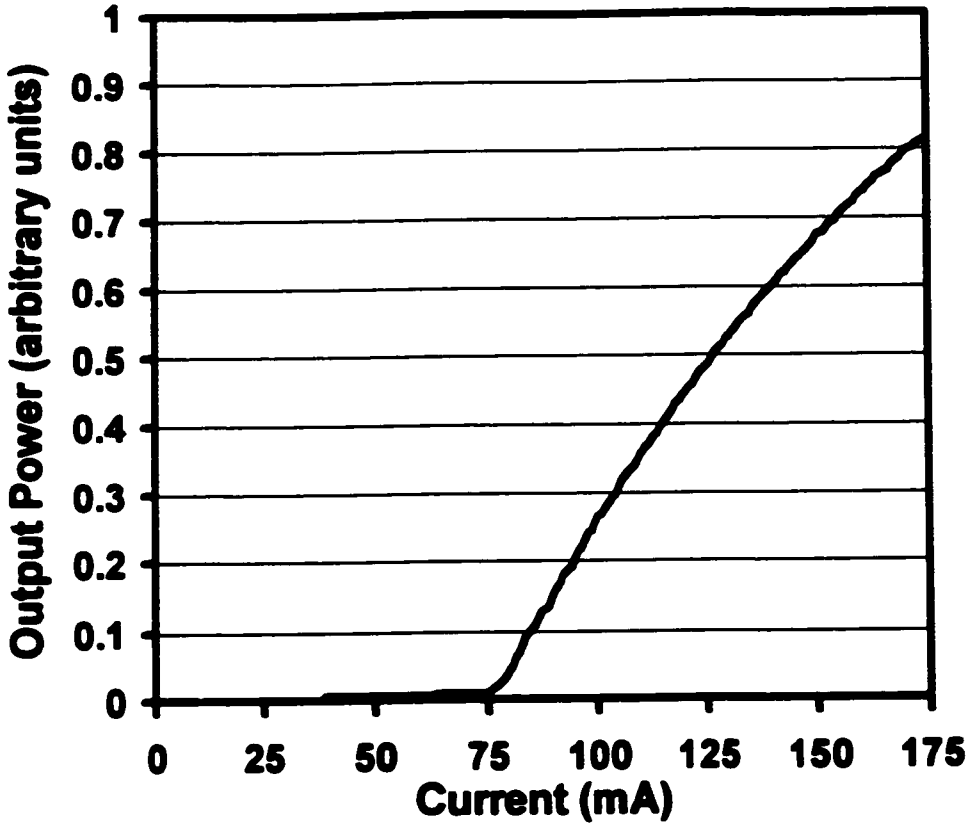

Fig. 2-10 LI curve for the 500 μm structure 1 device whose spectra are shown in Fig. 2-9.

2.4.3 Temperature Dependence

Switching from lasing on the 100 Å well to lasing on the 50 Å well was also observed while changing the temperature of the 600 μm cavity length lasers and keeping the current constant. The spectra of a 600 μm structure 1 laser are shown in Fig. 2-11 for a range of temperatures and a current of 110 mA. At 17 °C the device lases at 1.535 μm, corresponding to the 100 Å well, and increasing the temperature to 30 °C results in a switch to lasing at 1.490 μm corresponding to the 50 Å well.

The LI curves for a 600 μm structure 1 laser are shown in Fig. 2-12 for temperatures of 17 °C, 23 °C and 30 °C. The spectra of the device at 17 °C are shown in Fig. 2-13 for currents of 135, 155, and 165 mA and the spectra of the device at 30 °C are shown in Fig. 2-14 for currents

of 100 mA and 170 mA. When the device is at 17 °C the wavelength shift and lasing of the thin QWs occur at higher currents than when the device is at 23 °C. The "kink" in the LI curve moves to higher currents and becomes more pronounced. The beginning of the "kink" still corresponds to the beginning of the wavelength shift and the end of the "kink" corresponds to the threshold of the thin QWs. At 30 °C the devices reach threshold on the thin wells and operate above threshold entirely on the thin wells. The LI curve does not have a "kink". At 30 °C the 600 μm devices behave similarly to the 500 μm devices at 23 °C. The TCL is temperature dependent. The TCL increases with increasing temperature and decreases with decreasing temperature.

2.4.4 Pulsed Operation

Structure 1 devices with 600 μm cavity lengths were tested under pulsed current injection conditions to determine if the switching process is thermal. The lasers were driven with 2 μs current pulses with a 0.6 % duty cycle. As was observed under c.w. operation the 600 μm cavity length lasers began lasing on the 100 Å well and with increased current switched to lasing on the 50 Å well. The pulses were too short for substantial heating of the junction to take place. This demonstrates that the switching process is non-thermal. A time and wavelength resolved examination of the laser output for current levels large enough for the laser to lase on the 50 Å well determined that, at the beginning of the pulse, only the 100 Å well emits light and that the 50 Å wells do not produce light until the end of the pulse.

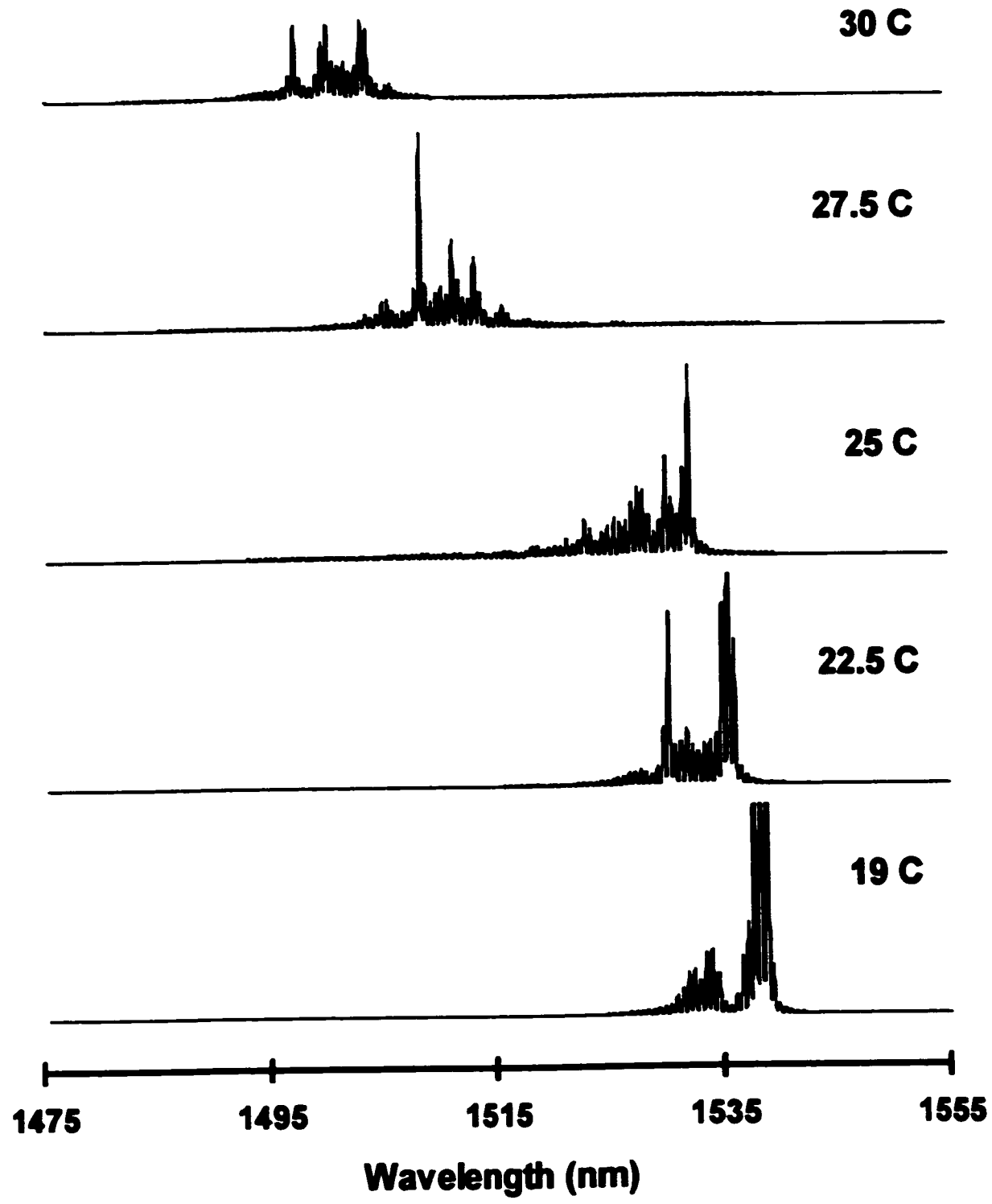

Fig. 2-11 Measured spectra for a structure 1 device with a cavity length of 600 μm. The spectra are taken at a c.w. operating current of 110 mA and at temperatures of 19, 22.5, 25, 27.5, and 30 °C.

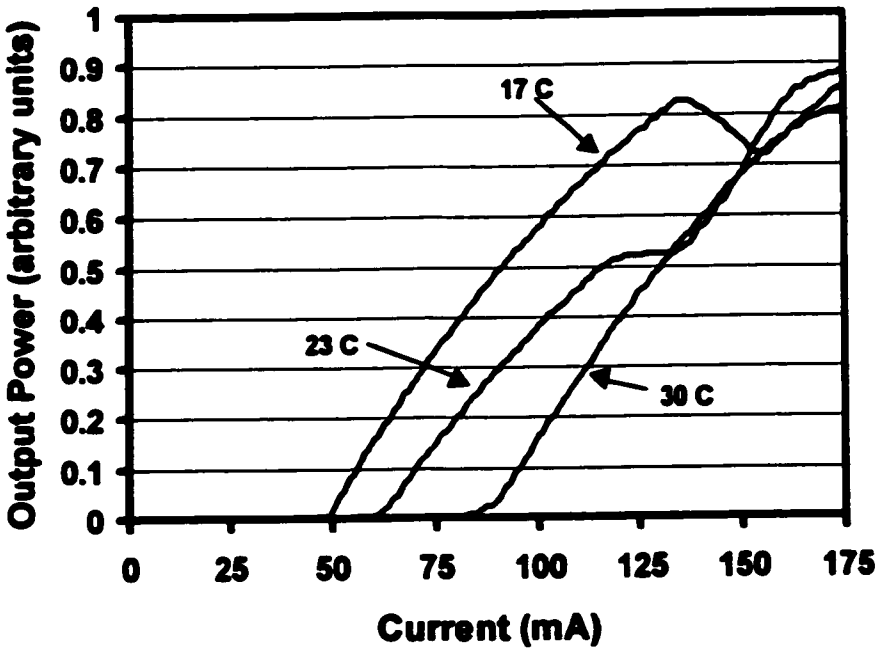

Fig. 2-12 LI curves for a structure 1 device with a 600 μm cavity length taken at 17, 23, and 30 °C.

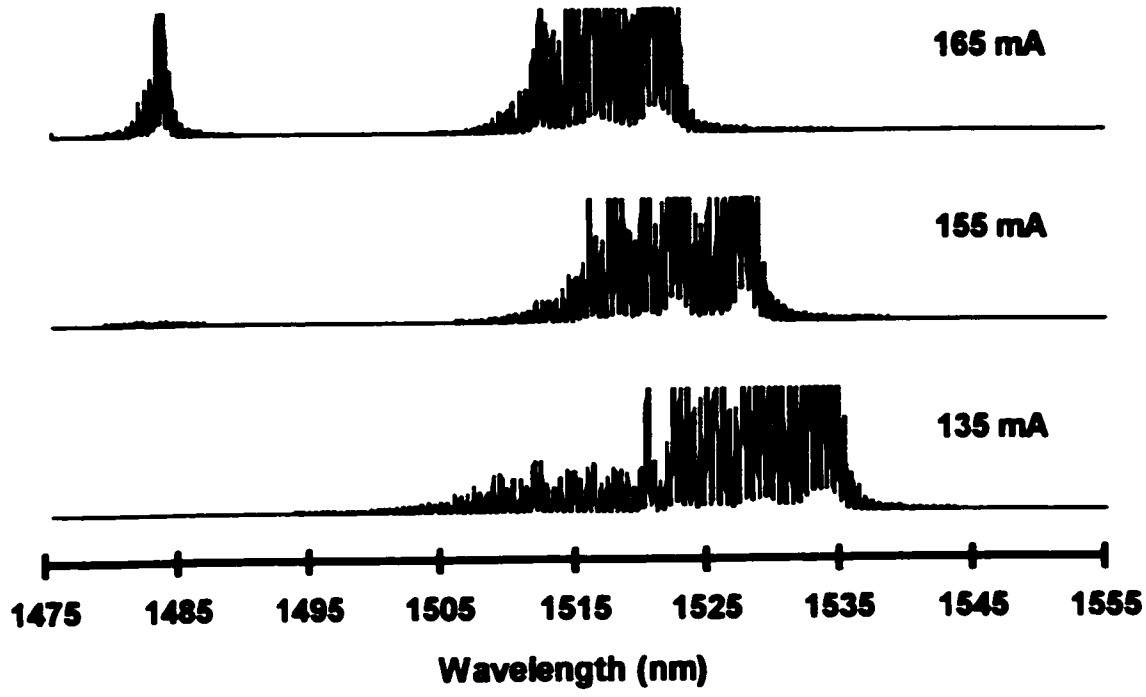

Fig. 2-13 Measured spectra at 17 °C for the 600 μm cavity length structure 1 device whose LI curves are shown in Fig. 2-12.

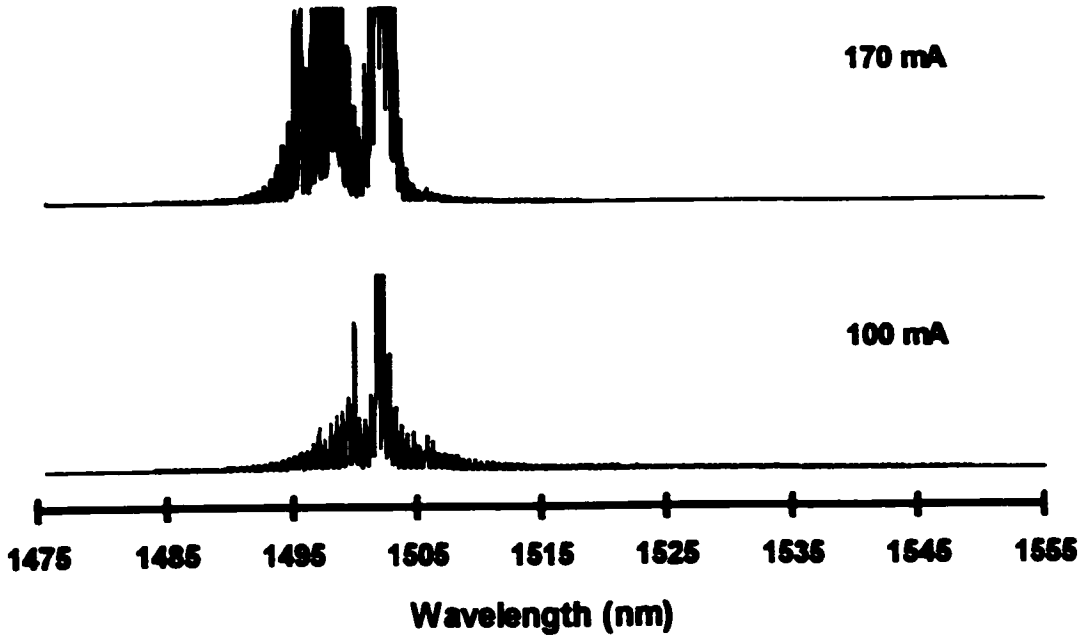

Fig. 2-14 Measured spectra at 30 °C for the 600 μm cavity length structure 1 device whose LI curves are shown in Fig. 2-12.

2.4.5 Simultaneous Lasing

For devices with cavity lengths longer than but near the TCL (described in section 2.4.1 above) and for high injection currents, the thick and thin wells were observed to lase simultaneously. However, lasing could be rapidly switching between the thick and thin wells such as occurs with the various modes of a multimode laser which is called partitioning. High speed measurements were performed to determine whether AMQW lasers do in fact lase simultaneously on the thick and thin wells or partitioning between the wells takes place. A high speed detector and monochromator were used to examine the lasing emission from the 100 Å and 50 Å wells. A 600 μm structure 1 device was tested at a current of 150 mA. No partitioning between the 100 Å and 50 Å QWs was observed on a 10 ns time scale. The thick and thin QWs appear to lase simultaneously.

2.5 Conclusion

The spectral properties of AMQW lasers are strongly dependent on cavity length. For structures with wells of two different thicknesses, devices with long cavity lengths reach threshold on the thick QWs while short cavity length devices reach threshold on the thin QWs. We defined the TCL as the cavity length above which such a structure reaches threshold on the thick wells and below which devices reach threshold on the thin wells. Devices with cavity lengths longer than but near the TCL initially reach threshold on the thick QWs and then exhibit a large shift in wavelength with increasing current. This shift is followed by the thin QWs reaching threshold and appearing to lase simultaneously with the thick QWs. High speed measurements did not reveal partitioning between lasing on the thick and thin wells. The TCL was found to increase with increasing temperature and decrease with decreasing temperature. Pulsed measurements demonstrated that the observed wavelength shifts are not due to thermal effects. These phenomena were observed in thirteen different AMQW laser structures and I believe they are general properties of AMQW lasers.

3. CHAPTER 3 – THE TCL METHOD

3.1 Introduction

In Chapter 1 I listed reasons for studying AMQW lasers and stated that AMQW devices provide a means of experimentally probing the active region. The QWs emit at different wavelengths and hence are distinguishable. This enables one to determine the relative strengths of the QWs in the active region. We have used this feature of AMQW lasers to develop a new experimental technique for studying the distribution of carriers in the QWs of a MQW active region.

In a MQW laser the carrier density is not generally the same in each QW. The distribution of carriers in the QWs can profoundly affect device operation and is crucial to the understanding of MQW devices [16,21,22,25,33,34,35]. We have developed an experimental technique which employs AMQW lasers to quantify the degree to which the non-uniform carrier distribution affects the net gain of QWs at different locations in the active region.

A great deal of experimental work has been done to study carrier transport in QW lasers. This work consists mostly of time resolved photoluminescence experiments, pump probe experiments, and modulation response measurements [36]. These experiments are designed to study the high speed dynamics of carriers in QW lasers. Of key interest in this field are transport time across the heterostructure and carrier capture rate into the QWs as these two factors play a fundamental role in the high speed characteristics of QW laser devices. These experiments are not designed to measure the distribution of carriers in MQW lasers. A plethora of theoretical work has also been done to model carrier transport. Two basic types of models exist; elementary rate equation models and Poisson solver models. Theoretical carrier transport models are used to fit

to experimental carrier transport data and are capable of modeling many of the high speed properties of MQW lasers. Many theoretical carrier transport models predict a non-uniform carrier distribution in MQW lasers and the non-uniform carrier distribution has been studied theoretically at length [37]. However, carrier transport experiments are not designed to study the non-uniform carrier distribution and the theoretical predictions of the carrier transport models have not been compared to direct experimental measurements of the non-uniform carrier distribution.

Many experimental observations have been attributed to the non-uniform carrier distribution. For example Hazell *et. al.* [33] have used the non-uniform carrier distribution to explain experimental results obtained from structures with varying barrier heights. The non-uniform carrier distribution is evident in experimental data taken from complex coupled DFB lasers. Morrison *et. al.* [35] have shown the gain of the wells on the p-side is higher than the gain of the wells on the n-side of the active region of complex coupled DFB lasers and have attributed this to the non-uniform carrier distribution.

AMQW lasers can be used to study experimentally the non-uniform carrier distribution across the active region of MQW lasers. Yamazaki *et. al.* [16] were the first to use AMQW lasers to provide evidence of the non-uniform carrier distribution. Using AMQW lasers we have developed a quantitative experimental technique, called the Transition Cavity Length (TCL) method, which allows us to study the relative populations of wells on the p-side versus the n-side of the active region under electrically pumped, cw operating conditions [21,22,25]. We believe our technique has provided the first direct experimental measurement of the degree to which the non-uniform carrier distribution affects the gain of QWs in the active region. Our experimental

technique has provided new, quantitative information about the degree to which the non-uniform carrier distribution affects the gain of the QWs in a MQW active region under normal operating conditions and about the dependencies of the non-uniform carrier distribution on structural parameters such as the thickness and height of the quantum barriers.

In this chapter the TCL method is described and the experimental results of three studies performed using the TCL method are presented.

3.2 The TCL Method

In this section the TCL method is described. The section begins with an explanation of what mirror image AMQW structures are and their role in the TCL method. It is shown how comparing mirror image structures can reveal qualitative information about the carrier distribution. Next, the full, quantitative TCL method is described and the type of information the method yields is shown. Finally, the importance of the TCL when comparing mirror image structures or when using AMQW lasers to study the carrier distribution is explained.

3.2.1 Mirror Image Structures

Two mirror image DAMQW structures have nominally the same layers, compositions, thicknesses, doping, etc., but the ordering of the QWs from the p-side to the n-side of the active region is reversed in the two structures. Structures 1 and 2 in Fig. 3-1 are mirror image structures. The measured photoluminescence (PL) spectra of structures 1 and 2 are shown in Fig. 3-2. The PL of the two structures is nearly identical. In PL experiments the lasers are optically pumped which pumps all of the wells approximately equally regardless of their location in the active region. The two structures have nominally identical dimensions, compositions and number of quantum wells; only the ordering of the wells in the active region is different in the two

structures. When the wells are all equally pumped their location in the active region does not matter and, hence, the PL of structures 1 and 2 are expected to be nominally the same.

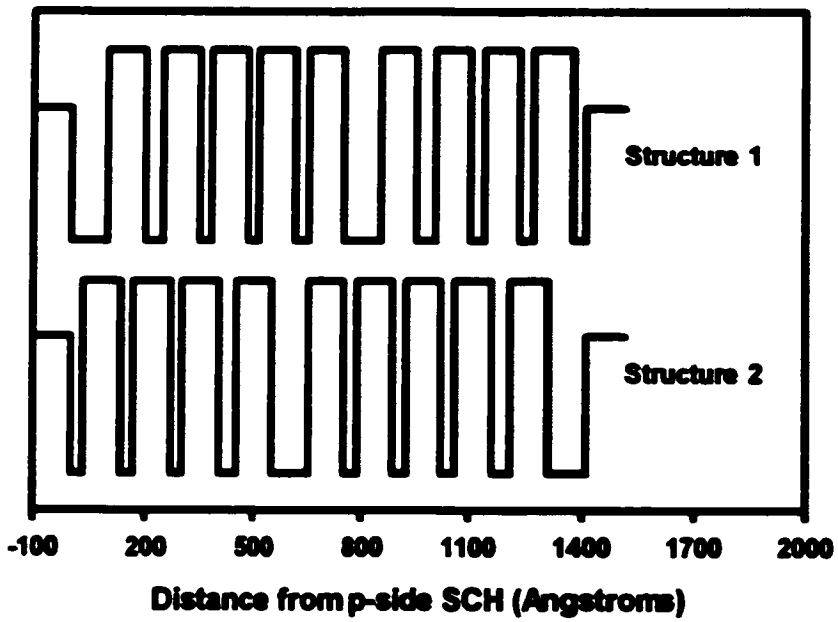

Fig. 3-1 Valence band energy diagram for the active region of structures 1 and 2.

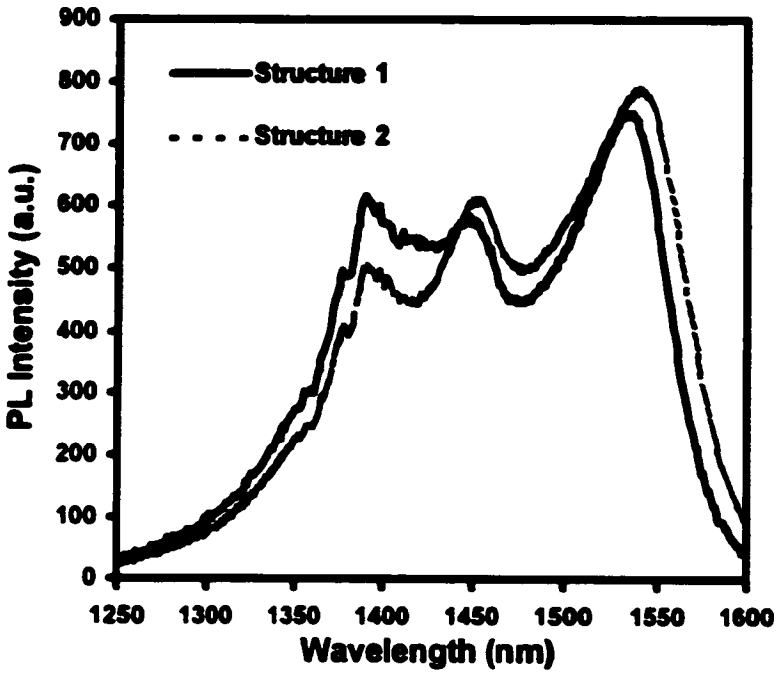

Fig. 3-2 Measured photoluminescence spectrum for structure 1 and 2.

The operating characteristics of mirror image AMQW lasers can be substantially different under electrical pumping conditions. Yamazaki *et al.* [16] were the first to use mirror image AMQW lasers to demonstrate that the carrier distribution across the active regions of MQW lasers is uneven. They observed, for a cavity length of 300 μm, that a device with the thick wells on the p-side of the active region operated on the thick wells and that the mirror image device with the thin wells on the p-side of the active region operated on the thin wells. The authors concluded that laser operation is achieved on the wells near the p-side of the active region because carriers concentrate near the p-side wells. Yamazaki *et al.* also noted a difference in threshold currents for the mirror image devices with 300 μm cavity lengths. The important result from this work is that if you fabricate two devices to be the same (same number of wells, thicknesses, barriers, cladding layers, ridge waveguide dimensions, etc.) with the only difference being that the order of the QWs is reversed then the devices behave differently and, therefore, the ordering of the wells is important. It is reasonable to deduce that this is due to the theoretically predicted [37] non-uniform carrier distribution. If all the QWs in the active region are pumped uniformly then their position in the active region should not affect the operating characteristics of a device. Hence if the carrier distribution among the QWs is uniform then mirror image structures should have identical operating characteristics. Thus, differences between mirror image AMQW structures can yield information about the non-uniformity of the carrier distribution.

We have studied the operation of mirror image AMQW lasers as a function of cavity length. We have found, in thirteen different AMQW structures, that regardless of the ordering of the QWs all AMQW lasers with QWs of two different thicknesses operate on the thick QWs for relatively long cavity lengths and on the thin QWs for short cavity lengths. In chapter 2 we defined the *Transition Cavity Length* (TCL) as the cavity length above which AMQW lasers with

QWs of two different thicknesses reach threshold on the thick QWs and below which they reach threshold on the thin QWs. Mirror image AMQW lasers have different TCLs. Structures with the thick wells on the p-side of the active region have shorter TCLs than the mirror image structures. This can be explained as follows. When the thick wells are on the p-side of the active region they contribute more gain. As the cavity length is decreased the amount of gain medium between the laser facets decreases so more gain is required to overcome the output coupling losses. When the thick wells are on the p-side of the active region they have higher gain and can, therefore, overcome the output coupling losses at shorter cavity lengths than they can when they are located on the n-side of the active region. This results in a shorter TCL. The enhanced gain of wells when they are located near the p-side of the active region is due to the non-uniform carrier distribution. Holes have a much lower mobility than electrons and the valence band has larger band offsets so that holes remain localized near the p-side of the active region. As a result most of the gain in the active region is contributed by QWs near the p-side.

Mirror image AMQW laser structures have different TCLs. The TCLs are different due to the non-uniform carrier distribution. Thus the difference in TCLs between mirror image AMQW laser structures gives a *qualitative* measure of the non-uniformity of the carrier distribution. The closer the TCLs of mirror image AMQW laser structures are together the more uniform the carrier distribution.

3.2.2 Quantitative Measure of The Non-uniform Carrier Distribution

Next, a *quantitative* estimate of the degree to which the uneven carrier distribution affects the contribution of wells to the laser oscillation is developed. Using only the elementary laser threshold condition we can use the difference in TCLs for mirror image structures to determine

numerically the difference in *net gain* for wells when they are located near the p-side versus the n-side of the active region. It is important to distinguish that numerical values are obtained for the net gain which encompasses the intrinsic gain of the QWs, various loss mechanisms and various pumping mechanisms. To extract accurately parameters such as the carrier density per well the net gain must be broken down into its constituents. However, the difference in net gain for wells located on the p-side versus the n-side of the active region is a useful characterization parameter. It quantifies the degree to which the uneven carrier distribution affects device performance.

The elementary laser threshold condition states $R^2 e^{2gL} \equiv 1$ [4]. From the laser threshold condition we directly obtain the relation $g_{thick} \cdot L_t = \text{const} = \hat{g}_{thick} \cdot \hat{L}_t$ where g_{thick} is the net gain of the thick wells and L_t is the transition cavity length for the structure with the thick wells on the p-side of the active region and $\hat{g}_{thick}$ and $\hat{L}_t$ are the net gain of the thick wells and the transition cavity length for the mirror image structure. The constant in this relation can be eliminated by forming the normalized difference. We find

$$\xi = \frac{\hat{L}_t - L_t}{\hat{L}_t + L_t} = \frac{g_{thick} - \hat{g}_{thick}}{g_{thick} + \hat{g}_{thick}}. \qquad \text{Eq. 3-1}$$

ξ is the *normalized difference in transition cavity lengths* between two mirror image AMQW structures. From Eq. 3-1,

$$g_{thick} = \hat{g}_{thick} \cdot \frac{1+\xi}{1-\xi}. \qquad \text{Eq. 3-2}$$

Thus, the experimentally measured TCLs can be used to obtain numerical values for the ratio of the net gains of the thick wells when they are located on the p-side versus the n-side of the active region.

3.2.3 Importance of the TCL

Other groups have compared mirror image AMQW lasers of a single cavity length for the purpose of studying the uneven carrier distribution. Our results demonstrate that studying devices of a single cavity length is not adequate and a method such as the difference in TCLs must be used for this purpose. We believe our results are consistent with the experimental observations of Yamazaki *et al.* [16] and Evans *et al.* [38] but some of the conclusions drawn in Ref. [16] and Ref. [38] may be specious because the authors only studied one cavity length. We believe that the 300 μm cavity length used by Yamazaki *et al.* [16] is below the TCL for their structure A and above the TCL for their structure B. In addition one should note that decreasing the temperature of the devices, as Yamazaki *et al.* have done, increases the material gain of the QWs which causes a similar effect as increasing the cavity length. Therefore, operating at low temperatures, as Yamazaki *et al.* have done, is similar to working with long cavity lengths. Thus, it is not surprising (and it is consistent with our results) that Yamazaki *et al.* found both structures to operate on the thick wells at low temperatures. The conclusion drawn by Yamazaki *et al.* that the carrier distribution is not uneven for low temperatures may, therefore, be incorrect. We also believe that the 1000 μm cavity length used by Evans *et al.* is well below the TCL for their structures and hence the performance of both structures is dominated by the thin well so that the devices appear to be the same. Evans *et al.* reported differences in the mirror image devices for low temperatures ($T < 150$ K). Moving to lower temperatures would be similar to moving closer to the TCLs for these devices where there should be a greater difference between the devices. Evans *et al.* also used AlGaAs devices where the carrier distribution is expected to be more even than that of InP based devices due to the higher mobility of holes in GaAs [39].

The results of Yamazaki *et al.* [16] indicate that it may be possible to use the threshold current of mirror image devices of a *single cavity length* to qualitatively and perhaps quantitatively study the uneven carrier distribution that is not dependent on the TCL. We have found the threshold current (I_{th}) of structures with the thick wells on the p-side of the active region can be higher, lower, or nominally the same as the I_{th} of their mirror image structures depending on the cavity length. For example, at a cavity length of 3000 μm, I_{th} = 111 ± 2.5 mA for structure 6 and I_{th} = 102 ± 2.5 mA for structure 5; at a cavity length of 2400 ± 2.5 μm, I_{th} = 105 ± 2.5 mA for structure 6 and I_{th} = 104 ± 2.5 mA for structure 5; and at a cavity length of 1000 μm, I_{th} = 66 ± 2.5 mA for structure 6 and I_{th} = 91 ± 2.5 mA for structure 5. Therefore, studying I_{th} for mirror image structures of an arbitrary cavity length yields three different results depending on the cavity length used.

3.3 Studies Done Using The TCL Method

We have performed three comparative studies using the TCL method. The first examines the role of quantum barrier height in determining the carrier distribution by comparing structures with low and high quantum barriers. The second studies the degree to which the non-uniformity of the carrier distribution affects devices with varying numbers of QWs. The final study examines the role of quantum barrier thickness on the uneven carrier distribution by comparing structures with 100 Å, 50 Å and 30 Å thick quantum barriers.

3.3.1 Quantum Barrier Height

In this section we use four AMQW laser structures to demonstrate that the non-uniform carrier distribution across the active region of MQW lasers is dependent on the height of the quantum well barriers. We compare four structures: two with high barriers and two with low

barriers. We show that the devices with high barriers have a non-uniform carrier distribution across the active region and that the devices with low barrier heights have a more even carrier distribution.

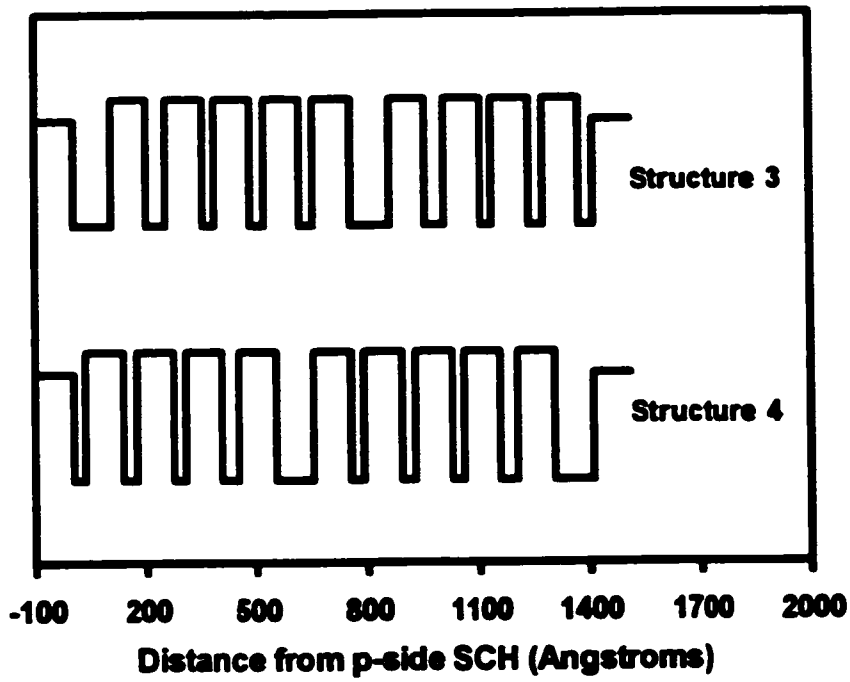

Fig. 3-3 Valence band energy diagram for the active region of structures 3 and 4.

Four laser structures were grown at McMaster University using gas source molecular beam epitaxy. Structures 1 and 2 were shown in Fig. 3-1 and structures 3 and 4 are shown in Fig. 3-3. Each structure contains two 100 Å wells, two 50 Å wells and six 35 Å wells separated by 100 Å barriers. Structures 1 and 3 are mirror images of structures 2 and 4. Structures 1 and 3 have the 100 Å wells on the p-side of the active region and the 35 Å wells on the n-side of the active region while structures 2 and 4 have the 35 Å wells on the p-side of the active region and the 100 Å wells on the n-side of the active region. Structures 1 and 2 have wells of composition $In_{.775}Ga_{.225}As_{.780}P_{.220}$ and barriers of composition $In_{.775}Ga_{.225}As_{.305}P_{.695}$. The wells are 1% compressively strained and the barriers are 0.57% tensile strained. Structures 3 and 4 have wells

of composition $In_{.775}Ga_{.225}As_{.760}P_{.240}$ and barriers of composition $In_{.775}Ga_{.225}As_{.390}P_{.610}$. The wells are 0.8% compressive strained and the barriers are 0.4% tensile strained. Layer thicknesses and compositions are precise to within ± 3 Å and ± 1% respectively. Ridge waveguide (RWG) devices were processed from each material. Ridge widths of 2, 3, 4, and 5 μm were made. Cavity lengths ranging from 300 to 2000 μm ± 10 μm were tested. Four to twelve lasers of each cavity length were tested. The devices were mounted and tested as described in chapter 2. All measurements were taken at 23 °C.

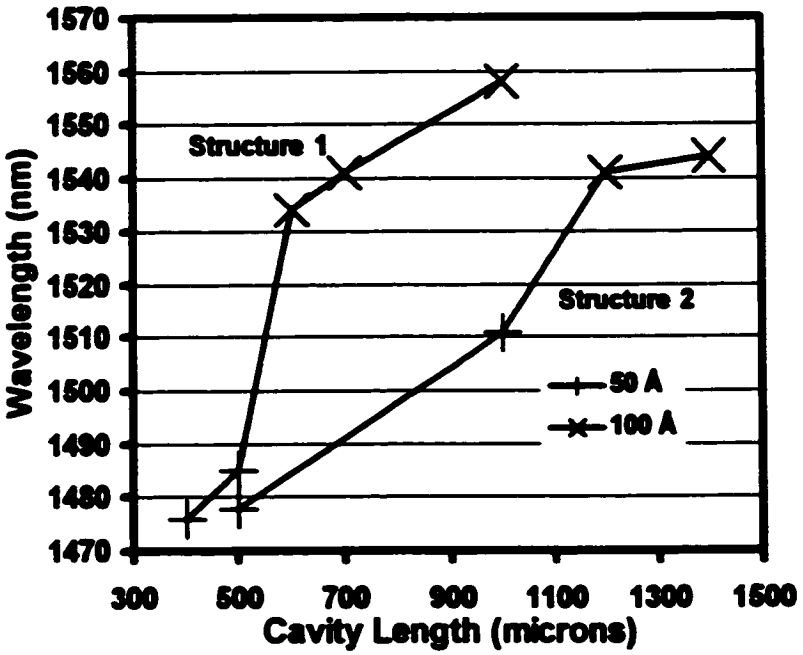

Fig. 3-4 Lasing wavelength at threshold versus cavity length for structures 1 and 2.

The wavelength at threshold is plotted versus cavity length in Fig. 3-4 for structures 1 and 2. The sharp drop in wavelength with decreasing cavity length marks the TCL. The transition cavity length for structure 1 is ≈ 550 μm and the transition cavity length for structure 2 is ≈ 1150 μm. The large difference in transition cavity length between structures 1 and 2 shows that the location of the QWs in the active region strongly affects how the devices operate. The 100 Å

QWs in the structure 1 lasers are on the p-side of the active region and are preferentially pumped, due to the non-uniform carrier distribution, allowing the 100 Å QWs to dominate laser operation to much shorter cavity lengths than in the structure 2 devices.

The degree to which the non-uniform carrier distribution affects the net gain of the thick wells when they are located on the p- versus the n-side of the active region can be quantified using Eq. 3-1 and Eq. 3-2. We find that $g_{thick} = 2.08 \cdot \hat{g}_{thick}$ meaning the net gain of the 100 Å QWs is more than twice as big when the 100 Å QWs are on the p- versus the n-side of the active region.

Structures 3 and 4 were grown to investigate the effect of barrier height on the carrier distribution across the active region. Structures 3 and 4 are similar to structures 1 and 2 except that the well and barrier material compositions were changed to reduce the height of the barriers. The difference in band gap energy between the wells and barriers in structures 1 and 2 was 480 meV. This was reduced to 371 meV in structures 3 and 4, a reduction of ≈ 110 meV. To decrease the barrier height and maintain strain compensation in the structure, the strains in the wells and barriers were different in structures 3 and 4 from what they were in structures 1 and 2. Simulations were performed using Lastip [40] to investigate the effect of strain on the carrier distribution. Fig. 3-5 shows the valence bands and quasi-Fermi levels for four different simulated structures. The structures in the top row have barrier heights of 480 meV and the structures in the bottom row have barrier heights of 371 meV. The structures in the left column have 0.8 % compressively strained wells and the structures in the right column have 1.0 % compressively strained wells. Comparing the left and right columns of Fig. 3-5 indicates that strain does not have a large effect on carrier distribution while comparing the top and bottom rows of Fig. 3-5

indicates that barrier height has a large effect on the carrier distribution. Based on these simulations we believe that the change in strain does not strongly affect the carrier distribution.

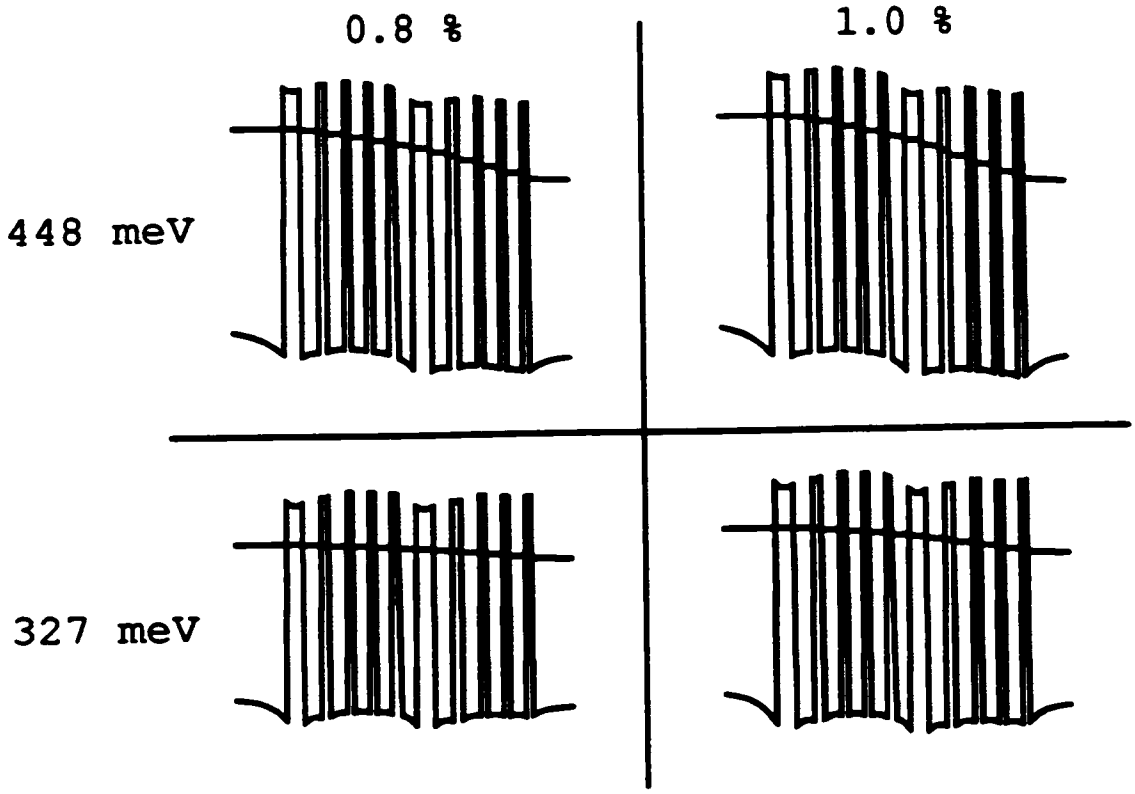

Fig. 3-5 Valence bands and quasi-Fermi levels for structures with different strains and barrier heights. The structures in the top row have barrier heights of 480 meV and the structures in the bottom row have barrier heights of 371 meV. The structures in the left column have 0.8 % compressively strained wells and the structures in the right column have 1.0 % compressively strained wells.

Lasing wavelength at threshold is plotted versus cavity length for structures 3 and 4 in Fig. 3-6. The transition cavity length for structure 3 is ≈ 850 μm and the transition cavity length for structure 4 is ≈ 1000 μm. The transition cavity lengths for structures 3 and 4 are much closer together than the transition cavity lengths for structures 1 and 2 qualitatively indicating a more uniform carrier distribution. Using the experimentally determined TCLs and Eq. 3-1 and Eq. 3-2 we find for structure 3 and 4 $g_{thick} = 1.18 \cdot \hat{g}_{thick}$. Decreasing the barrier height by 110 meV causes

the difference in gains for the thick wells when they are located on the p-side versus the n-side of the active region to decrease from 108 % to just 18 % for 1.5 μm InGaAsP/InP AMQW lasers.

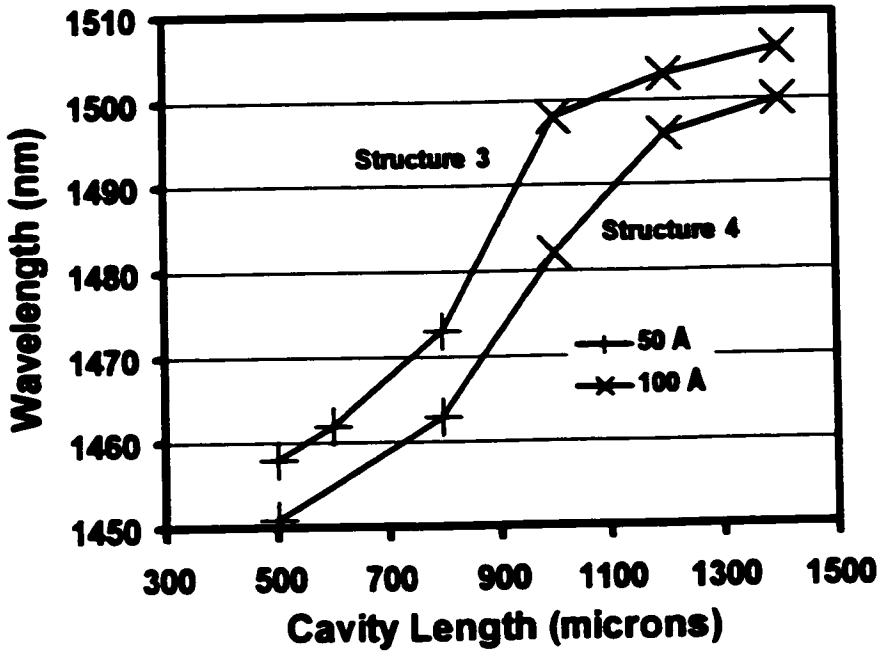

Fig. 3-6 Lasing wavelength at threshold versus cavity length for structures 3 and 4.

To summarize we have used four AMQW laser structures and simulations to study the effect of barrier height on the carrier distribution across the active region of MQW lasers. Two of the structures demonstrated that the carrier distribution across the active region of a MQW laser is non-uniform. Carriers appear to be localized near the p-side of the active region, preferentially pumping wells near the p-side. A similar pair of structures were grown with a 110 meV decrease in barrier height and we observed that the carrier distribution across the active region became more uniform. These results indicate that well position in the active region and barrier height are important design parameters for MQW lasers.

3.3.2 Numbers of QWs

In this section we examine the effect of the uneven carrier distribution on lasers with different numbers of QWs. The non-uniform carrier distribution has previously been studied by looking at the lasing wavelength at threshold for mirror image AMQW structures with nine [16] and ten [21] QWs. In addition, Evans *et al.* [38] studied the spontaneous emission spectra of two mirror image asymmetric AlGaAs structures with the same cavity length which had only two QWs. They reported that at room temperature the carrier distribution across the active region appeared to be uniform.

Four laser structures were grown at McMaster University using gas source molecular beam epitaxy. Structures 5 through 8 are shown schematically in Fig. 3-7 and Fig. 3-8. Structure 5 contains a 100 Å well and a 50 Å well and structure 7 contains two 100 Å wells followed by two 50 Å wells. All the wells are 1 % compressively strained with composition $In_{.775}Ga_{.225}As_{.810}P_{.190}$ and are separated by 0.57 % tensile strained 100 Å barriers of composition $In_{.775}Ga_{.225}As_{.305}P_{.695}$. The active regions of structures 6 and 8 are the mirror images of structures 5 and 7 respectively. Ridge waveguide (RWG) devices were processed from each material. Ridge widths of 2, 3, 4, and 5 μm were made. Cavity lengths ranging from 500 to 3000 μm ± 10 μm were tested. The devices were mounted and tested as described in chapter 2. Wavelength data are the mean values for the lasers tested of each cavity length. All measurements were taken at 23 °C.

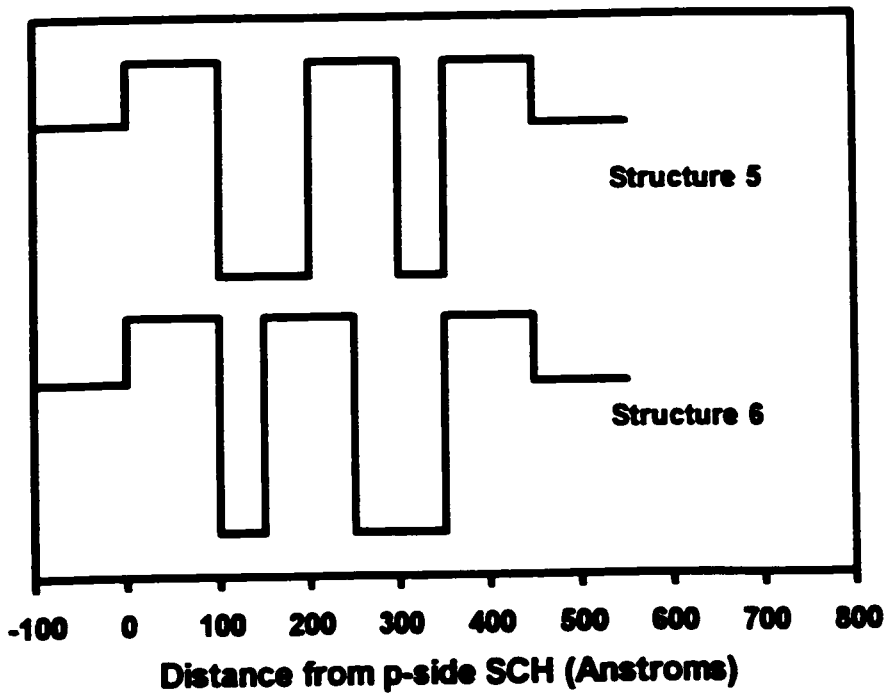

Fig. 3-7 Valence band energy diagram for the active region of structures 5 and 6.

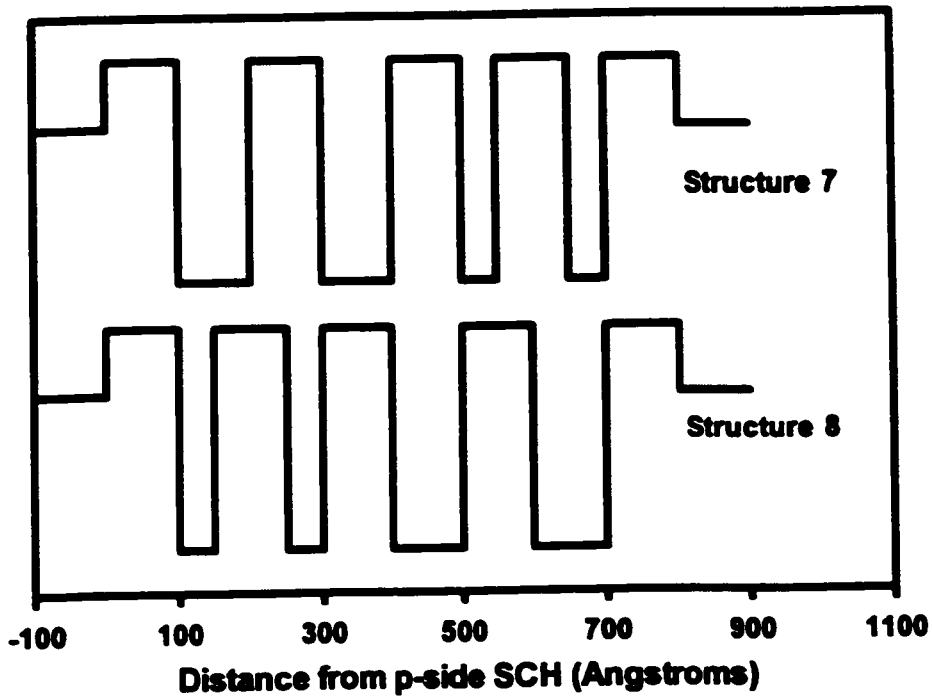

Fig. 3-8 Valence band energy diagram for the active region of structures 7 and 8.

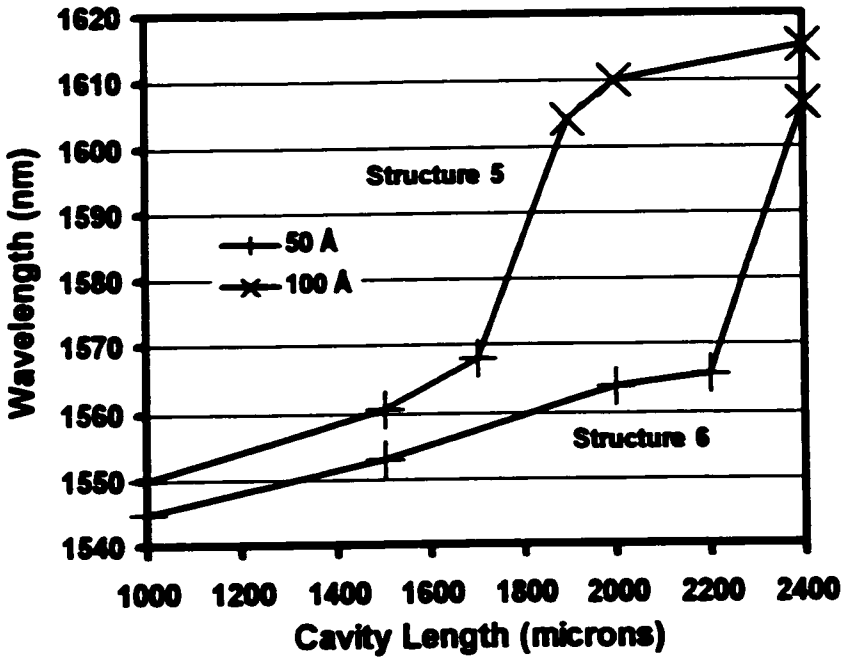

Fig. 3-9 Lasing wavelength at threshold versus cavity length for structures 5 and 6.

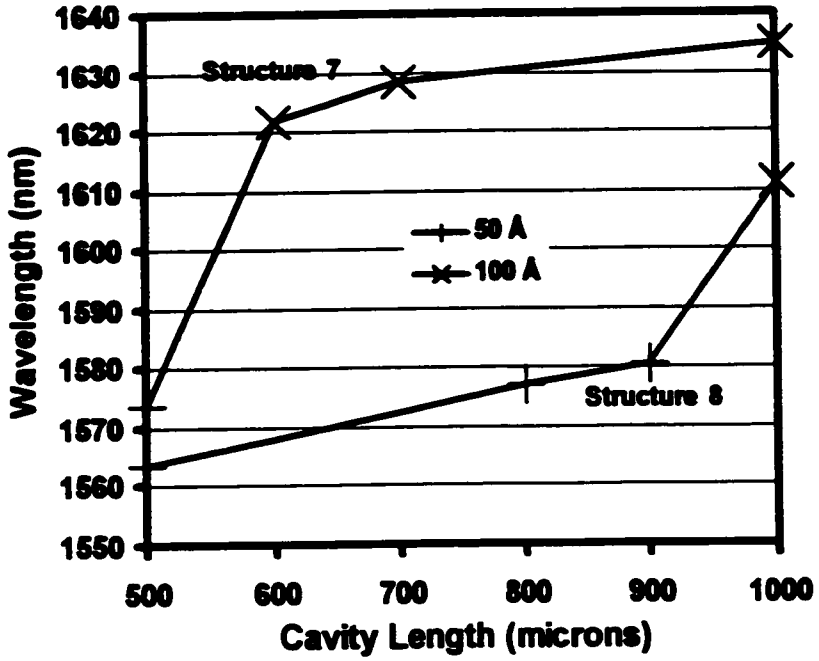

Fig. 3-10 Lasing wavelength at threshold versus cavity length for structures 7 and 8.

Here we list the magnitude of the ratio of net gains for wells on the p-side versus the n-side of the active region by applying the analysis derived in section III to three mirror image pairs of laser structures containing different numbers of QWs. Fig. 3-9 and 10 show the threshold lasing wavelength of structures 5 - 8 as a function of cavity length. The sharp drops in lasing wavelength with decreasing cavity length demonstrate the transition from lasing on the 100 Å wells to the 50 Å wells at threshold. The TCL is taken to be the midpoint of these sharp transitions. The TCL for structure 5 is 1800 ± 100 μm, for structure 6 it is 2300 ± 100 μm, for structure 7 it is 550 ± 50 μm and for structure 8 it is 950 ± 50 μm. Using Eq. 3-1 and Eq. 3-2 for structures 5 and 6, $g_{thick} = 1.27 \cdot \hat{g}_{thick}$; for structures 7 and 8, $g_{thick} = 1.74 \cdot \hat{g}_{thick}$. In the previous section we found that for structures 1 and 2, with ten QWs, $g_{thick} = 2.08 \cdot \hat{g}_{thick}$. The difference in the net gain of wells that are next to the p-side versus the n-side is substantial.

Structures 5 and 6 have only two QWs and yet the thick well has 27 % more gain when it is located on the p-side of the active region than when it is located on the n-side of the active region! The non-uniform carrier distribution affects the device performance of InGaAsP AMQW lasers with only two QWs which demonstrates that the non-uniform carrier distribution is important even to the design and understanding of MQW devices with small and simple active regions.

The increase in the net gain of the thick wells when they are on the p-side versus the n-side of the active region for structures 5 and 6 is 27 %, for structures 7 and 8 is 74 % and for structures 1 and 2 is 108 %. Increasing the number of QWs from two to four to ten increases the effect of the uneven carrier distribution. For four QWs the uneven carrier distribution already has a very large effect on the net gain of the thick wells and for ten QWs the net gain is decreased by

more than a factor of two when the thick wells are on the n-side of the active region. The comparison of net gains for the thick wells in mirror image structures allows us to quantify the degree to which the uneven carrier distribution affects devices. The results for the three mirror image pairs of structures analyzed here demonstrate that the uneven carrier distribution has a substantial effect on devices with as few as two QWs and the effect increases dramatically for devices with four and ten QWs. These results indicate that an understanding of the uneven carrier distribution is vital to the understanding of MQW lasers and the uneven carrier distribution needs to be taken into account when analyzing devices.

In summary, this study has demonstrated that the degree to which the non-uniform carrier distribution affects the net gain of the QWs increases with the number of QWs. The non-uniform carrier distribution is shown to affect the performance of devices with as few as two QWs. Thus, the non-uniform carrier distribution is important to the design and understanding not only of AMQW lasers with many wells but also of simpler laser structures.

3.3.3 Quantum Barrier Thickness

In this section we study the effect of quantum barrier thickness on the distribution of carriers among the wells in InGaAsP laser devices using the TCL method. The effect of barrier thickness on device performance is not well understood. We experimentally demonstrate the degree to which quantum barrier thickness affects the carrier distribution and thus show the importance of quantum barrier thickness as a design parameter when making MQW devices.

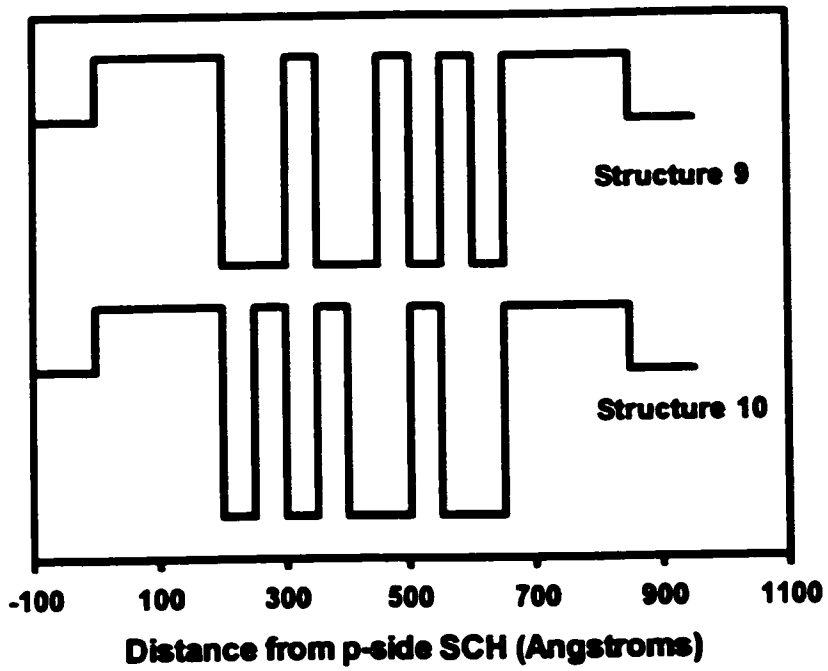

Fig. 3-11 Valence band energy diagram for the active region of structures 9 and 10.

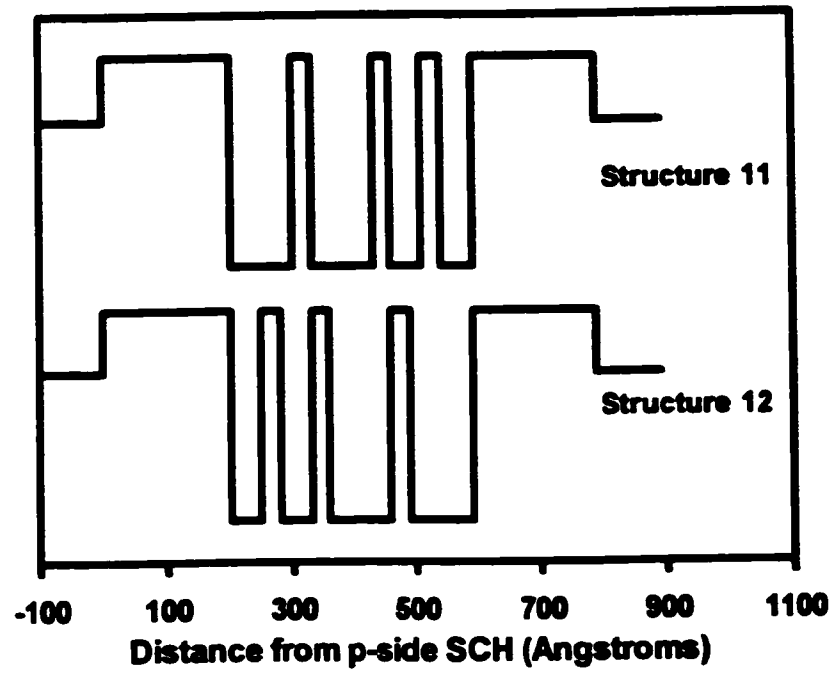

Fig. 3-12 Valence band energy diagram for the active region of structures 11 and 12.

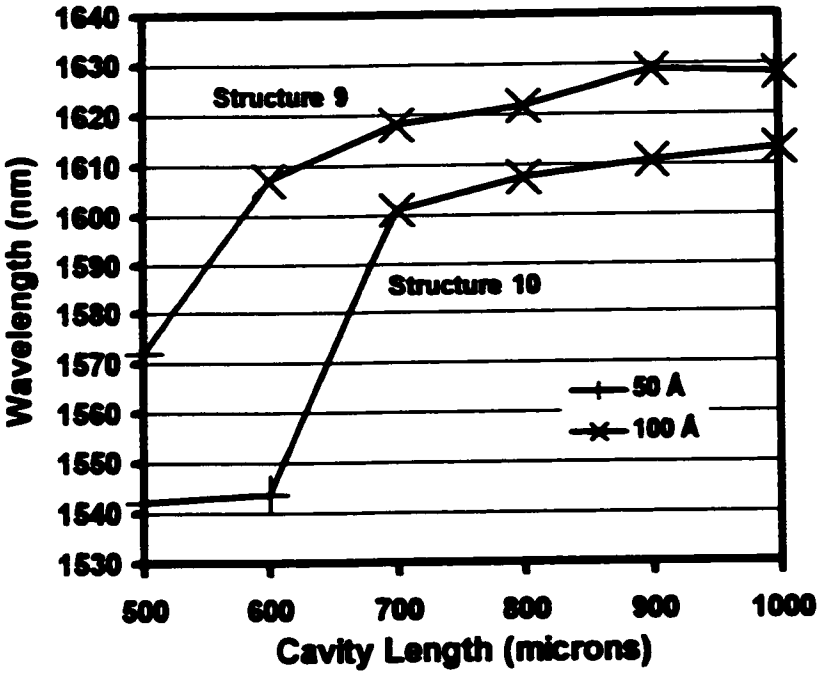

Fig. 3-13 Lasing wavelength at threshold versus cavity length for structures 9 and 10.

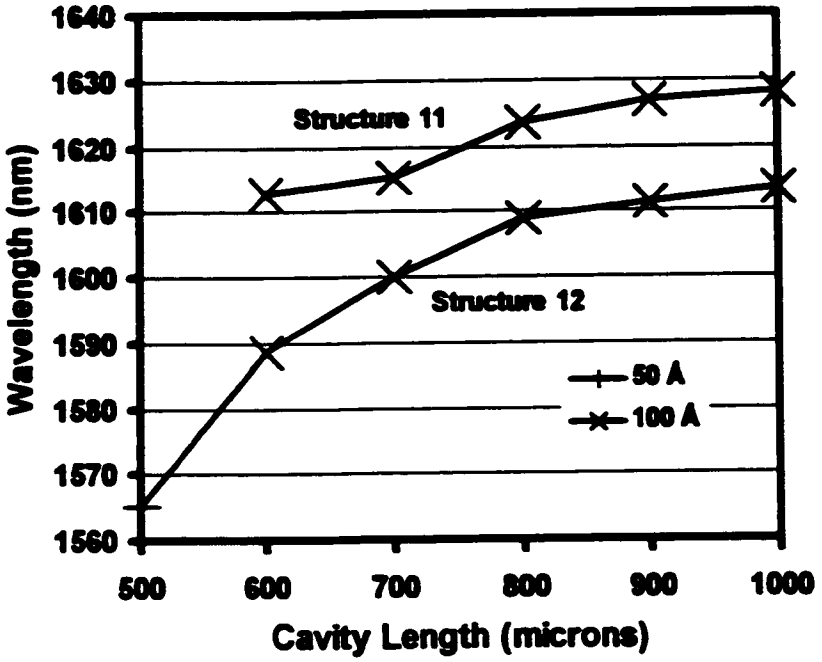

Fig. 3-14 Lasing wavelength at threshold versus cavity length for structures 11 and 12.

Structures 9 through 12 were grown for this study at McMaster University using gas source molecular beam epitaxy and are shown schematically in Fig. 3-11 and Fig. 3-12. Structures 10 and 12 are the mirror images of structures 9 and 11 respectively. Each structure contains two 100 Å wells and two 50 Å wells of composition $In_{.775}Ga_{.225}As_{.810}P_{.190}$. Structures 9 and 10 have 50 Å barriers and structures 11 and 12 have 30 Å barriers. All barriers are of composition $In_{.775}Ga_{.225}As_{.305}P_{.695}$. The wells are 1% compressively strained and the barriers are 0.57% tensile strained. Structures 9 and 11 have the 100 Å wells on the p-side while structures 10 and 12 have the 100 Å wells on the n-side of the active region. Structures 9 and 11 differ from structure 7 only by the thickness of the barrier layers and structures 10 and 12 differ from structure 8 only by the thickness of the barrier layers. Layer thicknesses and compositions are estimated to be within ± 3 Å and ± 1% of their target values respectively. Ridge waveguide (RWG) devices of widths 2, 3, 4, and 5 μm were processed from each material. Cavity lengths ranging from 300 to 2000 μm ± 10 μm were tested. Wavelength data are the mean values for the lasers tested of each cavity length.

Fig. 3-13 and Fig. 3-14 show the wavelength at threshold versus cavity length for structures 9 through 12. The sharp drop in the wavelength at threshold with decreasing cavity length indicates the transition cavity length where operation at threshold switches from the 100 Å wells at longer cavity lengths to the 50 Å wells at short cavity lengths. The TCLs for structures 7 and 8 were reported in the previous section. The TCL for structure 7 is 550 ± 50 μm and the TCL for structure 8 is 950 ± 50 μm. From Fig. 3-13 and Fig. 3-14 we see that the TCL for structure 9 is 550 ± 50 μm, the TCL for structure 10 is 650 ± 50 μm, the TCL for structure 11 is < 600 μm, and the TCL for structure 12 is 650 ± 50 μm. Using the TCLs for structures 7 and 8

with Eq. 3-1 and Eq. 3-2 we find that for the structures with 100 Å barriers the net gain of the thick wells when they are on the p-side of the active region is 74 % larger than the net gain of the thick wells when they are on the n-side of the active region ($g_{thick} = 1.74 \cdot \hat{g}_{thick}$). For structure 9 and 10 with 50 Å barriers we find $g_{thick} = 1.18 \cdot \hat{g}_{thick}$, i.e., the net gain of the thick wells is 18 % higher when they are located on the p-side of the active region than when they are on the n-side. The ratio of net gains for the thick wells on the p-side versus the n-side of the active region could not be found experimentally for the devices with 30 Å barriers as the structure 11 devices did not lase for cavity lengths shorter than 600 μm due to a bad electrical contact. Decreasing the barrier thickness from 100 Å to 50 Å decreases the effect of the uneven carrier distribution on the net gain from 74 % to only 18 %. Thin barrier layers result in a substantially more uniform carrier distribution. Thus, barrier thickness should be recognized as an important design parameter for MQW laser design.

3.4 Conclusion

We have developed an experimental technique, called the Transition Cavity Length (TCL) method, which employs mirror image AMQW lasers to quantify the degree to which the non-uniform carrier distribution in MQW lasers affects the net gain of QWs at different positions in the active region. We have performed three studies using the TCL method involving twelve different AMQW laser structures. The studies were designed to determine the effect of barrier height and barrier thickness on the non-uniformity of the carrier distribution and the degree to which the non-uniform carrier distribution affects devices with different numbers of QWs.

The active regions of the AMQW laser structures we have studied are summarized in Table 3-1. All active regions were embedded in the structure shown in Fig. 2-1 of chapter 2. The

barrier height in Table 3-1 is defined as the total difference between the band gap of the barrier and the band gap of the quantum well. Structure 13 is described in detail in Chapter 6 and was designed as a broadly tunable device. The mirror image of structure 13 was not grown.

The experimentally determined TCL data for all 13 structures is summarized in Table 3-2 along with the experimentally determined ratio of net gains for QWs located on the p-side versus the n-side of the active region. The first important result to be taken from Table 3-2 is the magnitude of the effect the carrier distribution has on the gain of wells located at different positions in the active region. Depending on the structure, wells located on the p-side of the active region have between 18 % and 109 % more gain than wells located on the n-side of the active region. These results clearly indicate that the carrier distribution can dramatically affect device performance and hence should be taken into account when designing or understanding the behaviour of MQW lasers. From Table 3-2 we can also discern several important trends. First, the effect of the non-uniform carrier distribution on the net gain of a well when it is located on the p-side versus the n-side of the active region decreases dramatically with decreasing barrier height. Structures 1 through 4 show that for a 10 QW laser with 480 meV barriers, a well located at the p-side of the active region has twice the net gain it has when it is located at the n-side of the active region but for the same structure with 371 meV barriers the well only has 18 % more gain when it is located on the p-side as opposed to the n-side of the active region. Barrier height has a large effect on the non-uniformity of the carrier distribution and is an important design parameter in this respect. Structures 7 through 10 demonstrate that decreasing the barrier thickness has a similar effect on the carrier distribution as decreasing the barrier height. For structures 7 and 8 with 100 Å barriers the gain of the wells when located on the p-side of the active region is 74 % higher than when the wells are on the n-side of the active region while for structures 9 and 10

with 50 Å barriers the gain of the wells when located on the p-side of the active region is only 18 % higher than when they are located on the n-side. Barrier thickness has a large effect on the non-uniformity of the carrier distribution and is also an important design parameter in this respect.

Structure	Barrier Thickness (Å)	Barrier Height (meV)	Well x & y	Barrier x & y	Thickness of wells in order from p-side to n-side (Å)
1	100	480	.24, .78	.24, .31	100 50 35 35 35 100 50 35 35 35
2	100	480	.24, .78	.24, .31	35 35 35 50 100 35 35 35 50 100
3	100	371	.23, .76	.23, .39	100 50 35 35 35 100 50 35 35 35
4	100	371	.23, .76	.23, .39	35 35 35 50 100 35 35 35 50 100
5	100	495	.20, .81	.20, .31	100 50
6	100	495	.20, .81	.20, .31	50 100
7	100	495	.20, .81	.20, .31	100 100 50 50
8	100	495	.20, .81	.20, .31	50 50 100 100
9	50	495	.20, .81	.20, .31	100 100 50 50
10	50	495	.20, .81	.20, .31	50 50 100 100
11	30	495	.20, .81	.20, .31	100 100 50 50
12	30	495	.20, .81	.20, .31	50 50 100 100
13	100	452	.18, .69	.18, .24	30 60 30 60 30 60

Table 3-1 Structural information on the active regions of all thirteen structures.

Structure	Experimental TCL ± 100 μm	Experimental $g_{thick} / \hat{g}_{thick}$
1	550	2.09
2	1150	
3	850	1.18
4	1000	
5	1800	1.28
6	2300	
7	550	1.73
8	950	
9	550	1.18
10	650	
11	< 600	N/A
12	650	
13	≈ 250	N/A

Table 3-2 Experimental results of the TCL method for all thirteen AMQW laser structures.

4. CHAPTER 4 – THEORETICAL MODEL

4.1 Introduction

A great deal of theoretical work has been done modeling carrier transport in MQW lasers. Two types of carrier transport models exist in the literature; Poisson/continuity equation solvers and ambipolar rate equation models. Both types of carrier transport models predict a non-uniform carrier distribution in MQW lasers and the non-uniform carrier distribution has been studied using these models. Nagaragan and Bowers show the non-uniform carrier distribution predicted by the two types of carrier transport models for an InGaAs/InP active region with ten 100 Å QWs in chapter 3 of the text edited by Kapon [37]. The structure they simulate is similar in material and dimensions to the devices we have studied. Nagarajan and Bowers show that the two types of carrier transport models result in nearly identical non-uniform carrier distributions [37].

The TCL method described in chapter 3 has provided the first quantitative experimental data on the degree to which the non-uniform carrier distribution affects the net gain of QWs at different locations in the active region. Prior to the advent of the TCL method no direct experimental measure of the non-uniformity of the carrier distribution existed to test the validity of the carrier distributions predicted by existing carrier transport models. The TCL method has provided new experimental data on the degree of non-uniformity of the carrier distribution and its dependencies with barrier thickness and barrier height. Existing carrier transport models are capable of fitting our experimental result for the dependence of the non-uniformity of the carrier distribution on barrier height but do not appear to be able fit our experimental data for the dependence of the non-uniformity of the carrier distribution on barrier thickness. The

experimentally observed dependence with barrier thickness appears to be too strong to be explained using existing carrier transport models.

In this chapter an ambipolar rate equation model is described which is capable of explaining the experimentally observed dependence of the non-uniform carrier distribution on barrier thickness. The model accounts for the electric field produced by the p-i-n junction in which the active region is embedded. The model is able to predict experimental results from thirteen different AMQW laser structures including trends with varying barrier thickness and height.

4.2 Physical Explanation of the Barrier Thickness Dependence

In this section a physical explanation of the experimentally observed dependence of the non-uniform carrier distribution on quantum barrier thickness is given. First, existing carrier transport models are examined. The physical processes which determine the non-uniform carrier distribution predicted theoretically by carrier transport models are described and it is shown why existing carrier transport models do not predict the experimentally observed barrier thickness dependence. Next, we rule out quantum mechanical tunneling as the explanation for the observed barrier thickness dependence by showing that the penetration depth for holes is less than 10 Å for our structures. Finally, we show that if one assumes an electric field is present across the active region then the resulting carrier distribution is capable of fitting the experimentally observed barrier thickness dependence. An explanation for the origin of the electric field is also given.

Two types of carrier transport models exist in the literature; Poisson/continuity equation solvers and ambipolar rate equation models. Nagarajan and Bowers [37] have shown that the two types of carrier transport models result in nearly the same non-uniform carrier distribution. The

reason for the success of the comparatively simplistic ambipolar model is the difference in mobilities between electrons and holes in InP materials. Electrons have a much higher mobility than holes in InP based materials and hence the electrons can rapidly move to eliminate charge separation between the electrons and holes. The electrons move to where the holes are and hence the carrier distribution can be determined simply by finding the distribution of the holes.

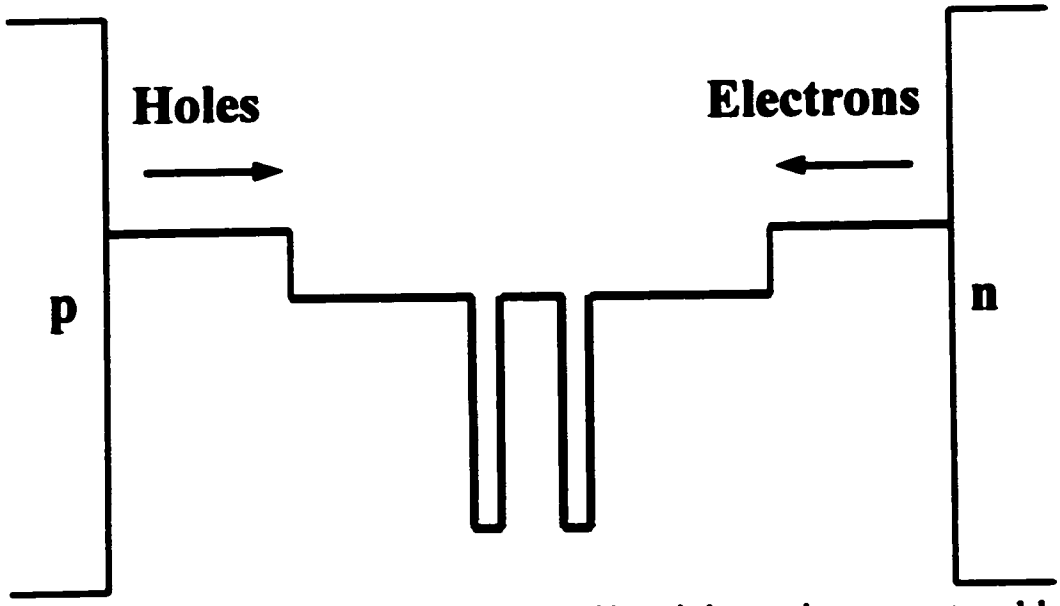

Fig. 4-1 Schematic of a MQW active region used by existing carrier transport models. The active region is assumed to be flat band. "Clouds" of holes are injected from the p-side and electrons are injected from the n-side. The fact that the active region is embedded in a p-i-n junction is ignored.

Carrier transport models begin with a diagram of the active region similar to that shown in Fig. 4-1. The schematic of Fig. 4-1 assumes a heavily forward biased active region which results in a flat band across the MQW active region. Electrons are injected into the active region from the n-side and holes are injected into the active region from the p-side. In the ambipolar approximation we need only look at the holes to determine the carrier distribution. The electrons will move to take on the distribution determined by the holes. For the holes alone we have a text book problem of steady state carrier injection. For an elementary treatment of this problem see

for example chapter 4, section 4.4.4 of Streetman's text book [41]. A fixed density of holes is injected at the p-side edge of the active region and these holes diffuse across the active region. As they diffuse recombination occurs which results in an exponentially decaying carrier density across the active region (assuming a uniform carrier lifetime throughout the material) given by [41],

$$p(x) = p_o \exp\left[\frac{-x}{L_p}\right], \qquad \text{Eq. 4-1}$$

where p(x) is the hole concentration in the 3-D states of the separate confinement heterostructure (SCH), barriers and QWs at a distance x from the p-side of the active region, p_o is the hole concentration at the p-side edge of the active region and L_p is the diffusion length for holes in the material. Note that the carrier density described here is that of the 3-D states above the barriers and wells. The steady state density of carriers captured in the 2-D states of the QWs is determined by a rate equation which balances spontaneous and stimulated recombination and thermionic escape processes with stimulated absorption, and carrier capture processes. The carrier capture rate is determined directly by the carrier density in the 3-D states above the QW (see chapter 5 for a detailed discussion). The diffusion length, L_p, is given by,

$$L_p = \sqrt{D_p \tau_p} \approx 1.6 \times 10^{-2} \sqrt{\tau_p} \ \text{[meters]}, \qquad \text{Eq. 4-2}$$

where D_p is the diffusion constant for the active region material and τ_p is the recombination lifetime in the material.

The recombination rate in the barrier material is relatively small and the diffusion length for holes in the barrier material is roughly 5 to 10 μm. The carrier lifetime at a QW is much smaller due to the high recombination rate in the QW. Thus the hole concentration in the 3-D states will decrease slowly with distance from the p-side of the active region across the SCH and barrier material but will experience sharp drops at the QWs. The bottom curve of Fig. 4-2 is an

example hole distribution in the 3-D states predicted using Eq. 4-1 and Eq. 4-2. The QW active region used in Fig. 4-2 is that of structure 7. The hole concentration decreases slowly with distance from the p-side of the active region across the SCH and barrier material. A diffusion length of 5 μm in the SCH and barrier material was used to generate the bottom curve of Fig. 4-2. The carrier distribution drops sharply at each QW due to the higher recombination rate in the QW and hence shorter carrier lifetime in the 3-D states of the QW material. For the bottom curve of Fig. 4-2 we have assumed that the device is below threshold so that the recombination lifetime for holes in the 2-D states of the QWs is equal to the spontaneous emission lifetime of 1 ns. Under these conditions the carrier capture time for holes in the 3-D states to move to the 2-D states (< 1 ps) is much faster than the recombination time. Therefore the rate at which carriers are taken from the 3-D states above a QW is determined by the rate at which carriers within the QW are recombining, i.e., under steady state conditions the rate at which carriers are captured into the QW must balance the rate at which carriers are depleted from the QW due to recombination. For a spontaneous recombination lifetime of 1 ns and typical carrier densities in the 2-D states of the QWs on the order of 1×10^{24} m^{-3} the diffusion length for holes in the 3-D states of a QW is on the order of 0.1 μm. A diffusion length of 0.1 μm was used for the QW material in the bottom curve of Fig. 4-2.

The bottom curve of Fig. 4-2 is an example of the carrier distribution in the 3-D states predicted by existing carrier transport models. The carrier density decreases slowly with distance from the p-side of the active region due to recombination in the SCH and barriers and then drops sharply at each QW. The sharp drops at the QWs, due to the large amount of recombination in the QWs, are the physical origin of the non-uniform carrier distribution predicted by existing

carrier transport models. These sharp drops at the QWs are responsible for the carrier distribution presented by Nagarajan and Bowers [37].

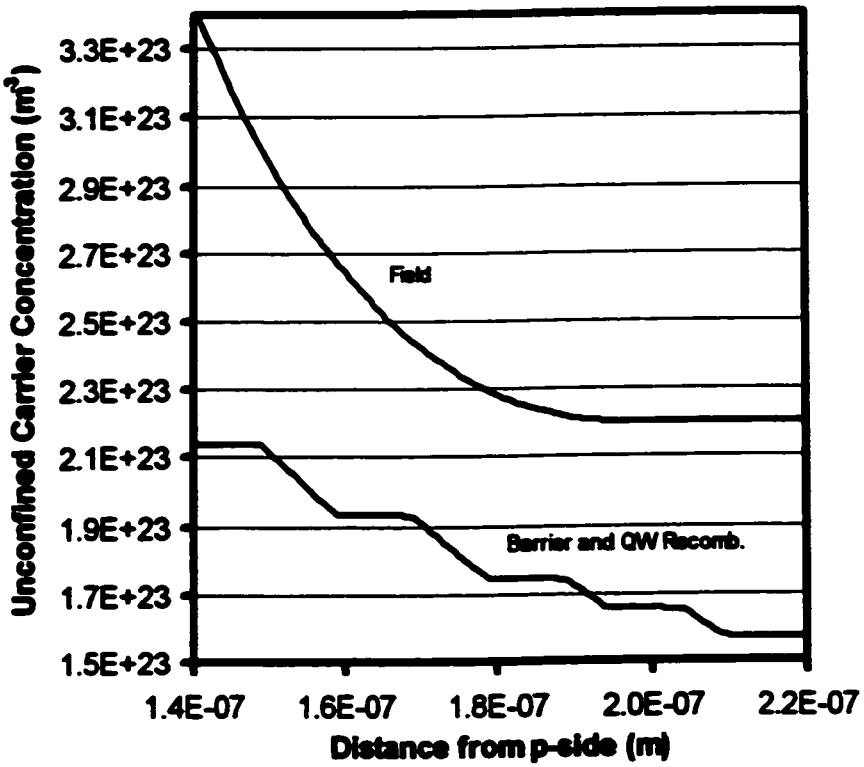

Fig. 4-2 Carrier density in the 3-D state of the SCH, barriers, and QW as a function of distance for structure 7 predicted using different theoretical models. The distribution incorporating recombination in the barriers and QWs is that predicted by existing carrier transport models. The "Field" distribution was used to fit our experimental TCL data.

As can be seen in Fig. 4-2, the carrier distribution predicted by existing carrier transport models has very little dependence on the barrier thickness. The recombination rate in the barriers is small and does not strongly affect the carrier distribution. Nagarajan and Bowers make no mention of the barrier thickness in [37] as the barrier thickness does not affect their theoretical results. Our experimental results obtained using the TCL method demonstrate a strong dependence of the non-uniform carrier distribution on barrier thickness. Existing carrier transport models do not appear to explain this experimental result.

Using the TCL method we have also studied the effect of barrier height on the non-uniform carrier distribution and we have found experimentally that the carrier distribution becomes more uniform with decreasing barrier height. Existing carrier transport models do predict a more uniform carrier distribution with decreasing barrier height and can explain this experimental result. Carrier transport models account for carriers escaping from QWs via thermionic emission and being captured by neighbouring wells resulting in a more uniform carrier distribution. Thermionic emission is strongly dependent on barrier height and so smaller barrier heights result in more uniform carrier distributions. As was shown in chapter 3 Lastip [40], a commercially available Poisson/continuity equation solver, did predict a more uniform carrier distribution with decreasing barrier height (see chapter 3 Fig. 3-5). Lastip did not however predict the experimentally observed dependence with barrier thickness.

The experimentally observed barrier thickness dependence does not appear to be predicted by existing carrier transport models and so we have attempted to find a physical explanation for this result. One possible explanation for the barrier thickness dependence is that some type of charge transfer exists between the QWs which results in a more uniform carrier distribution and grows stronger the closer the QWs are together. Such a transfer cannot be explained classically but could be due to quantum mechanical tunneling. The penetration depth (distance at which the wavefunction drops to 1/e of its value at the edge of the QW) is given by [1],

$$\delta_{pen} = \frac{\hbar}{\sqrt{2m^*(U-E)}}, \qquad \text{Eq. 4-3}$$

where m^* is the effective mass, U is the barrier height of the QW and E is the energy of the particle in the well. For the QWs in structures 5 through 12 the penetration depth for holes in the valence band QWs is 5.78 Å and the penetration depth for electrons in the conduction band QWs

is 27.8 Å. For barriers as thin as 30 Å such as those used in structures 11 and 12 significant electron tunneling can occur between the wells. This increase in ease of electron transport between wells will improve the validity of the ambipolar model. The hole penetration depth of roughly 6 μm is too small for there to be significant tunneling of holes through barriers as thick as 30 Å or 50 Å. Thus quantum tunneling between the wells cannot explain the observed dependence of the non-uniform carrier distribution on barrier thickness.

The decrease in hole concentration in the 3-D states with distance from the p-side of the active region predicted by Poisson/continuity equation solvers and ambipolar models (bottom curve of Fig. 4-2) is due to the recombination of carriers in the SCH, barrier and QW material. Holes are injected from the p-side of the active region and diffuse across the active region. The concentration of holes decreases with distance from the p-side edge of the active region as holes are lost to recombination. A second possible physical mechanism exists which will also result in the hole concentration decreasing with distance from the p-side edge of the active region. If an electric field is present in the active region and which opposes the diffusion of the holes, then the hole concentration will decrease with distance from the p-side edge of the active region as diffusing holes are turned back by the electric field [42]. The diffusion current in an electric field is described by Boltzmann statistics and the carrier density in the 3-D states in the presence of an electric field is a function of distance from the p-side of the active region and is given by,

$$p(x) = p_o \exp\left[\frac{-qV(x)}{kT}\right], \qquad \text{Eq. 4-4}$$

where p(x) is the hole concentration in the 3-D states above the barriers and wells at a distance x from the p-side of the active region, p_o is the hole concentration at the p-side edge of the active region, q is the electronic charge, k is Boltzmann's constant, T is the temperature, and V(x) is the

electric potential at a point x due to the electric field. The existence of a small electric field can have a strong effect on the carrier distribution. An electric field of magnitude 1×10^{-3} V/cm has a similar effect on the carrier distribution as a diffusion length due to recombination of 0.1 μm as was used for the QW material in Fig. 4-2. The "field" distribution shown in Fig. 4-2 was used to fit our experimental data with barrier thickness. The field causing the distribution shown in Fig. 4-2 is small but still results in large drops in the carrier density across the barriers unlike recombination in the barriers. In this chapter we describe a simple ambipolar rate equation model which assumes the existence of a small electric field across the MQW active region and determines the carrier distribution resulting from such a field. The model is able to fit the experimentally observed barrier thickness dependence of the non-uniform carrier distribution to within experimental uncertainty. Furthermore, the simple model we have developed is capable of fitting the experimental results of all thirteen AMQW laser structures we have grown and tested to within experimental uncertainty.

The experimental TCL data on the non-uniform carrier distribution can be fit by assuming an electric field exists across the active region. I'll now discuss the physical origin of the electric field. A conventional MQW laser is a p-i-n junction diode. In particular our devices are P^+-n-N^+ heterostructure devices. Any p-i-n junction device has transition regions where large electric fields exist at the edges of the intrinsic region (p-i and i-n junctions). Most carrier transport models in the literature ignore the p-i and i-n junctions and assume that the p-i and i-n transition regions are small compared with the width of the intrinsic region [36,37,43]. For convenience I will call this the flat band assumption. In the flat band assumption the QWs are located in the middle of the neutral intrinsic region and carriers are injected from the edges of the active region across the p-i and i-n junctions. To my knowledge, all existing ambipolar models make the flat

band approximation. Most Poisson/continuity equation solvers appear to make the flat band approximation. Poisson/continuity equation solvers are, in principle, capable of calculating the effects of the p-i and i-n junctions however most are of the type described by Tessler and Eisenstein [36] which uses the flat band assumption and treats current injection at the edges of the active region as a boundary condition rather than properly solving the effects of the p-i and i-n junctions.

The flat band assumption appears to date back to the 1950s when heavily forward biased p-i-n junction theory was first being developed [44,45]. In early work the flat band assumption was made for devices with intrinsic regions tens of microns wide. The transition region widths for these devices were on the order of 0.1 μm so that the flat band assumption was certainly valid. For MQW diode lasers the transition width can vary from a few hundred angstroms to a few thousand angstroms depending on the doping concentrations of the p and n materials and the background doping of the intrinsic material. The extent of the transition region is also dependent on material parameters such as band gap and dielectric constant, the existence of hetero-interfaces, and the bias voltage required to reach threshold. The intrinsic region in MQW lasers is typically only a few thousand angstroms across and hence the assumption that that the p-i and i-n transition regions are small compared with the width of the intrinsic region may or may not be valid depending on the specifics of the p-i-n junction MQW device. It does not appear as though the flat band assumption is valid for our devices. The P^+-n transition region appears to extend into the MQW active region of our devices and the resulting electric field accounts for the experimentally observed dependence on barrier thickness.

4.3 Theoretical Model

In this section the theoretical model used to fit the experimental TCL data presented in chapter 3 is described. The model is an ambipolar rate equation model which incorporates an electric field into the pumping mechanism. The electric field due to the transition regions at the P^+-n and n-N^+ junctions is calculated using the depletion approximation and the carrier density in the 3-D states across the active region resulting from this field is calculated. The current into each QW is determined through carrier capture of the carriers in the 3-D states of each QW. Rate equations for each QW are solved which balance the carrier capture current with carrier escape through thermionic emission and carrier recombination through spontaneous and stimulated emission. The rate equations determine the carrier densities in each well which are then used to determine the gain profile for the complete MQW active region. The gain peak wavelength at threshold is plotted as a function of cavity length to determine theoretical TCL data which is then compared to the experimental TCL data provided in chapter 3.

4.3.1 Calculation of Material Parameters and Gain

Vergard's interpolation [46] was used to determine the hydrostatic deformation potential (a), the shear deformation potential (b), the elastic stiffness constants (C_{ij}), the effective masses of the conduction and valence bands and the hole mobility. The binary material parameters used in the Vergard interpolation formula were taken from [46]. The hydrostatic deformation potential for the conduction and valence band were taken to be $a_c = (2/3)a$ and $a_v = a/3$ [46]. The energy gap for the quaternary material was calculated using Nahory's formula [46] for unstrained material and Kuphal's formula [46] for strained material. Strain was accounted for by shifting the barrier and well conduction and valence bands according to the relations in [47]. The conduction

band and valence band finite quantum well energy levels were calculated numerically and the transition energies were determined. Transition energies were calculated for all the confined energy levels but it was found that for n > 1 transitions the transition energies were too high to contribute to the region of the spectrum we are concerned with. Hence, all gain calculations were done for the n = 1 transition alone.

The material gain of a quantum well was calculated for a given carrier density in the following way. First the quasi-Fermi levels were calculated for the given carrier density using

$$E_{Fc} = E_t + kT\ln\left(e^{N\pi\hbar^2 L_z/m_c kT} - 1\right), \qquad \text{Eq. 4-5}$$

$$E_{Fv} = 0 - kT\ln\left(e^{P\pi\hbar^2 L_z/m_v kT} - 1\right). \qquad \text{Eq. 4-6}$$

Next the beginning and end energies of the transition were calculated as [47]

$$E_2 = E_c + (m_r/m_c)(h\nu - E_t), \qquad \text{Eq. 4-7}$$

$$E_1 = E_v - (m_r/m_v)(h\nu - E_t), \qquad \text{Eq. 4-8}$$

$$E_2 - E_1 = h\nu, \qquad \text{Eq. 4-9}$$

and the quasi-Fermi functions and density of states were calculated from

$$F_c = \frac{1}{e^{(E_2 - E_{Fc})/kT} + 1}, \qquad \text{Eq. 4-10}$$

$$F_v = \frac{1}{e^{(E_1 - E_{Fv})/kT} + 1}, \qquad \text{Eq. 4-11}$$

$$\left.\begin{aligned} \rho(h\upsilon) &= 0 \\ \rho(h\upsilon) &= \frac{m_r}{\pi\hbar^2 L_z} \end{aligned}\right\} \begin{aligned} h\upsilon &< E_t \\ h\upsilon &\geq E_t \end{aligned} \qquad \text{Eq. 4-12}$$

The material gain was calculated using [48],

$$g_{mat}(h\nu) = \frac{C_o}{h\nu} \cdot \left|I_h^e\right|^2 \cdot \left|e \cdot p_{cv}\right|^2 \cdot \rho(h\nu) \cdot \left(F_c - F_v\right), \quad \text{Eq. 4-13}$$

$$C_o = \frac{\pi q^2 \hbar}{n_r c \varepsilon_o m_o^2}. \quad \text{Eq. 4-14}$$

$\left|e \cdot p_{cv}\right|^2$ is the momentum matrix and I_h^e is the overlap integral of the conduction and valence band envelope functions. The terms $C_o \cdot \left|I_h^e\right|^2 \cdot \left|e \cdot p_{cv}\right|^2$ were calculated for our structures using a commercially available laser simulator [40]. The material gain was convolved with a Lorentzian lineshape function given by [48],

$$L = \frac{\hbar / \pi\tau_{in}}{\left(\hbar / \tau_{in}\right)^2 + \left(E - E_{21}\right)^2}, \quad \text{Eq. 4-15}$$

and τ_{in} was taken to be 0.1 ps [49].

The modal gain for a quantum well was then calculated by multiplying the material gain by the optical overlap, Γ_λ. Γ_λ was calculated by evaluating the overlap integral between the area of the quantum well and the optical mode. The optical mode was calculated using the effective index method [50]. Γ_λ was found to be proportional to the thickness of the QW as expected. Finally, the total gain of the laser was taken to be the sum of the modal gains of each well.

4.3.2 Rate Equation Model

The carrier densities in each well were determined using a rate equation model. Under steady state conditions the rate of carriers entering each well must equal the rate at which carriers are depleted from the well. Our rate equation for each well incorporated a direct pumping current into the well, an indirect pumping current into the well, an escape current out of the well, a recombination current due to stimulated emission, a recombination current due to spontaneous emission, and optical pumping of a well by the optical field produced by the other wells. The

direct pumping, indirect pumping and escape currents are described in the following two subsections. The spontaneous emission rate was assumed to be proportional to the population of the well and a spontaneous emission lifetime of 1 ns was assumed. The stimulated emission rate was calculated using the gain curve as was the stimulated absorption current which accounts for optical pumping from the other wells. The carrier densities in all the wells were solved for self consistently and once the carrier densities of each well were known a gain spectrum for the device was calculated. The peak gain of the device was then equated to the laser threshold condition to determine the lasing wavelength at threshold for the device. Lasing wavelength at threshold was then plotted versus cavity length to determine the theoretical TCL for the structure.

4.3.3 Electrical Pumping Model

In this section we describe the model used to determine the electrical pump current going into the wells of our AMQW lasers.

The voltage profiles across the P^+-n-N^+ junctions of our devices are calculated in the depletion approximation in the manner described by Chuang in chapter 2 of his text book [51]. The calculated voltage profile for structure 7 is plotted for holes in Fig. 4-3 for bias voltages of 0 V and 1.15 V. According to our model our devices reach threshold near 1.15 V bias. The voltage profiles were calculated according to [51] using $P^+ = 2 \times 10^{23}$ m^{-3} and $N^+ = 1 \times 10^{24}$ m^{-3}, as was grown, and assuming an n-type background doping of 5×10^{21} m^{-3} in the intrinsic region, which is typical for intrinsic quaternary material grown with our MBE facility. Fig. 4-3 demonstrates that, for our structures, the QWs lie at the edge of the transition region of the P^+-n junction resulting in a small but non-negligible field across the QW region. The voltage profile at

a bias of 1.15 V, shown in Fig. 4-3, resulted in carrier distributions which fit our experimentally observed barrier thickness dependence to within experimental uncertainty.

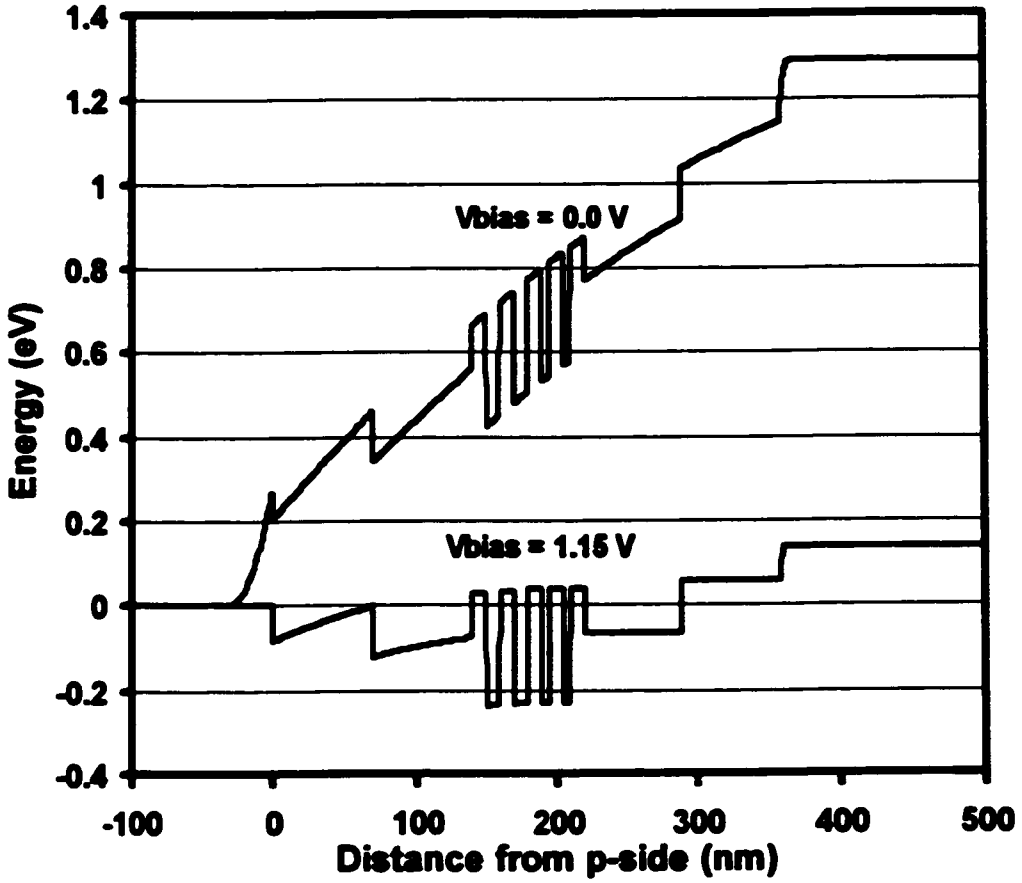

Fig. 4-3 Calculated valence band energy profile across the active region.

If the wells lie in the junction transition region then we know, from established p-n junction theory, that the current pumping the wells is dominated by the diffusion current. The diffusion current is described by classical Boltzmann statistics [42]. The holes in the p-doped region are diffusing around and a certain number, which is proportional to the doping of the p-side N_a, approach the junction each second. Most of this current is turned back by the potential barrier qV at the junction and only the fraction $e^{-qV/kT}$ overcome the barrier. As is shown in Fig. 4-4, there is a barrier qV_1 between the p-side and the first well and qV_2 between the p-side and

the second well. Boltzmann statistics tells us that the population in the 3-D states (energies above the barriers) at any point, x, in the active region is given by $P_{3\text{-}D}(x) = N_s e^{-qV(x)/kT}$. The population in the 3-D states of a well is then,

$$P_w^{3\text{-}D} = \frac{N_s}{2}\left(e^{-qV_w/kT} + e^{-q(V_w+\Delta V_w)/kT}\right), \qquad \text{Eq. 4-16}$$

where w is the index of the well from the p-side of the active region and V_w and ΔV_w are defined explicitly for the first two wells in Fig. 4-4. We have assumed that the field is linear across the well for the purpose of taking the average population. This assumption is reasonable for distances as small as the well thicknesses. The carriers above the well are captured into the well at a rate described by the carrier capture time such that the current into a well, called the *direct pumping current*, I_{dir}, is given by,

$$I_{dir} = \frac{qAL_w P_w^{3\text{-}D}}{\tau_{cap}}. \qquad \text{Eq. 4-17}$$

A is the cross sectional area of the device, L_w is the well thickness, and τ_{cap} is the hole capture time.

In chapter 5 we describe the relation between carrier capture and escape rates. Using the equilibrium condition we find that the escape current out of a QW (from the 2-D confined states into the 3-D unconfined states) is given by (see chapter 5),

$$I_{esc} = \frac{qAL_w P_{2D}}{\tau_{cap}} \sqrt{\frac{N_{c3D}N_{v3D}}{N_{c2D}N_{v2D}}} \exp\left[-\frac{E_{barrier} - E_{level} - E_{Fv}}{kT}\right]. \qquad \text{Eq. 4-18}$$

where q, A, L_w, and τ_{cap} are the same as were used in the I_{dir} equation, k is Boltzmann's constant, T is temperature, P_{2D} is the population density of the well, and N_{xxD} are the effective densities of states for the 2-D and 3-D states of the conduction band and valence band QWs (see chapter 5 for a complete derivation). $E_{barrier}$ is defined in Fig. 4-4 and for the valence band in InGaAsP is 0.6 of

the difference in band gaps between the barrier and well material. E_{level} is the energy of the QW energy level above the bottom of the well. E_{Fv} is the quasi-Fermi energy for the well and accounts for the fact that as the well fills the carriers will be in higher energy states and not have as high a barrier to overcome when escaping the well.

The escape current from one well can pump the other wells in the active region. Again we assume that the pumping of wells is dominated by diffusion currents. The escape current from a well will increase the carrier densities above the other wells in the active region and hence increase the pumping to those wells. This additional pumping current is called the *indirect pumping current*, I_{indir}.

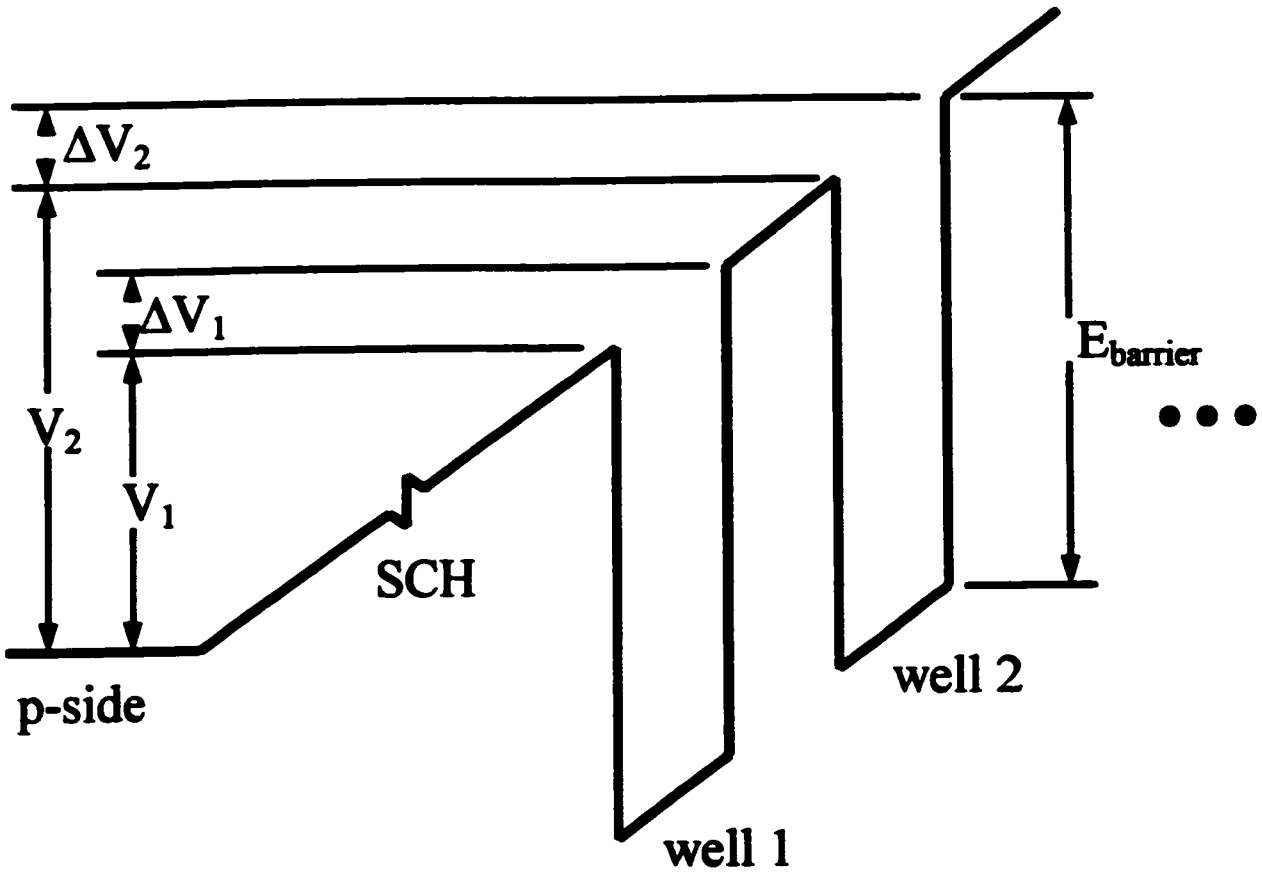

Fig. 4-4 Schematic showing the potential barrier across the active region that the hole diffusion current must overcome to pump the quantum wells.

4.4 Modeling Results

In this section the major successes of the model described in the previous section are discussed. The model predicts the existence of the TCL in AMQW lasers and provides a physical understanding of the origin of the TCL. The carrier distribution predicted by the model has a strong dependence on barrier thickness due to the existence of the electric field and the model is able to fit our experimental barrier thickness data to within experimental uncertainty; a result that could not be obtained using existing carrier transport models. The model is not only capable of predicting the experimentally observed barrier thickness dependence but is capable of fitting, to within experimental uncertainty, the experimental data taken from all thirteen AMQW laser structures we have studied experimentally.

4.4.1 Origin of the TCL

Using the gain model described above we can explain the physical origin of the TCL in AMQW lasers. Fig. 4-5 shows the material gain versus wavelength as a function of carrier density for structure 7 assuming a uniform carrier distribution so each well has the same carrier density. The thick wells reach transparency at lower carrier densities than the thin wells due to the well known Bernard-Duraffourg condition which states that in a bipolar semiconductor laser gain is provided to photons with energies ($\hbar\omega$) that are greater than the band gap and smaller than the difference in conduction band and valence band quasi-Fermi levels or stated mathematically [48],

$$E_g' < \hbar\omega < E_{fc} - E_{fv},$$

where E_g' is the energy gap between the n = 1 energy levels in the conduction band and valence band QWs and E_{fc} and E_{fv} are the quasi-Fermi levels for the conduction band and valence band

QWs. Thick wells have a lower transition energies than thin wells meaning E_g' is smaller for thick wells so thick wells provide gain for a smaller separation of quasi-Fermi levels (smaller carrier densities) than thin wells. In general, QWs with smaller transition energies (longer wavelengths) will provide gain for lower carrier densities than QWs with higher transition energies. Thus at low carrier densities the gain peak is at wavelengths corresponding to the thick wells. At higher carrier densities the thin wells also reach transparency. The thick wells continue to provide more gain than the thin wells. However, the thick wells also provide gain at wavelengths corresponding to the gain peak wavelength of the thin wells. For high enough carrier densities the sum of the gain from the thin and thick wells at the wavelength corresponding to the gain peak of the thin wells overtakes the gain of the thick wells at the gain peak of the thick wells. Devices with long cavity lengths reach threshold at low carrier densities when the total gain peak corresponds to the gain peak of the thick wells. Devices with short cavity lengths require higher carrier densities to reach threshold and at high carrier densities the total gain peak is at a wavelength corresponding to the gain peak of the thin wells. Fig. 4-6 shows the lasing wavelength at threshold versus cavity length for structure 7 again assuming a uniform carrier distribution (i.e., the same carrier density in each well). One can see that in an AMQW laser there exists a TCL above which the laser initially reaches threshold on the thick wells and below which the device initially reaches threshold on the thin wells. If the carrier distribution is assumed to be uniform, as was done in this simulation, then the mirror image structure, structure 8, has precisely the same TCL as structure 7. The experimental observation that the TCL is different for mirror image AMQW structures demonstrates that the carrier distribution is not uniform. The TCL is a general property of AMQW lasers and is not an artifact of the non-uniform carrier distribution. The difference in

TCLs between mirror image AMQW laser structures is, however, due to the non-uniform carrier distribution.

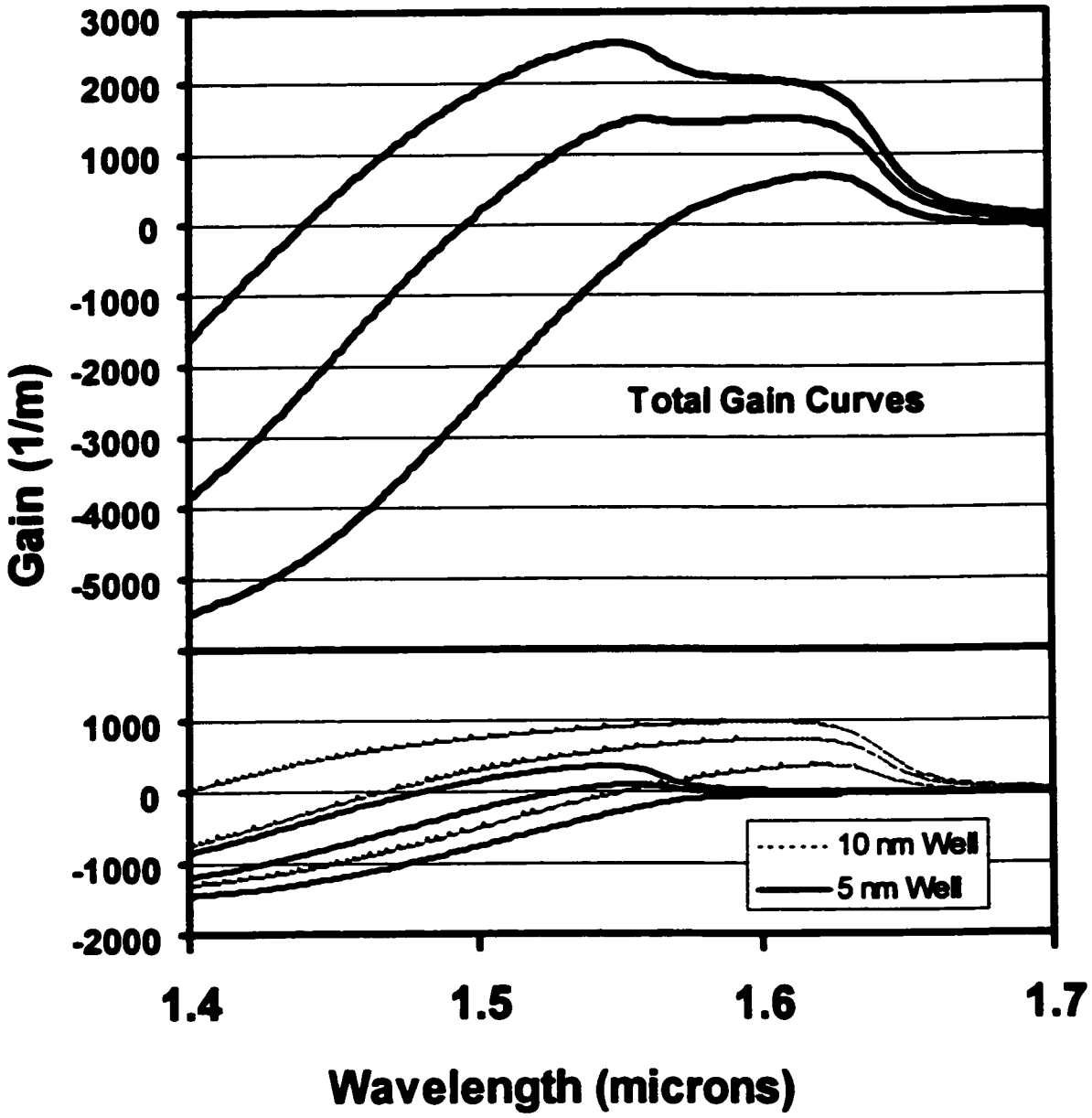

Fig. 4-5 Gain curves for AMQW devices assuming a uniform carrier density amongst all the QWs. Gain curves for carrier densities of 1.5×10^{24} m^{-3}, 2.25×10^{24} m^{-3} and 3.0×10^{24} m^{-3} are shown. The bottom graph shows the gain curves of the individual 100 Å and 50 Å wells at all three carrier densities while the top graph shows the sum of the individual gain curves at each carrier density. The sum of the gain curves due to the individual wells gives the total gain for the AMQW laser.

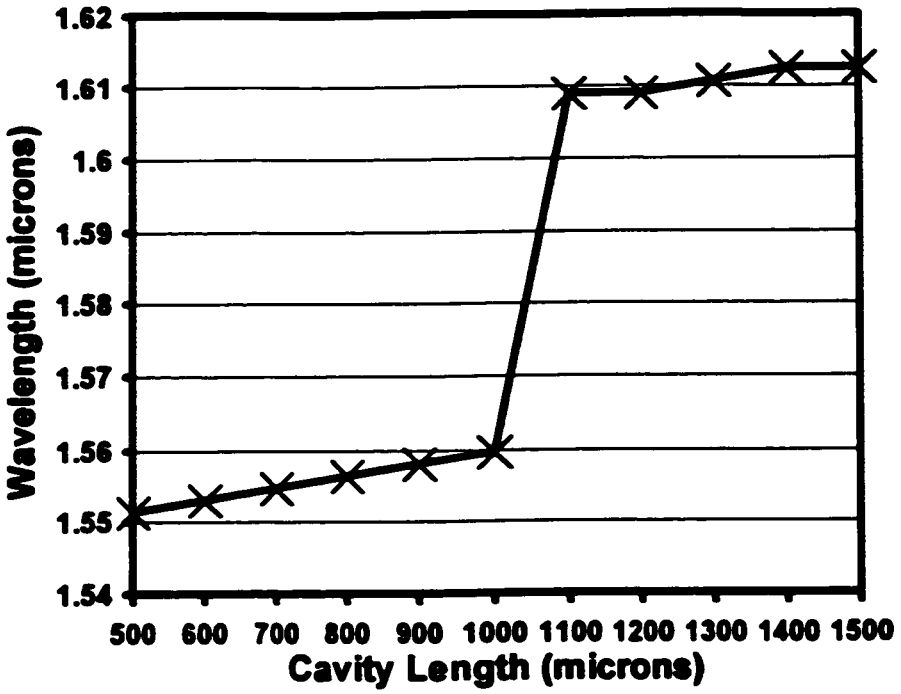

Fig. 4-6 Theoretical plot of wavelength of operation at threshold versus cavity length for structure 7 assuming a uniform carrier density in all the QWs.

4.4.2 Barrier Thickness Dependence

Our electric field, ambipolar rate equation model was developed to explain the large dependence of the non-uniformity of the carrier distribution on quantum barrier thickness. Theoretical plots of the wavelength at threshold versus cavity length for structures 7 through 10 are shown in Fig. 4-7. These theoretical plots can be compared to Fig. 3-10 and Fig. 3-13 of chapter 3 which show the experimentally determined curves. The fitting procedure is described in the next section and the parameters used to fit structures 7 through 10 are given in Table 4-1. TCLs of 950 μm and 550 μm for structures 7 and 8 respectively and of 650 μm and 550 μm for structures 9 and 10 were obtained using the model. The theoretical results match the experimentally measured results to within experimental uncertainty. The quality of the fit

demonstrates that our electric field model accurately describes the barrier thickness dependence of the carrier distribution in MQW lasers.

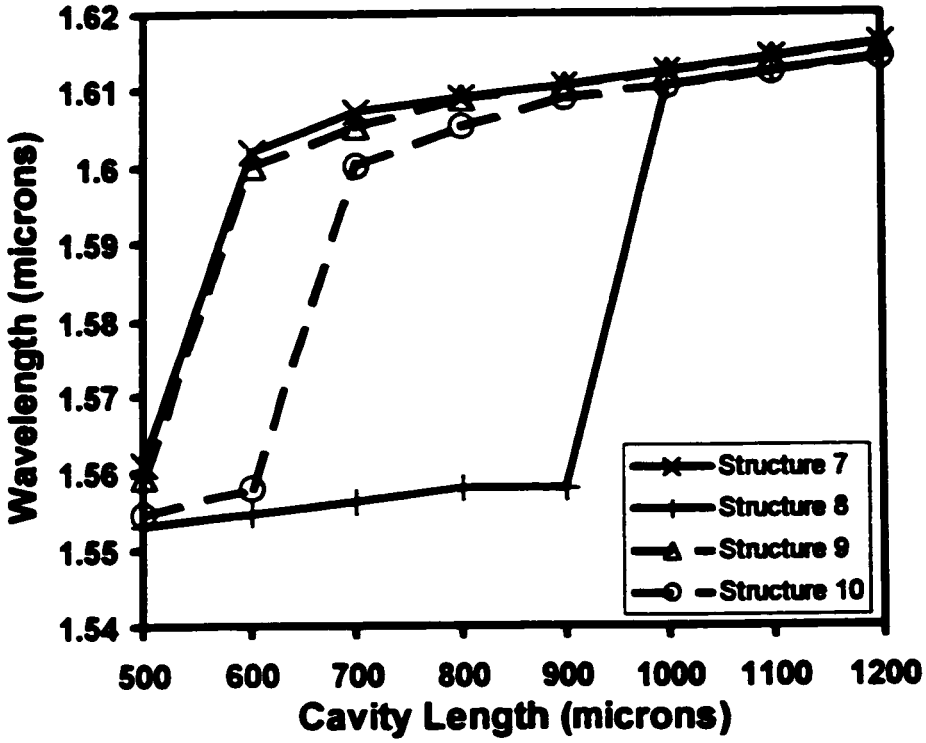

Fig. 4-7 Theoretically calculated plots of lasing wavelength at threshold versus cavity length for structures 7 - 10. The dashed lines are for the structures with 50 Å barriers and the solid lines are for the structures with 100 Å barriers.

4.4.3 Fit to All Thirteen Laser Structures

The measured and theoretically predicted TCLs for all 13 structures are presented in Table 4-1. Table 4-1 demonstrates that the theoretically predicted TCLs match those measured experimentally to within the experimental uncertainty. Two fitting parameters were used to fit the data: the quantum well carrier capture time, τ_{cap}, and the loss per unit length, α.

A quantum well capture time of 60 psec was used to fit all the experimental data. This is consistent with theoretical capture times reported in the literature [49] but is substantially larger than the currently accepted hole capture time of $\approx$ 0.25 ps which has been determined

experimentally for InGaAs/InP quantum wells [37]. I believe the carrier capture time in my model is large because it is compensating for the use of the depletion approximation when calculating the field across the junction. The field across the active region which fits the barrier thickness data will be obtained for a smaller applied bias than is predicted by the depletion approximation. As a result the necessary field will exist when there are higher carrier densities in the 3-D states across the active region. This means that to reach threshold when the necessary field exists the carrier capture time will have to be smaller than is predicted by my model. To determine the field correctly one must write a Poisson/continuity equation solver which calculates the fields in the transition region while accounting for the fields from the carriers in the transition region. Our group is in the process of writing such a solver. The simple depletion approximation can be used to determine the electric fields in the transition region as long is one is willing to compensate for the approximation by using a large carrier capture time in the model. One could just as well use the accepted carrier capture time of 0.25 ps in the model and add a fudge factor to the depletion approximation field calculation to compensate for the approximation.

Structure	Experimental TCL ± 100 μm	Theoretical TCL (μm)	α (m^{-1})	Experimental $g_{thick} / \hat{g}_{thick}$	Theoretical $g_{thick} / \hat{g}_{thick}$
1	550	550	1300	2.09	1.91
2	1150	1050	2025		
3	850	850	1175	1.18	1.29
4	1000	1100	1175		
5	1800	1700	975	1.28	1.41
6	2300	2400	975		
7	550	550	1400	1.73	1.73
8	950	950	1400		
9	550	550	1200	1.18	1.18
10	650	650	1200		
11	< 600	550	1200	N/A	1.18
12	650	650	1200		
13	≈ 250	250	1000	N/A	N/A

Table 4-1 Experimental and theoretical TCL data and fitting parameters.

α is tabulated along with the theoretical TCLs in Table 4-1. α was kept nominally the same for all mirror image structures (except one) so that the difference between TCLs for mirror image structures was predicted entirely by the physical parameters in the model such as I_{dir}. We were not, however, able to fit structure 2 using the same α as structure 1. α was 725 m^{-1} higher for structure 2 than for structure 1. Measured threshold current densities for structure 2 were found to be, on average, twice as high as for structure 1 indicating that α is in fact larger for structure 2 than for structure 1. Structure 1 and 2 were processed at different times while all other pairs of mirror image structures were processed simultaneously. Differences in the processing conditions could easily account for the difference in α between structures 1 and 2.

4.5 Conclusion

In chapter 3 we described the TCL method which has provided the first quantitative experimental data on the degree to which the non-uniform carrier distribution affects the gain of QWs at different locations in the active region. The TCL method was used to quantitatively study the effect of quantum barrier height and thickness on the non-uniformity of the carrier distribution. We found experimentally that decreasing the barrier height results in a more uniform carrier distribution and decreasing the barrier thickness results in a more uniform carrier distribution. The dependence with barrier height is predicted by existing carrier transport models and is the result of increased thermionic emission from wells with smaller barrier heights. The dependence of the non-uniform carrier distribution on barrier thickness does not appear to be predicted by existing carrier transport models.

We have developed a simple ambipolar rate equation model which incorporates the effects of an electric field across the MQW active region when determining the electrical pump current

into each well. The field appears to be the result of the P^+-n junction transition region extending into the MQW active region. The model predicts the experimentally observed dependence on quantum barrier thickness. The model is also capable of fitting all the experimental TCL results presented in chapter 3 to within experimental uncertainty.

5. CHAPTER 5 – CARRIER CAPTURE AND ESCAPE

5.1 Introduction

Three different approaches to modeling carrier capture and carrier escape for a QW are reported in the literature. All approaches treat the QWs in the conduction band and valence band as 2 level systems. For the conduction band QW the electrons can be in the 2-D confined states of the QW or they can be in the 3-D unconfined states of the QW, higher in energy than the barriers as depicted in Fig. 5-1. Similarly for the valence band QW the holes can either be in the 2-D confined states or the 3-D unconfined states. Carrier transport models assume that there is an interaction between the 2-D and 3-D states in the conduction band and valence band QWs such that the rate at which carriers move from the 3-D states to the 2-D states, called the carrier capture rate, R_{cap}, is given for electrons in the conduction band by,

$$R_{cap} = \frac{Vn_{3D}}{\tau_{cap}}, \qquad \text{Eq. 5-1}$$

where n_{3D} is the number of electrons in the unconfined levels per unit volume, τ_{cap} is a phenomenological term describing the strength of the interaction between the 2-D and 3-D states called the capture time, and V is the volume of the interaction region which will be discussed in the following paragraph. Similarly, the rate at which carriers move from the 2-D states to the 3-D states, called the carrier escape rate, R_{esc}, is given for electrons in the conduction band by,

$$R_{esc} = \frac{Vn_{2D}}{\tau_{esc}}, \qquad \text{Eq. 5-2}$$

where n_{2D} is the number of electrons in the 2-D confined levels per unit volume, and τ_{esc} is a phenomenological parameter called the escape time.

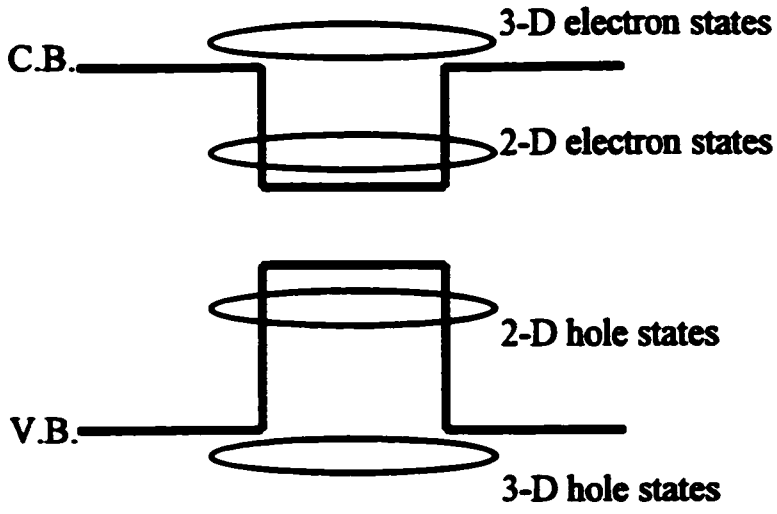

Fig. 5-1 The conduction band and valence band QWs as two state systems.

In the literature, different models use different values for the volume of the interaction region, V, in Eq. 5-1 and Eq. 5-2. In the next section the equilibrium condition is used to develop a relation between the carrier capture and escape times. The analysis is independent of the choice of the interaction region volume as long as the carrier capture and carrier escape interaction volumes are equal. We assume the interaction volumes for carrier capture and escape are equal as is done in carrier transport models in the literature. It is however possible that the volumes are different. The volume of 3-D states interacting with the 2-D states of the QW could be larger than the volume of the QW. This will not, however, significantly affect the analysis presented in this chapter. If the volume of the 3-D states is different from the volume of 2-D states then a ratio of the two volumes will appear in the relation between the capture and escape times and a weighted average of the effective densities of states for the 3-D states in the QW and the 3-D states in the barrier material must be used. For our analysis we assume that the volumes are the same and we assume that the interaction volume is equal to the volume of the QW, $V = AL_z$, where A is the cross sectional area of the QW and L_z is the thickness of the QW. As will be discussed later in this chapter, we have found that the L_z dependence of the interaction volume is

required to fit our experimental data for AMQW structures. The volume of the 2-D states can be determined by finding the width of the wavefunction for the holes or electrons in the energy levels of the QW. As discussed in Chapter 4, for our structures the wavefuntions for the holes extended with significant amplitude only 7 angstroms into the barriers so that, to an excellent approximation, the volume of the 2-D states for a QW is the volume of the QW.

There are three different approaches in the literature to modeling carrier capture and escape for a QW. The first and by far most popular approach is to assume that the carrier capture and carrier escape times are independent. In these models experimentally determined values for the carrier capture and carrier escape times are often used. In other models of this type [37,52] an experimentally determined value for the capture time is used while the carrier escape time predicted by classical thermionic emission theory is used [53].

The second approach in the literature [54, 55] states that the capture and escape times must be related in order to satisfy the equilibrium condition *when the device is at equilibrium* (i.e., no applied bias). Tessler *et. al.* [54] expressed this condition for electrons in the conduction band as,

$$R_{cap} - R_{esc} = \frac{\eta_{FN} n_{3D} - n_{2D}}{\tau_{cap}}, \qquad \text{Eq. 5-3}$$

$$\eta_{FN} = \frac{n_{2D}^{F}}{n_{3D}^{F}}, \qquad \text{Eq. 5-4}$$

where R_{cap}, R_{esc}, n_{3D}, n_{2D}, and τ_{cap} are as defined above and n^{F}_{2D} and n^{F}_{3D} are the carrier densities in the 2-D and 3-D states when the device is at equilibrium. Ishikawa *et. al.* [55] expressed the "equilibrium at equilibrium" condition for electrons in the conduction band as,

$$\tau_{esc} = \frac{n_{2D}^{F}}{n_{3D}^{F}}\tau_{cap} = \left(\frac{\log\left[1+\exp\left(E_F / kT\right)\right]}{\log\left[1+\exp\left(\left[E_F - E_{bc}\right]/kT\right)\right]} - 1 \right)\tau_{cap}, \qquad \text{Eq. 5-5}$$

where E_F is the equilibrium Fermi level, k is Boltzmann's constant, T is temperature, and E_{bc} is the barrier height of the conduction band QW measured from the energy of the first quantized level to the energy of the barrier.

The third approach in the literature assumes that the 2-D and 3-D carrier densities are in equilibrium when the device itself is under bias and away from equilibrium. Stated another way, the 2-D and 3-D states have the same quasi-Fermi level. The equilibrium under bias approach is expressed by Tessler *et. al.* [36] for electrons in the conduction band as,

$$n_{2D} = \eta_F n_{3D}, \qquad \text{Eq. 5-6}$$

$$\eta_F = \frac{\int \rho_{c2D}(E) f_c(E, E_{fc}, T) dE}{\int \rho_{c3D}(E) f_c(E, E_{fc}, T) dE}, \qquad \text{Eq. 5-7}$$

where ρ_{c2D} and ρ_{c3D} are the densities of states for the 2-D and 3-D states in the conduction band, f_c is the Fermi function, and E_{fc} is the conduction band quasi-Fermi level for a device under bias. The "equilibrium under bias" approach rests on the assumption that the carrier capture and escape times are much faster than the other processes affecting the carrier densities in the 2-D and 3-D states such as optical recombination across the band gap. The capture time has been found experimentally to be less than 1 ps for holes in InP/InGaAs QWs, which is much faster than the spontaneous emission lifetime in a QW. Below threshold spontaneous emission will be the dominant recombination process. Thus, the assumption of equilibrium carrier densities in the 2-D and 3-D states seems to be valid at least below threshold. An interesting point is that the carrier densities in the different sub-bands of a QW (n = 1, 2, ...) are always assumed to be in equilibrium, having a single quasi-Fermi level. The assumption that the carrier densities in the sub-bands of a

QW are in equilibrium under bias is similar to the assumption that the 2-D and 3-D states of a QW are in equilibrium under bias.

Of the three approaches to treating carrier capture and escape in the literature the first is by far the most common but is physically incorrect. Models using the first approach do not satisfy the equilibrium condition *at equilibrium*. When a QW device is at equilibrium and without an applied bias, models using the first approach allow net current flow into or out of the QWs.

We have used the second approach in our model. In the next section we use the second approach to derive a relation between the carrier capture and escape times which must be true for the equilibrium condition to be satisfied at equilibrium. The relation we derive is physically equivalent to the condition presented by Tessler *et. al.* [54] (Eq. 5-3 and Eq. 5-4) but unlike Eq. 5-3 and Eq. 5-4 we present an analytic mathematical relation between the carrier capture and escape times which is easy to implement and displays the critical dependencies of the carrier capture and escape times. The relation we derive is similar to Ishikawa's [55] relation (Eq. 5-5) but includes the effects of the different densities of states of the 2-D and 3-D states. In the following sections we show that the well thickness dependence of our model is critical when fitting data taken from AMQW lasers with different thickness QWs in the same active region. It is also shown that the capture time predicted by classical thermionic emission theory has a QW thickness dependence that cannot fit our experimental data.

5.2 Semiconductor Quantum Wells in Thermal Equilibrium

The rates at which carriers enter and leave a quantum well, given by Eq. 5-1 and Eq. 5-2, must balance each other when the device is at equilibrium. In this section we examine a QW device *at equilibrium* (no applied bias) and use the equilibrium condition to determine a relation

between the capture and escape times that *must be true* for the QW device to satisfy the equilibrium condition. The entire analysis is done at equilibrium.

As we are working at equilibrium we can make several simplifying approximations such as the use of effective densities of states and an approximated Fermi function. The analysis can easily be carried out without making such approximations and a relation between the carrier capture and escape times found. The result without approximations for the electrons in the conduction band is,

$$\tau_{esc}^{e} = \frac{\int \rho_{e2D}(E) f(E) dE}{\int \rho_{e3D}(E) f(E) dE} \tau_{cap}^{e}, \qquad \text{Eq. 5-8}$$

where ρ_{3D} and ρ_{2D} are the densities of states for the 3-D and 2-D states in the conduction band, f(E) is the Fermi function, and E_F is the *equilibrium* Fermi level. While perfectly correct, Eq. 5-8 is relatively difficult to implement and determining dependencies on parameters such as barrier height must be done numerically. At equilibrium the effective density of states and approximate Fermi function used in our analysis are excellent approximations [41] and allow us to obtain a simplified result which is easy to implement and displays the key physical dependencies.

A QW in a p-n junction device at equilibrium is depicted in Fig. 5-2. We have selected the location of the QW such that a point exists within the QW where the intrinsic Fermi level of the 3-D states crosses the Fermi level (i.e., $E_{i3D} = E_F$) as shown in Fig. 5-2. For the mathematical analysis carried out in this section we will work at the point where $E_{i3D} = E_F$ as it reduces the complexity of the mathematical derivation. The arbitrary selection of this point for the analysis in no way affects the result, which is equally valid for a QW at any point in the active region, but reduces the mathematical terms that must be carried through the analysis. Fig. 5-2 shows the

energy band diagram for the point in the active region at which $E_{i3D} = E_F$. The following relations are obtained graphically from Fig. 5-2,

$$E_{i2D} - E_F = \frac{E_{g3D}}{2} - \frac{E_{g2D}}{2} - E_{bc}, \qquad \text{Eq. 5-9}$$

$$E_{i2D} - E_F = -\left[\frac{E_{g3D}}{2} - \frac{E_{g2D}}{2} - E_{bv}\right]. \qquad \text{Eq. 5-10}$$

E_{g3D} is the energy gap between the 3-D, unconfined states in the conduction band and the valence band. E_{g2D} is the energy gap between the n = 1 energy level in the conduction band and the n = 1 energy level in the valence band. The 3-D unconfined states in the conduction band and valence band are separated by an energy gap E_{g3D} and the 2-D, n = 1 energy level states in the conduction and valence band are separated by an energy gap E_{g2D}. E_{bc} and E_{bv} are the separation in energy between the n = 1 energy level and the 3-D unconfined states for the conduction and valence bands respectively and are the barrier energies that electrons and holes at the band edge must overcome to escape the 2-D states of the QW. E_{i2D} is the intrinsic Fermi level for the 2-D confined states and E_{i3D} is the intrinsic Fermi level for the 3-D unconfined states. E_{i2D} and E_{i3D} are assumed to be in the middle of the E_{g2D} and E_{g3D} energy gaps respectively and the small offset due to the difference in density of states between the conduction band and valence band is ignored [41].

We are examining a device at equilibrium. At equilibrium the Fermi level will lie several kT below the conduction band edge and we may simplify our analysis by using the concept of the effective density of states. The effective density of states is defined as [41],

$$n = \int_{E_c}^{\infty} f(E)\rho(E)dE = N_c f(E_c), \qquad \text{Eq. 5-11}$$

where n is the carrier density in the conduction band, f(E) is the Fermi function, $\rho(E)$ is the density of states for the conduction band, and N_c is the effective density of states for the

conduction band. The effective densities of states for the confined 2-D states and 3-D unconfined states are derived in Appendix II. As we are at equilibrium $(E_c-E_F) >> kT$ so that the Fermi function f(E) can be approximated with [41],

$$f(E) \approx \exp\left[\frac{E_F - E}{kT}\right], \qquad \text{Eq. 5-12}$$

where k is Boltzmann's constant and T is the temperature.

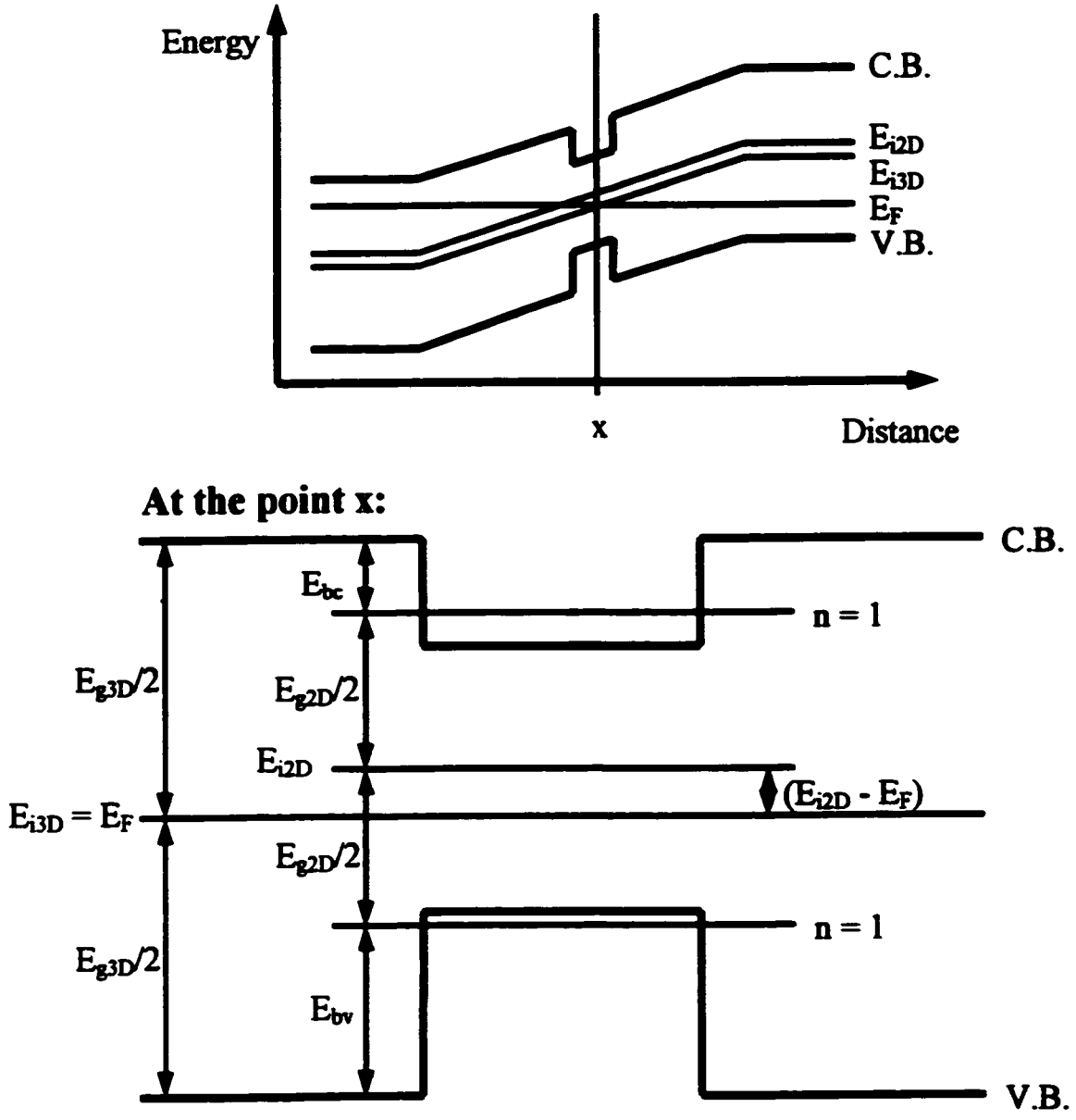

Fig. 5-2 Schematic defining the energy variables used in my analysis.

Now we employ some well known relations for the carrier concentrations in a semiconductor at equilibrium [41]. Using the selection of $E_{i3D} = E_F$ we can write the electron and hole carrier densities in the 3-D states at equilibrium [41],

$$n_{3D} = p_{3D} = n_{i3D} = \sqrt{N_{c3D}N_{v3D}}\exp\left[-\frac{E_{g3D}}{2kT}\right], \qquad \text{Eq. 5-13}$$

where n_{3D} is the electron density in the 3-D unconfined states of the conduction band, p_{3D} is the hole density in the 3-D unconfined states of the valence band, n_{i3D} is the intrinsic carrier density, and N_{c3D} and N_{v3D} are the effective densities of states for the 3-D unconfined states in the conduction band and valence band respectively and are derived in Appendix II. E_{g3D}, k, and T are defined above. For the 2-D confined states the intrinsic carrier density is given by [41],

$$n_{i2D} = \sqrt{N_{c2D}N_{v2D}}\exp\left[-\frac{E_{g2D}}{2kT}\right], \qquad \text{Eq. 5-14}$$

where n_{i2D} is the intrinsic carrier density, N_{c2D} and N_{v2D} are the effective densities of states for the n = 1, 2-D confined states of the conduction band and valence band respectively and are derived in Appendix II, E_{g2D}, k, and T are defined above. The electron and hole equilibrium carrier densities in the 2-D confined states are given by [41],

$$n_{2D} = n_{i2D}\exp\left[\frac{E_F - E_{i2D}}{kT}\right], \qquad \text{Eq. 5-15}$$

$$p_{2D} = n_{i2D}\exp\left[\frac{E_{i2D} - E_F}{kT}\right]. \qquad \text{Eq. 5-16}$$

Eq. 5-13, Eq. 5-15, and Eq. 5-16 give the conduction band and valence band carrier concentrations in the 2-D and 3-D states at equilibrium. Eq. 5-1 and Eq. 5-2 give us the rates into and out of the conduction band and valence band QWs. At equilibrium the carrier densities must remain at their equilibrium values and hence the rates into the QWs must equal the rates out of the QWs ($R_{cap} \equiv R_{esc}$). Equating the capture and escape rates (Eq. 5-1 and Eq. 5-2) and using the

populations at equilibrium (Eq. 5-13, Eq. 5-15, and Eq. 5-16) as well as Eq. 5-9 and Eq. 5-10, gives, for the conduction band QW,

$$\frac{AL_w\sqrt{N_{c3D}N_{v3D}}\exp\left[-\frac{E_{g3D}}{2kT}\right]}{\tau^c_{cap}} = \frac{AL_w\sqrt{N_{c2D}N_{v2D}}\exp\left[-\frac{E_{g2D}}{2kT}\right]\exp\left[-\frac{E_{g3D}-E_{g2D}-2E_{bc}}{2kT}\right]}{\tau^c_{esc}},$$

Eq. 5-17

which reduces to,

$$\tau^c_{esc} = \tau^c_{cap}\sqrt{\frac{N_{c2D}N_{v2D}}{N_{c3D}N_{v3D}}}\exp\left[\frac{E_{bc}}{kT}\right].$$ Eq. 5-18

Similarly, for the valence band QW,

$$\tau^v_{esc} = \tau^v_{cap}\sqrt{\frac{N_{c2D}N_{v2D}}{N_{c3D}N_{v3D}}}\exp\left[\frac{E_{bv}}{kT}\right].$$ Eq. 5-19

Eq. 5-18 and Eq. 5-19 give relationships between the capture and escape times for the conduction and valence band QWs which *must be true* for the equilibrium condition to be satisfied when the device is at equilibrium. The above relationships between the capture times and escape times for the conduction band and valence band QWs are valuable tools for the analysis of experimental and theoretical capture and escape times. For example, if an experiment measures the capture time of electrons into a QW one can estimate the escape time or if a theoretical method is developed for calculating the escape time from a QW then the capture time can be calculated.

Eq. 5-18 and Eq. 5-19 allow us to write the capture and escape rates for the conduction and valence band QWs in terms of the capture times. For the conduction band QW,

$$R^c_{cap} = \frac{AL_w n_{3D}}{\tau^c_{cap}},$$ Eq. 5-20

$$R^{c}_{esc} = \frac{AL_w n_{2D}}{\tau^{c}_{cap}} \sqrt{\frac{N_{c3D}N_{v3D}}{N_{c2D}N_{v2D}}} \exp\left[-\frac{E_{bc}}{kT}\right], \qquad \text{Eq. 5-21}$$

and for the valence band QW,

$$R^{v}_{cap} = \frac{AL_w p_{3D}}{\tau^{v}_{cap}}, \qquad \text{Eq. 5-22}$$

$$R^{v}_{esc} = \frac{AL_w p_{2D}}{\tau^{v}_{cap}} \sqrt{\frac{N_{c3D}N_{v3D}}{N_{c2D}N_{v2D}}} \exp\left[-\frac{E_{bv}}{kT}\right]. \qquad \text{Eq. 5-23}$$

5.3 Implications of the Equilibrium Condition

In the previous section we used the equilibrium condition to develop a relationship between the capture and escape times for a semiconductor QW. Eq. 5-18 and Eq. 5-19 are powerful because they allow one to determine the escape time if the capture time is known or the capture time if the escape time is known. In this section we examine the implications of Eq. 5-18 and Eq. 5-19.

Carrier capture times have been found experimentally for InGaAs/InP QWs to be ≈ 0.25 ps for holes and $\approx$ 1 ps for electrons [37]. For Table 5-1 we took the difference in band gap between the barrier and well material to be $E_{gb} - E_{gw} = 0.4$ eV. We also approximated the valence and conduction band QW barrier heights to be $E_{bv} = 0.6(E_{gb} - E_{gw})$ and $E_{bc} = 0.4(E_{gb} - E_{gw})$, ignoring the fact that the barrier height is decreased because the n = 1 energy level does not lie at the band edge of the QW. The escape times for electrons and holes calculated using Eq. 5-18 and Eq. 5-19 for capture times of 0.25 ps for holes and 1 ps for electrons are 100 to 1000 times the magnitude of the respective capture times. The predicted escape times are of the same order of magnitude as values typically found in the literature such as those predicted by thermionic emission theory which are also displayed in Table 5-1. Note also that the predicted escape times

have the same exponential dependence with barrier height ($\exp[E_b/kT]$) as escape times typically used in the literature [37].

In the previous paragraph we used Eq. 5-18 and Eq. 5-19 to determine escape times from experimentally determined values for the carrier capture time. Eq. 5-18 and Eq. 5-19 are also useful in theoretical modeling because a theoretically determined carrier capture time will also provide, through Eq. 5-18 and Eq. 5-19, a theoretical carrier escape time and vice versa. Classical thermionic emission theory has been used to determine a theoretical carrier escape time from a QW [53]. Using Eq. 5-18 and Eq. 5-19 a theoretical capture time can be determined from the theoretical thermionic emission escape time. Classical thermionic emission theory was first applied to QWs by Schneider and Klitzing [53]. They determined the thermionic emission current out of the well over the QW barriers to the left and to the right and then used the equivalent of Eq. 5-2 to determine a thermionic emission escape time to the left and to the right. Schneider and Klitzing found [53],

$$\tau_{esc}^{r,l} = L_w\left[\frac{2\pi m^*}{kT}\right]^{1/2}\exp\left[\frac{E_{r,l}}{kT}\right], \qquad \text{Eq. 5-24}$$

where m^* is the effective mass, $E_{r,l}$ is the barrier height to the left or right of the QW, and L_w, k and T are as defined in the previous section. If nearly equal barrier heights to the left and right are assumed then the results of Schneider and Klitzing can be rewritten using the same variables as the analysis we presented in the previous section. The escape time and escape rate for the valence band QW derived from thermionic emission theory are,

$$\tau_{esc}^{thermionic} = \frac{L_w}{2}\left[\frac{2\pi m_v}{kT}\right]^{1/2}\exp\left[\frac{E_{bv}}{kT}\right], \qquad \text{Eq. 5-25}$$

$$R_{esc}^{thermionic} = 2Ap_{2D}\left[\frac{kT}{2\pi m_v}\right]^{1/2}\exp\left[-\frac{E_{bv}}{kT}\right]. \qquad \text{Eq. 5-26}$$

Eq. 5-19 can be used to determine a carrier capture time that satisfies the equilibrium condition for the escape time predicted by thermionic emission theory. The capture time and capture rate required to satisfy equilibrium using thermionic emission theory are, for the valence band QW,

$$\tau_{cap}^{thermionic} = \frac{L_w}{2}\left[\frac{2\pi m_v}{kT}\right]^{1/2}\sqrt{\frac{N_{c3D}N_{v3D}}{N_{c2D}N_{v2D}}}, \qquad \text{Eq. 5-27}$$

$$R_{cap}^{thermionic} = 2Ap_{3D}\left[\frac{kT}{2\pi m_v}\right]^{1/2}\sqrt{\frac{N_{c2D}N_{v2D}}{N_{c3D}N_{v3D}}}. \qquad \text{Eq. 5-28}$$

Calculated capture and escape times for the conduction and valence band QWs predicted by thermionic emission theory in conjunction with the equilibrium condition are displayed in Table 5-1. The predicted capture time for holes agrees at least in order of magnitude with experimentally measured values for the hole capture time [37]. The predicted capture time for electrons is much shorter than experimentally determined values for the electron carrier capture time [37]. Thermionic emission theory does not appear to account properly for the difference in carrier capture between electrons and holes.

		150 Å	100 Å	50 Å	25 Å
Experimental τ_{cap}	τ^{v}_{cap}	0.25 ps	0.25 ps	0.25 ps	0.25 ps
	τ^{v}_{esc}	0.62 ns	0.93 ns	1.9 ns	3.7 ns
Experimental τ_{cap}	τ^{c}_{cap}	1.0 ps	1.0 ps	1.0 ps	1.0 ps
	τ^{c}_{esc}	0.11 ns	0.17 ns	0.34 ns	0.68 ns
Thermionic Emission	τ^{v}_{cap}	0.72 ps	0.32 ps	0.079 ps	0.02 ps
	τ^{v}_{esc}	1.78 ns	1.19 ns	0.59 ns	0.30 ns
Thermionic Emission	τ^{c}_{cap}	0.27 ps	0.12 ps	0.03 ps	7.4 fs
	τ^{c}_{esc}	31 ps	20 ps	10 ps	5.0 ps

Table 5-1 Experimentally measured carrier capture times [37] and corresponding escape times calculated using Eq. 5-18 and Eq. 5-19 as well as carrier capture and escape times predicted using thermionic emission theory in conjunction with Eq. 5-18 and Eq. 5-19.

The carrier capture and escape times predicted using thermionic emission theory have very different dependencies on QW thickness from those obtained by using experimentally determined carrier capture times and calculating the carrier escape times using Eq. 5-18 and Eq. 5-19. If one uses the experimentally determined values for the carrier capture time then the carrier capture rate, given by Eq. 5-20 for electrons and Eq. 5-22 for holes, is proportional to the QW thickness, L_w, so that thinner QWs are pumped at a slower rate than thicker QWs. The capture rate predicted using thermionic emission theory is proportional to $\sqrt{\frac{N_{c2D}N_{v2D}}{N_{c3D}N_{v3D}}}$ which is proportional to $1/L_w$. The thermionic emission model predicts that thinner QWs are pumped at a faster rate than thicker QWs. To fit experimental data taken from AMQW lasers with QWs of different thicknesses within the same active region it is necessary to have the correct dependencies with QW thickness. Eq. 5-22 and Eq. 5-23 were used in the model described in Chapter 4 to fit experimental data taken from 13 different AMQW lasers structures. The gain spectrum at threshold for structure 1 lasers with cavity lengths of 550 μm predicted using the carrier capture and escape rates given by Eq. 5-22 and Eq. 5-23 is plotted in Fig. 5-3. The gain spectrum for the same device with the same applied bias predicted using the carrier capture and escape rates predicted by thermionic emission theory (Eq. 5-26 and Eq. 5-28) is also plotted in Fig. 5-3. Eq. 5-22 and Eq. 5-23 predict nearly equal contributions from the 100 Å and 50 Å QWs with no contribution from the 35 Å QWs as was observed experimentally. Thermionic emission theory predicts that the gain spectrum will be dominated by the 35 Å QWs. The capture rate determined using thermionic emission theory predicts that thin QWs are pumped more strongly than was observed experimentally. It was not possible to fit our experimental data taken from AMQW structures using the carrier capture and escape rates predicted by thermionic emission theory.

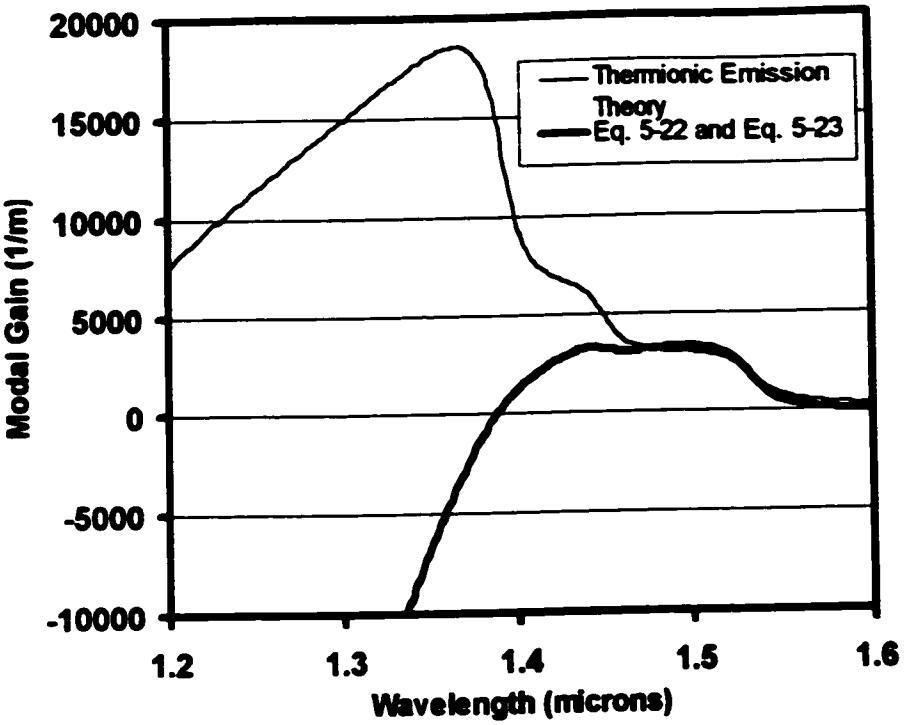

Fig. 5-3 Theoretical plot of the gain spectra at threshold for a 600 μm cavity length structure 1 device using the model described in chapter 4 with experimentally measured carrier capture times and escape times predicted using Eq. 5-18 and Eq. 5-19. The gain spectra predicted using the capture and escape times predicted using thermionic emission theory for the same structure, cavity length, and applied bias is plotted for comparison.

5.4 Conclusion

The theoretical approach used to treat the processes of carrier capture and escape from a QW in the model presented in Chapter 4 have been described. We use a non-equilibrium model, meaning we do not require the carrier densities in the 2-D and 3-D states of the QWs to be in equilibrium while the device is under bias. Our model does however require that the equilibrium condition be satisfied when the device is not under bias and at equilibrium. This requirement is not satisfied by most models in the literature meaning that these models predict net current flow into or out of the QWs when the device is not under bias - an unphysical situation. I have

developed analytic relations between the carrier capture and escape rates which are easy to implement in a theoretical model.

6. CHAPTER 6 – BROADLY TUNABLE AMQW LASERS

6.1 Introduction

AMQW lasers were introduced in chapter 1 and some reasons for studying them were mentioned. AMQW lasers are useful for studying the physics taking place in the active region of lasers as they can be used to probe the active region as a function of distance and to study dependencies on parameters such as QW thickness. The majority of this thesis has been devoted to the implementation of an experimental technique which employs AMQW lasers to study the physics taking place in the active region of MQW lasers. AMQW lasers are also of interest because they may be suitable to a large number of applications. In this chapter we discuss one such application: broadly tunable lasers.

In chapter 1 I defined AMQW devices with QWs of varying thickness as *dimensionally asymmetric* MQW devices and AMQW devices with QWs of varying composition as *compositionally asymmetric* MQW devices. The QWs of different thickness and/or composition generally emit at different wavelengths which makes AMQW devices suitable for applications such as spectrally broad SLDs and broadly tunable lasers. Dimensionally AMQW lasers in external cavity configurations have been shown experimentally and theoretically to exhibit broad wavelength tuning ranges [13,15,17,24].

AMQW lasers can, if designed properly, exhibit broad spectral tuning ranges more than twice as large as conventional MQW lasers. In this chapter it is shown experimentally and theoretically that AMQW lasers only exhibit broad wavelength tuning ranges near the transition cavity length. The transition cavity length is a critical design parameter for engineering broadly tunable AMQW lasers.

6.2 Broadly Tunable AMQW Lasers

Our original interest in AMQW lasers was to create a broadly tunable laser source for the purpose of trace liquid detection [56]. Structure 13 shown in Fig. 6-1 was the first AMQW laser structure grown at McMaster University and was designed by Xiang Zhu to detect liquids near 1.4 μm. Structure 13 is described in detail in [17]. Dr. Zhu obtained a 118 nm tuning range using a Littrow configuration external cavity to tune a 250 μm cavity length uncoated structure 13 device [17]. Dr. Zhu was also able to tune a 500 μm cavity length structure 13 device over an 80 nm tuning range [17].

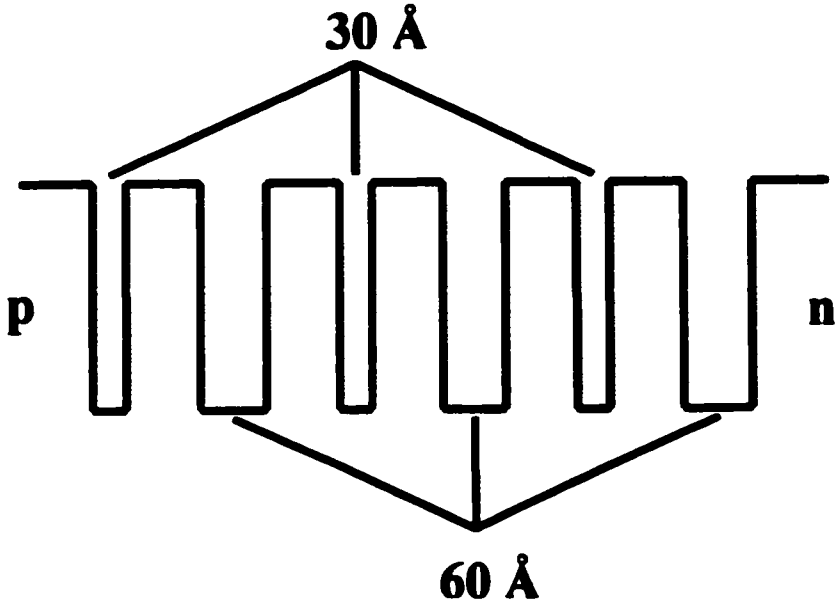

Fig. 6-1 Schematic of the active region of structure 13.

Gingrich *et al.* [13] reported an InGaAs/AlGaAs AMQW laser with three quantum wells having thicknesses of 80 Å, 60 Å and 45 Å in a Littrow configuration external cavity. A 155 μm cavity length device with one AR coated facet and one angled facet was tuned over an 80 nm wavelength range and a 287 μm cavity length device with an AR coated facet was tuned over a somewhat smaller range (≈ 66 nm). Krauss *et al.* [15] were able to wavelength tune a 600 μm

cavity length AR coated GaAs/AlGaAs AMQW laser with one 100 Å, two 50 Å and four 25 Å quantum wells over an 85 nm range using a grating external cavity. Lee *et al.* [18] reported a tilted stripe AMQW laser amplifier consisting of two InGaAs quantum wells 40 Å and 75 Å thick which was wavelength tuned using a grating coupled ring external cavity. They obtained tuning ranges of 90, 70, and 48 nm for 400, 700, and 1000 μm cavity lengths respectively.

6.3 Cavity Length Dependence

Prior to the investigation of AMQW devices as broadly tunable lasers researchers produced broadly tunable lasers by accessing contributions to the gain spectrum from the n = 1 and n = 2 transitions in the same QW [57,58]. For convenience we will dub broadly tunable lasers which rely on n = 1 and n = 2 transitions in the same QW as *dual quantized state* (DQS) devices. Mehuys *et al.* [57] described the design criteria for broadly tunable DQS lasers. To achieve broad tuning ranges the cavity length/loss must be adjusted to attain nearly equal contributions to the gain peak from the n = 1 and n = 2 transitions [57]. If the cavity length is too long the n = 1 transition dominates and the n = 2 transition does not contribute significantly. For long cavity lengths, wavelength tuning ranges are those typically reported for standard QW lasers and are on the order of 45 nm for uncoated devices tuned using grating external cavities [59]. Mehuys *et al.* [57] found that if the cavity length is too short the n = 2 transition dominates the gain curve and the tuning range is limited to near the n = 2 peak (a roughly 20 nm range). But when the cavity length was optimised to obtain nearly equal contributions from the n = 1 and n = 2 transitions Mehuys *et al.* [57] achieved a 105 nm tuning range which is approximately double the tuning range that has been reported for uncoated devices operating on the n = 1 transition alone. Using an optimised AR coated DQS laser Tabuchi and Ishikawa [58] achieved a 240 nm tuning range.

Other authors have claimed without proof or argument that the optimisation of cavity length/loss required to achieve a broad tuning range in DQS lasers is not required for AMQW lasers [15,18]. Krauss, Hondromitros, Vögele and De La Rue [15] stated that AMQW lasers "should be very much less dependent on the choice of cavity length" than DQS lasers but only tested their devices at a single cavity length. Lee and Lin [18] reported three substantially different tuning ranges for the same AMQW structure with three different cavity lengths and stated that unlike DQS lasers "no particular device length is required". In this chapter we demonstrate experimentally and theoretically that optimisation of cavity length/loss is required to achieve a broad wavelength tuning range with AMQW lasers.

The behaviour of AMQW lasers with varying cavity length/loss is strikingly similar to DQS lasers. The gain peak is broad and flat near a specific cavity length/loss but is narrow and sharply peaked for other cavity lengths/losses. In this chapter we show experimentally, using the same technique as Mehuys *et al.* [57], that the breadth of the tuning range is strongly dependent on cavity length. This dependence with cavity length is explained physically using a previously developed gain model for AMQW lasers [30].

We have previously reported a phenomenon called the transition cavity length in AMQW lasers [21,22,25,30]. AMQW lasers with two different thickness wells in the active region initially reach threshold on the thick wells in the active region for long cavity lengths and initially reach threshold on the thin wells for short cavity lengths. This behaviour has been experimentally observed in thirteen different AMQW laser structures [30] and therefore is thought to be a general property of AMQW lasers. We have defined the *transition cavity length* (TCL) to be the cavity length above which AMQW lasers initially reach threshold on the thick wells and below which

they initially reach threshold on the thin wells [21]. The TCL marks the onset of lasing on the thin wells which is analogous to what Mehuys *et al.* [57] described as the "onset of second quantised state lasing" for DQS lasers.

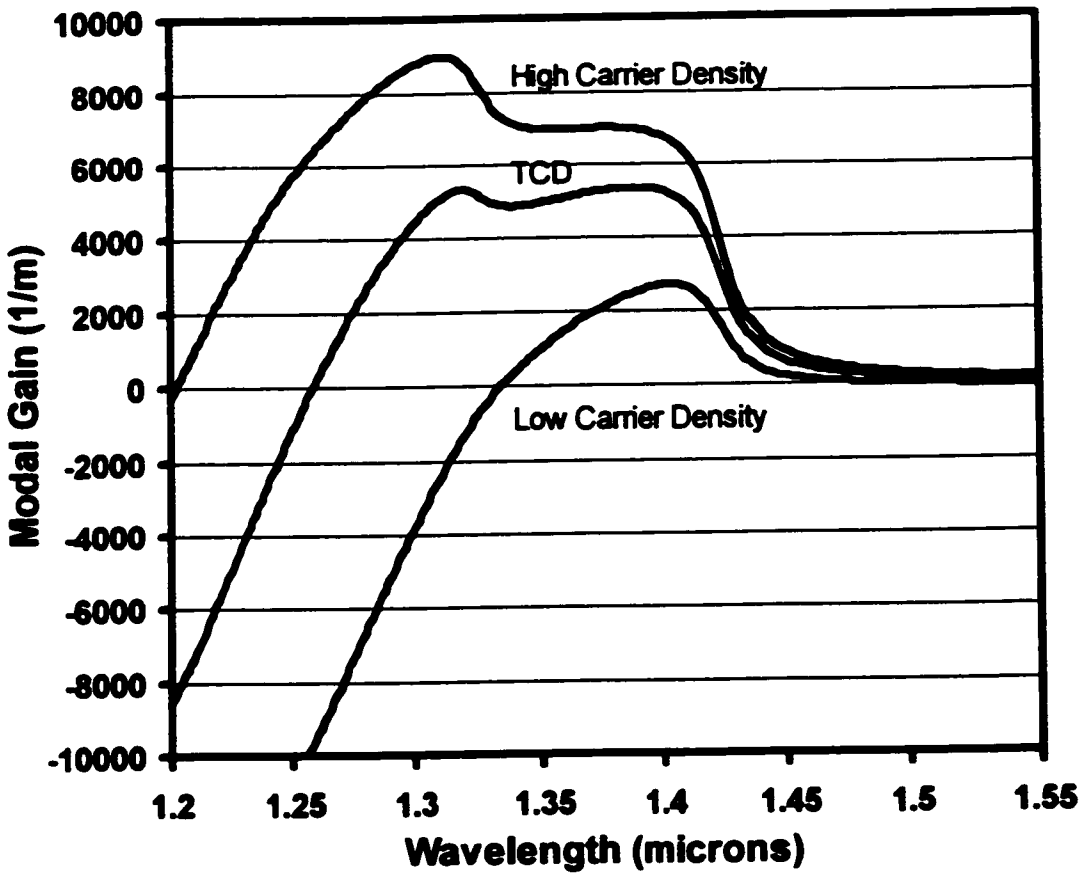

Fig. 6-2 Theoretical Gain curves for structure 13 assuming a uniform carrier distribution amongst all the QWs. Gain curves for three different carrier densities are shown.

In chapter 4 we developed a gain model for AMQW lasers and used it to explain the physical origin of the TCL in AMQW lasers. Calculated modal gain curves for structure 13 (see Fig. 6-1) are shown in Fig. 6-2 for three different carrier densities. For illustration, a uniform carrier distribution (equal carrier densities in all the QWs) is assumed for Fig. 6-2. As explained in chapter 4, the result of the Bernard-Durafourg condition is that the thick wells (low energy transition) reach transparency at lower carrier densities than the thin wells (high energy

transition). Fig. 6-2 demonstrates that for low carrier densities the gain peak is entirely due to the thick wells as the thin wells have not yet reached transparency. As the carrier density increases the thin wells reach transparency and contribute to the gain peak. At a particular carrier density the gain peaks of the thick and thin wells are equal and the total gain curve is broad and flat. We define this carrier density to be the *transition carrier density* (TCD). At higher carrier densities the gain peak of the thin wells is higher than that of the thick wells and the gain drops off sharply on both sides of the gain peak of the thin wells. Fig. 6-2 demonstrates that the gain spectrum is only broad and flat near the transition carrier density.

The peak gain at threshold and hence the carrier density at threshold are determined by the cavity loss and the cavity length according to the laser threshold condition,

$$R_1 R_2 e^{2(g_{th}-\alpha)L_{cav}} = 1 \qquad \text{Eq. 6-1}$$

where g_{th} is the peak gain at threshold, R_1 and R_2 are the power reflectances of the facets, α is the loss per unit length, and L_{cav} is the cavity length. If the facet reflectances and α remain constant then the peak gain at threshold and the threshold carrier density are determined by the cavity length. Devices with long cavity lengths have more gain material available to overcome the mirror losses than devices with short cavity lengths. Thus, for longer cavity lengths g_{th} is smaller and the threshold carrier density is smaller than for shorter cavity lengths. The TCL is the cavity length at which the threshold carrier density is the transition carrier density. The gain peak is only broad and flat near the TCL.

The experimental method described by Mehuys *et al.* [57] was used to study the tuning range of structures 1 and 13 at various cavity lengths. The uncoated Fabry-Perot lasers were mounted active region up on a copper heat sink and the temperature was stabilized using a thermoelectric cooler. All the devices were operated under cw conditions and all work was done

at 23 °C. The wavelength was tuned using an external cavity which consisted of a 600 line/mm ruled grating (blaze angle of 22.01 ° at 1.25 μm, E43746, Edmund Scientific) and a molded aspheric lens (350110-C, THORLABS, N.A. = 0.40) in the Littrow configuration.

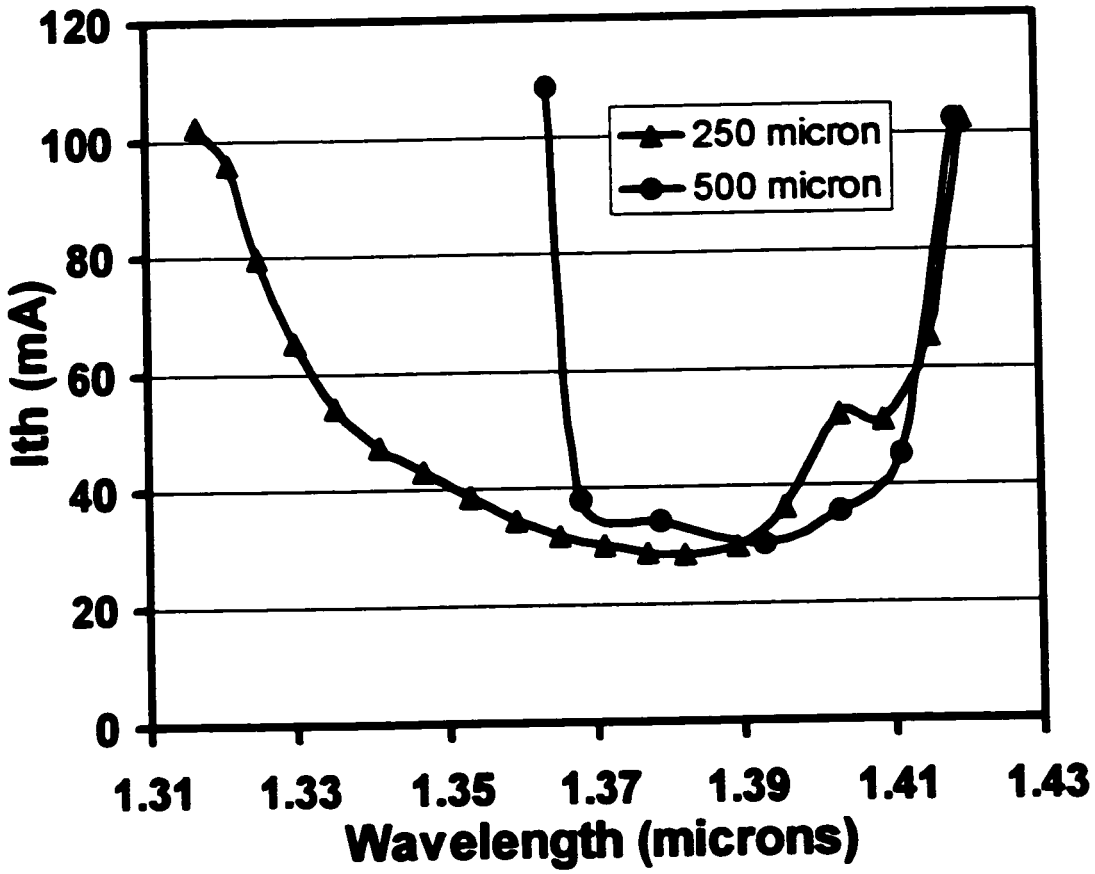

Fig. 6-3 Measured single longitudinal mode threshold current versus wavelength for structure 13 devices cleaved to cavity lengths of 500 μm and 250 μm.

Fig. 6-3 shows the measured threshold current versus grating-selected wavelength across the tuning range for structure 13 devices cleaved to 500 μm and 250 μm cavity lengths. The 250 μm cavity length device was tuned over a 103 nm tuning range from 1.317 μm to 1.420 μm and the 500 μm cavity length device was tuned over a 55 nm tuning range from 1.364 μm to 1.419 μm. The tuning range is substantially larger for the 250 μm device than for the 500 μm device. A

conventional MQW laser operating near 1.4 μm with five QWs all of the same thickness was tuned over a 45 nm wavelength range using the same external cavity [59].

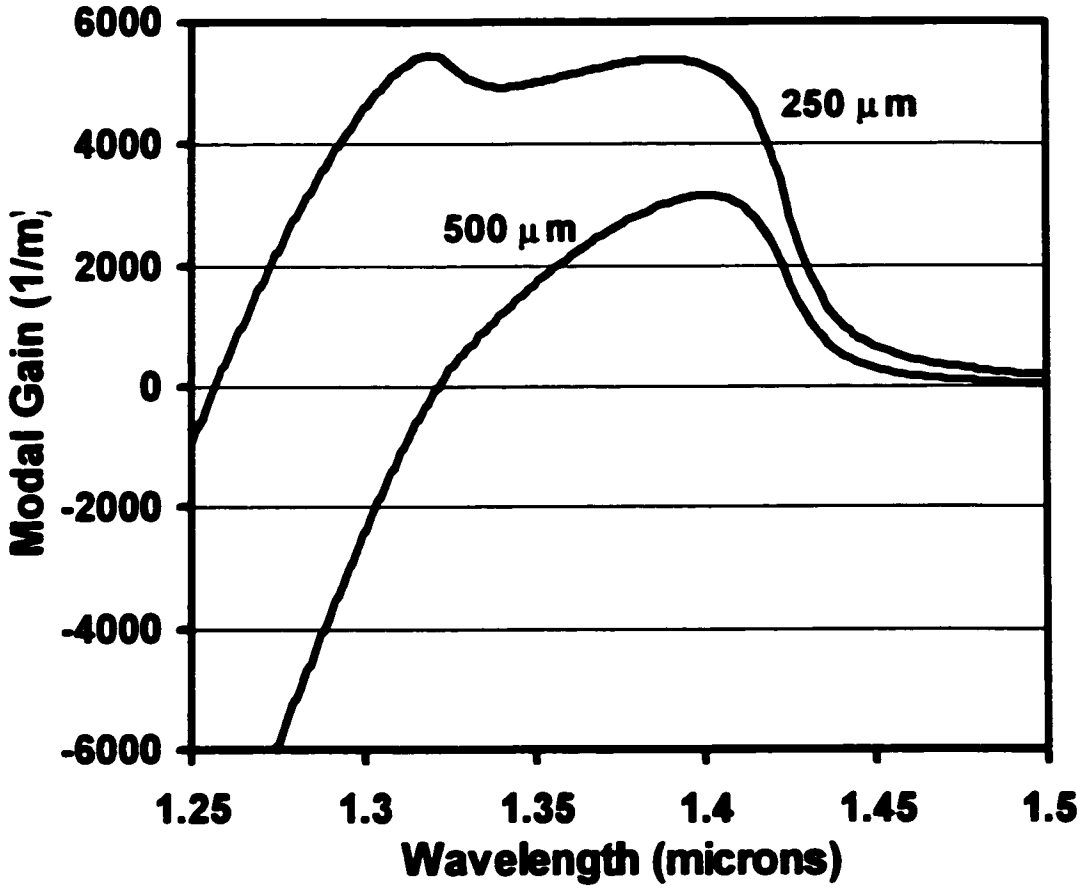

Fig. 6-4 Calculated gain curves at threshold for structure 13 devices with 500 μm and 250 μm cavity lengths.

Fig. 6-4 shows calculated gain curves at laser threshold for structure 13 devices with cavity lengths of 500 μm and 250 μm. For these calculations the carrier densities in the wells were not assumed to be equal but were calculated according to the model described in chapter 4 to account for the non-uniform carrier distribution. Our model predicted the TCL for structure 13 to be approximately 250 μm. The TCL for structure 13 was determined experimentally to be 300 ± 100 μm by plotting lasing wavelength at threshold versus cavity length as shown in Fig.

6-5. At 250 μm the gain curve is broad and flat owing to nearly equal gain peaks from the thick and thin wells which results in a broad tuning range more than double that of a conventional laser. At 500 μm, which is far above the TCL, the thin wells do not contribute significantly to the gain curve and the tuning range is extended only ≈10 nm beyond that of a conventional laser. Fig. 6-3 and Fig. 6-4 demonstrate that the tuning ranges of AMQW lasers with cavity lengths far from the TCL are roughly equal to those obtained using a conventional MQW laser with all the wells of the same thickness. Only near the TCL where equal contributions to the gain curve are seen from the different thickness wells does one see a substantially broadened wavelength tuning range. Thus, the cavity length is of critical importance when designing and implementing broadly tunable AMQW lasers.

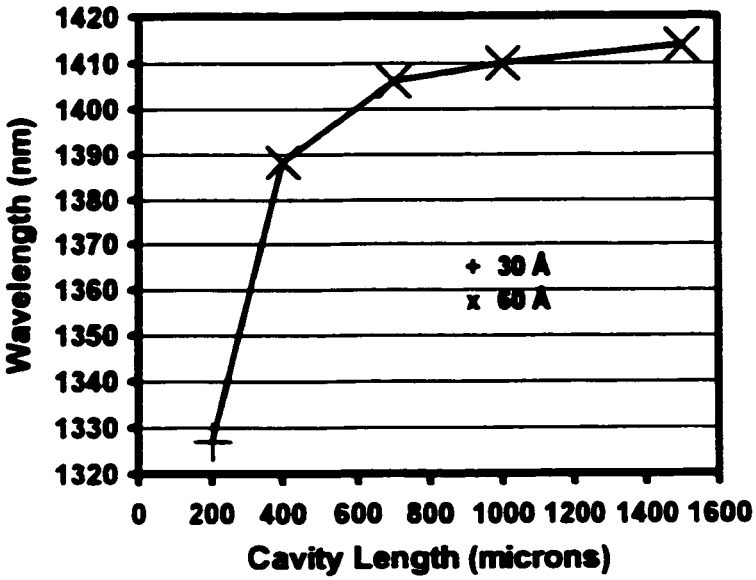

Fig. 6-5 Experimentally measured wavelength at threshold versus cavity length for structure 13.

As stated earlier the calculated gain curves only account for the n = 1 conduction band to heavy hole band transitions in the QWs. The conduction band to light hole band transitions are ignored because all of the devices discussed in this paper are compressively strained. It is possible

that the extended tuning range for the 250 μm cavity length device shown in Fig. 6-3 is due to contributions from the n = 1 and n = 2 transitions in the 60 Å wells and not the n = 1 transitions in the 60 Å and 30 Å wells. This possibility can be ruled out by examining the transition wavelengths for the n = 1 and n = 2 transitions in the wells. For structure 13 the n = 2 energy level is not confined in the conduction band of the 60 Å QWs which eliminates the possibility that the extended tuning range observed in Fig. 6-3 is due to contributions from the n = 2 transition in the 60 Å QWs. For structure 1 the n = 2 transition in the 100 Å QWs is more than 25 nm shorter in wavelength than the n = 1 transition in the 35 Å QWs and hence the n = 1 and n = 2 transitions are easily distinguished. Wavelengths corresponding to the n = 2 transitions have not been observed in any of the AMQW devices we have studied.

6.4 Behaviour in an External Cavity

For DQS lasers, Mehuys *et al.* [57] recommended that the cavity length be slightly shorter than the cavity length at which lasing began on the n = 2 transition which is analogous to cavity lengths slightly shorter than the TCL for AMQW lasers. They found that for cavity lengths slightly longer than the cavity length at which lasing began on the n = 2 transition it was not possible to attain single mode operation across the entire tuning range. We have also found experimentally that for AMQW lasers with cavity lengths slightly longer than the TCL it is not possible to achieve single mode operation over the entire tuning range. To achieve single mode tuning over the entire broad flat gain peak it appears to be optimal to cleave devices to cavity lengths slightly shorter than the TCL.

A 600 μm cavity length structure 1 laser was tested in an external cavity to demonstrate the behaviour of devices with cavity lengths marginally longer than the TCL in external cavities.

At 70 mA a single mode (i.e., side mode suppression ratio greater than 20 dB) tuning range of 45 nm from 1.558 μm to 1.513 μm was attained. Lasing at the gain peak was suppressed over this entire tuning range. This is consistent with conventional MQW lasers tested using the same external cavity [59]. At 70 mA only the 100 Å well is contributing to the gain and so the tuning range is what one would expect for a conventional MQW laser where all the quantum wells are of the same thickness. At 130 mA laser operation was attained over a nearly 100 nm range from 1.560 μm to 1.461 μm, however a side mode suppression ratio greater than 100 was not obtained over the entire range because lasing at the gain peaks could not be suppressed as is described below. At 130 mA the 600 μm cavity length lasers have gain from both the 100 Å and 50 Å wells resulting in operation over a wavelength range that is roughly double that of a conventional MQW laser in which all the quantum wells are the same thickness.

At 70 mA the external cavity laser operated single mode at the selected wavelength and lasing at the gain peak of the 100 Å wells was suppressed. At 120 mA the external cavity laser operated single mode with the gain peak lasing suppressed while it was being tuned across wavelengths corresponding to the 100 Å wells. However, when the external cavity was used to select wavelengths at or shorter than the wavelength of the 50 Å wells (≈ 1.48 μm), the lasing at the gain peak of the 100 Å wells could not be suppressed. For a solitary laser (i.e., no external cavity) at 150 mA, the 50 Å wells have reached threshold and lase simultaneously with the 100 Å wells. With the external cavity and a current of 150 mA, while the external cavity was being tuned across the wavelength range associated with the 100 Å wells, lasing at the gain peak of the 100 Å wells was suppressed; however, lasing on the gain peak of the 50 Å wells could not be suppressed. Conversely, when the selected wavelength was set to a wavelength associated with

the 50 Å wells, lasing on the gain peak of the 50 Å wells was suppressed but lasing at the gain peak of the 100 Å wells continued.

6.5 Contributions From More Than Two Transition Energies

Wavelength tuning ranges of more than 100 nm have been demonstrated for uncoated dimensionally AMQW lasers with QWs of two different thicknesses which is more than double the tuning ranges achieved with conventional uncoated MQW lasers. There are several possible ways to extend the tuning range. One way to extend the tuning range is to put wells of more than two different thicknesses in the structure and attempt to get contributions to the gain curve from more than two transition energies. The TCL plays a critical role in attaining contributions to the wavelength tuning range from several different transitions in the same laser.

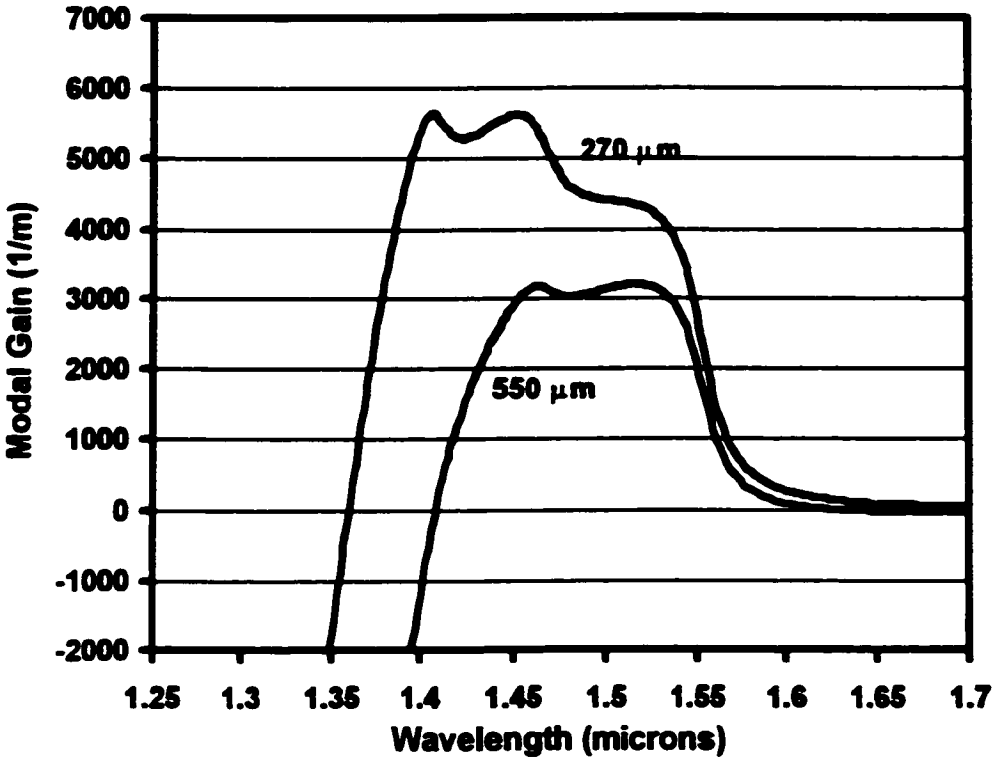

Fig. 6-6 Calculated gain curves at threshold for structure 1 devices with 550 μm and 270 μm cavity lengths.

Structure 1 (see Fig. 2-2) has wells of three different thicknesses. The calculated gain curves at threshold for structure 1 are shown in Fig. 6-6 for cavity lengths of 550 μm and 270 μm. From Fig. 6-6 we see that structure 1 has two transition cavity lengths. 550 μm is the TCL for the 100 Å and 50 Å wells. For cavity lengths longer than 550 μm structure 1 lasers initially reach threshold on the 100 Å wells and for cavity lengths shorter than 550 μm they initially reach threshold on the 50 Å wells. 270 μm is the TCL for the 50 Å and 35 Å wells. For cavity lengths longer than 270 μm and shorter than 550 μm structure 1 lasers initially reach threshold on the 50 Å wells and for cavity lengths shorter than 270 μm they initially reach threshold on the 35 Å wells. In general, AMQW structures with N different transition energies will have N - 1 transition cavity lengths. The wavelength tuning range was measured for a cavity length of 600 μm and was found to extend from 1.461 μm to 1.560 μm; a span of nearly 100 nm. The tuning range indicates contributions from the 100 Å wells and 50 Å wells but no contribution from the 35 Å wells. Near 550 μm the gain corresponding to the 35 Å wells is too weak to contribute to the tuning range and near 270 μm the gain peak corresponding to the 100 Å wells is too weak to contribute to the tuning range. It does not appear to be possible to tune over all three gain peaks of structure 1 with a single cavity length uncoated laser.

To obtain contributions to the tuning range from N different transition energies, all N - 1 TCLs must be approximately equal. If all N - 1 TCLs are approximately equal then for cavity lengths near the TCLs the gain curve at threshold will have N nearly equal peaks and the device should be wavelength tunable over all N peaks. It is possible to design AMQW lasers with multiple transition energies such that all the TCLs are equal. QW thickness, strain, the number of QWs of each transition energy [22] and the position of QWs in the active region [21,22,25] all

affect the TCL and can be used to engineer a structure with N transition energies to have N - 1 nearly equal TCLs. As an example we have re-engineered structure 1 by altering the thicknesses, numbers, and locations of the QWs in the active region to produce structure A shown in Fig. 6-7 (hypothetical structures will be denoted by letters; numbers are reserved for structures that were grown and tested). The theoretical gain curve at threshold for structure A at a cavity length of 600 μm is shown in Fig. 6-8. The hypothetical structure A should be tunable over all three gain peaks at a cavity length near 600 μm.

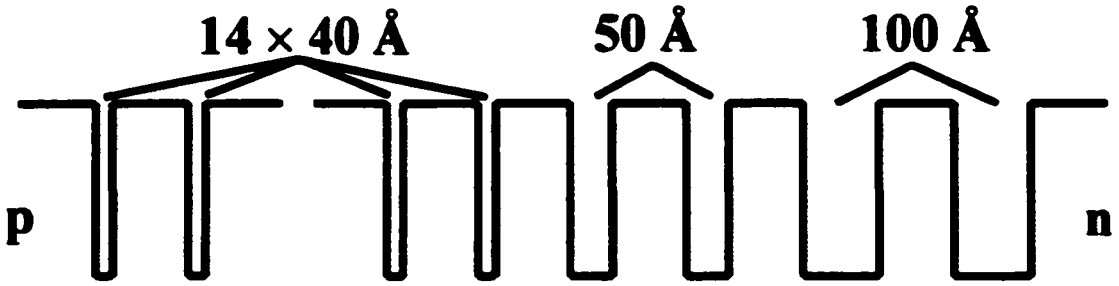

Fig. 6-7 Schematic of the hypothetical structure A.

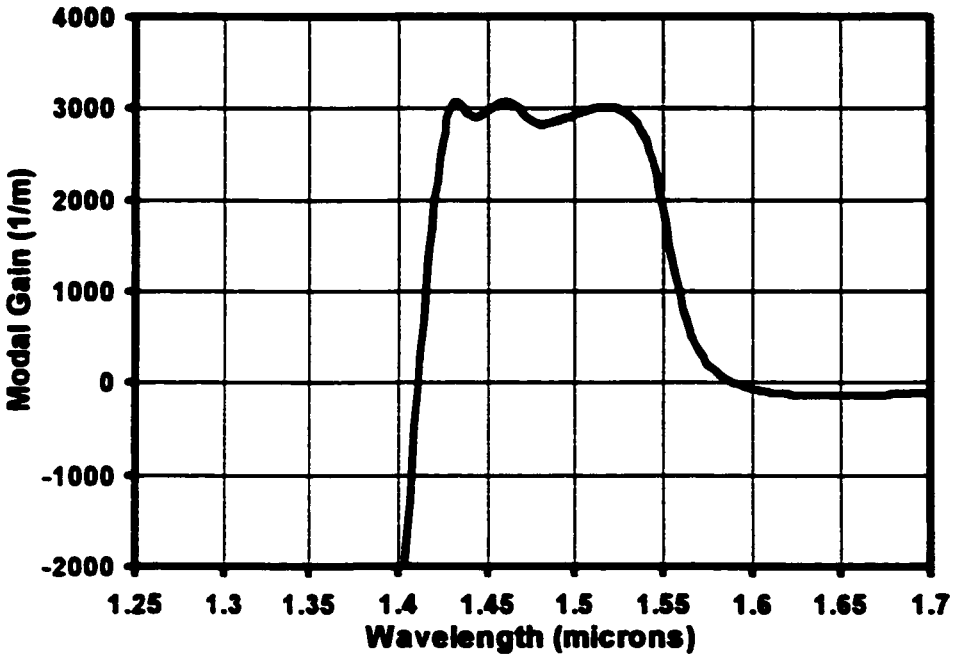

Fig. 6-8 Calculated gain curve at threshold for a 600 μm cavity length hypothetical device with fourteen 40 Å QWs, two 50 Å QWs, and two 100 Å QWs.

6.6 Compositionally AMQW Lasers

In the previous section we discussed the importance of making the N - 1 TCLs approximately equal in order to attain contributions to the tuning range from N different energy transitions. The gain curve of structure A shown in Fig. 6-8 demonstrates that it is possible to attain contributions to the tuning range from wells of three different thicknesses at a single cavity length. However, fourteen 40 Å wells were required to make the two TCLs equal in structure A. The dependence of the quasi-Fermi levels on well width results in thin wells producing less gain than thick wells for the same carrier density (see Eq. 4-5 and Eq. 4-6 of chapter 4). Fig. 6-9 shows plots of peak modal gain versus carrier density for single QWs of different thicknesses. Fig. 6-9 demonstrates how the peak modal gain of a well at a given carrier density decreases with decreasing well thickness. Thus, in order to obtain nearly equal gain peaks from wells of several different thicknesses at a single cavity length a large number of thin wells are required.

The maximum achievable tuning range for dimensionally AMQW lasers with reasonable numbers of QWs is limited by the smaller gain of thin wells. Obtaining nearly equal TCLs for the different transition energies of dimensionally AMQW structures with wells of several different thicknesses will require large numbers of the thinner wells. The large numbers of wells required makes these structures difficult to grow, especially when strain compensation is an issue. This limitation can be surpassed by using compositionally AMQW structures. Instead of changing the thickness of the wells to obtain different wavelengths the thickness can be kept constant and the composition of each well changed. Because the wells are the same thickness the well thickness dependence of the quasi-Fermi levels is not a factor and the wells contribute nearly equal amounts of gain but at different wavelengths. It is then feasible to design devices with gain curves that have nearly equal peaks corresponding to many different transition energies at the same cavity

length without using large numbers of QWs. Fig. 6-10 shows the calculated gain curve for structure B, one possible compositionally AMQW laser design. Structure B is a hypothetical device which contains ten 100 Å QWs of varying composition separated by 50 Å barriers of composition $In_{.80}Ga_{.20}As_{.31}P_{.69}$. The x composition ($In_{1-x}Ga_xAs_yP_{1-y}$) is 0.20 in all the wells. The y composition of the wells varies from p-side to n-side as follows; 0.81, 0.8, 0.72, 0.68, 0.65, 0.64, 0.62, 0.6, 0.6, 0.58. Structure B exhibits a gain curve more than 300 nm across and demonstrates theoretically that compositionally AMQW structures have a great deal more potential as broadly tunable lasers than dimensionally AMQW lasers.

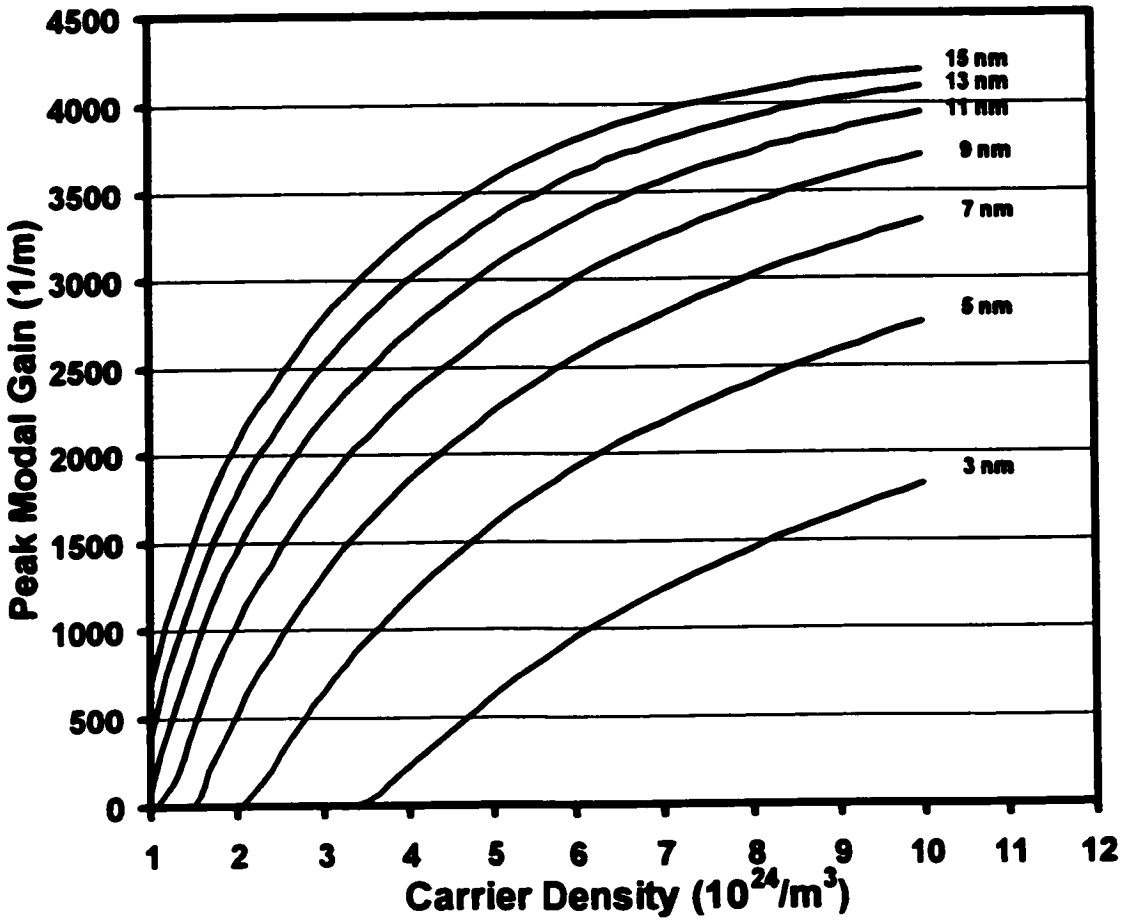

Fig. 6-9 Peak modal gain versus carrier density for different quantum well thicknesses. Thin wells provide less gain than thick wells at the same carrier density and have higher transparency carrier densities than thick wells.

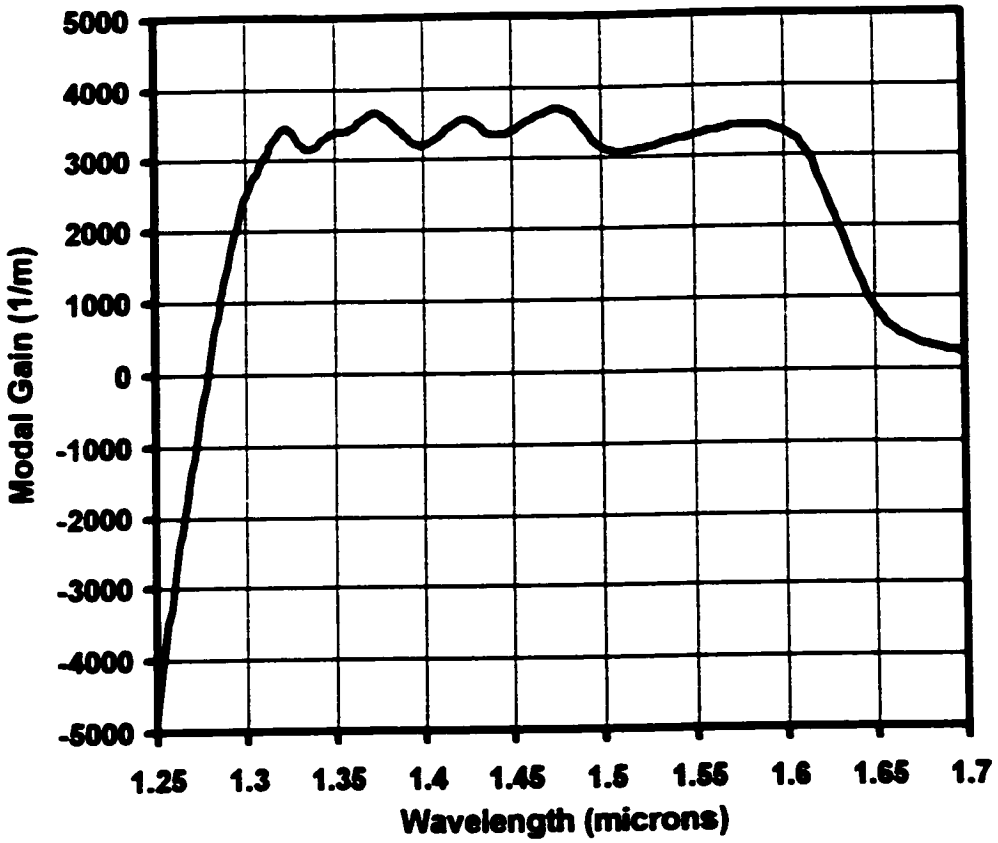

Fig. 6-10 Calculated gain curve at threshold for a 600 μm cavity length theoretical device with ten 100 Å QWs of varying composition and band gap.

6.7 Conclusion

AMQW lasers have been shown experimentally to exhibit tuning ranges more than double those obtained using conventional MQW lasers. We have experimentally demonstrated the importance of the cavity length/loss in designing broadly tunable AMQW lasers and explained this effect theoretically. The design issues for AMQW lasers are similar to those of broadly tunable lasers based on n = 1 and n = 2 transitions in the same QW. For a laser with two different transition energies there exists a transition cavity length at which both transitions contribute nearly equal amounts of gain resulting in a broad tuning range. Far from this TCL the tuning range is roughly equal to that of a conventional laser. To attain contributions to the tuning range from

more than two transition energies, the TCLs separating each transition energy must be designed to be approximately equal. The TCLs can be engineered to be approximately equal by varying the number of QWs, strain, position in the active region, and well thickness. Thin wells provide less gain in general than thick wells and as a result compositionally AMQW lasers (where the composition rather than the dimension is varied from well to well to change the emission wavelength) may be better suited to broadly tunable laser applications than dimensionally AMQW structures.

7. CHAPTER 7 - CONCLUSION

7.1 Suggestions for Future Work

AMQW lasers are highly interesting devices and we have only begun to understand their operation and exploit them for experimental studies of MQW laser physics and applications such as broadly tunable lasers. A great deal more work needs to be done in this field. While there is a lot to do, some work has already been begun and substantial progress has been made. In this section I describe some of the many possible AMQW laser projects which may be pursued in the future.

7.1.1 Comprehensive Modeling

In chapter 4 I reported an ambipolar rate equation and gain model which is capable of fitting our TCL data from thirteen different AMQW laser structures. The model is however a first attempt and there is much room for improvement. Here I will outline the approach that I believe should be taken to develop a more comprehensive model.

First, the optical model must be improved. I have used a simple rate equation model. Such a model does not does not properly account for the amplification of spontaneous emission. A Fabry-Perot amplified spontaneous emission model should be developed for AMQW lasers similar to [60,61,62]. Such a model requires gain and spontaneous emission spectra which can be calculated for a given carrier density as I have done.

Once the optical problem is treated properly the electrical currents into and out of the well must be modeled. I believe the relations between carrier capture and escape times presented in chapter 5 should be used. It would be interesting to examine the assumption of a single quasi-

Fermi level for the 2-D and 3-D states below and above threshold. I predict that above threshold the assumption of a single quasi-Fermi level will not be a good approximation to reality.

The carrier capture and escape relations given in chapter 5 link the carrier densities in the 2-D and 3-D states of a QW. The final aspect of the model that must be improved is the determination of the 3-D carrier densities. A Poisson/continuity equation solver must be developed to determine properly the carrier densities throughout the active region. It is critical that the Poisson solver include the charges of the dopant ions and hence the transition regions of the p-i-n junction.

7.1.2 Applications

We have stated that broad gain peak AMQW lasers may be well suited to many applications such as multiple trace gas detection, trace liquid detection and generating short pulses. AMQW lasers have already been used to perform trace gas detection across a wide tuning range [28]. Our original interest in AMQW lasers was to produce a broadly tunable source for trace liquid detection. Trace liquid detection should be feasible using nearly the same experimental apparatus used to demonstrate trace gas detection (i.e., a DOE external cavity AMQW laser). It would also be interesting to attempt second harmonic detection of a liquid using a DOE external cavity AMQW laser. To perform such an experiment one should first cleave the AMQW laser to a cavity length just shorter than the TCL. This will enable single mode tuning over the entire gain peak. The DOE will need to be mounted on a positioner which allows the DOE to be slowly scanned approximately 500 to 1000 μm along the optic axis of the external cavity while being modulated ± 50 to 100 μm along the optic axis at a few hundred Hz. Note that the laser will mode hop when the DOE is modulated over these ranges however, because the

absorption lines of liquids are so spectrally broad, mode hops on the order of a nanometer do not constitute significant jumps in wavelength. As a result trace liquid detection may prove to be less critically dependent on the alignment of the external cavity and laser wavelength stabilization than trace gas detection.

Broad gain peak lasers may also be an excellent gain medium for mode locked short pulse lasers. Wallace *et. al.* [27] have attempted to use an AMQW structure for this purpose. However, the design parameters described in chapter 6 for producing broad gain peak tunable lasers should also apply to short pulse mode locked lasers. The devices need to be designed so that under the operating conditions of the mode locked laser cavity equal contributions are obtained from the QWs of varying thickness/composition. A great deal of engineering needs to be done to determine the potential of AMQW lasers for this application.

In addition to broad gain peak laser applications AMQW structures also have potential uses as spectrally broad light emitting diodes (LEDs), superluminescent diodes (SLDs) and semiconductor optical amplifiers (SOAs). By varying the numbers of QWs, their emission wavelengths, and relative strengths it should be possible to not only make spectrally broad LEDs, SLDs, and SOAs but to engineer the spectral shape of the output.

7.1.3 Tunable Lasers

In chapter 6 we laid out the design criteria for broadly tunable AMQW lasers and showed, theoretically, the potential for making structures with very broad gain peaks. Now that we have an understanding of the design criteria many possibilities exist for making practical broadly tunable lasers. Broadly tunable laser sources are of great interest in industry today and AMQW technology has the potential to play a significant role in industrial products.

There are many possible ways to develop AMQW technology to enter the broadly tunable laser market. One approach is as follows. The first step is to experimentally verify the potential of compositionally AMQW structures predicted in chapter 6. If the experimental structures perform as predicted by our model then we can design a structure for a specific application having a specific tuning range. The structure should be designed accounting for AR coatings or tilted facets as these will be a necessity in a commercial device where side mode suppression ratios of 40 or 50 dB are desired. The reproducibility of the devices must also be determined. For example a target tuning range from 1.29 μm to 1.57 μm could be set to cover both telecom windows. A CAMQW structure could then be designed to have a gain peak reaching from 1.27 μm to 1.59 μm at some predetermined cavity length (assuming, for example, tilted facets and a specific pumping level). The width of the gain peak should be over designed to allow some tolerance at the edges of the desired tuning range. Several wafers should be grown and processed into tilted stripe devices of the predesigned cavity length and tested in external cavities to determine the reproducibility of the tuning ranges. If the tuning range of the devices consistently encompasses the entire specified tuning range then the design can be patented and sold.

AMQW structures can be designed to have customized gain profiles which need not be simply broad and flat such as is desirable for broadly tunable devices. For example a device can be designed to have separate gain peaks at 1.31 μm and 1.55 μm accessing both telecom windows but having little or no gain in the region between the two windows. Such a gain profile may have applications for switching from one telecom window directly to the other.

It would also be interesting to extend the tuning range as far as possible by increasing the wavelength spacing between the different QWs, increasing the number of different transition

energies and applying optimised AR coatings. The transition energies can be spaced further apart when an AR coating is applied as the external cavity feedback is stronger allowing single mode lasing to be obtained further from the gain peak. The tuning range may be extended dramatically by combining AR coating design with active region design.

Another interesting project would be to design split contact AMQW devices capable of switching from operation on one transition to another simply by changing the applied bias on the control contact. The total cavity length (pump region and control region combined) should be slightly longer than TCL for the structure. When both sections are pumped such a device will operate on the long wavelength transition. Decreasing the current in the control section will increase cavity loss which has the same effect on the gain spectrum as going to a shorter cavity length. Hence the thin wells should reach threshold and eventually operate on their own.

7.1.4 New Studies Using the TCL Method

We have developed the TCL method which is a quantitative experimental technique for studying the non-uniform carrier distribution in MQW lasers. The TCL method has provided new experimental data on the non-uniform carrier distribution. We have studied the effect of barrier height and barrier thickness on the non-uniform carrier distribution as well as the degree to which the non-uniform carrier distribution affects devices with different numbers of QWs. Many more experimental studies can be done using the TCL method. Little quantitative experimental data on the non-uniform carrier distribution exists making studies done using the TCL method new and exciting.

The model presented in chapter 4 assumes that the transition region of the P^+-n junction extends into the MQW region of our devices in order to explain the experimentally observed

dependence of the non-uniform carrier distribution on barrier thickness. The TCL method can be used to test this hypothesis experimentally. I would suggest growing four new structures with the same compositions and dimensions as structures 7 - 10 but with a slightly different doping profile. Either extend the p-doping an additional 700 Å into the SCH or stop the p-doping 1000 Å before the SCH begins. If the model presented in chapter 4 is correct then altering the location of the P^+-n junction will significantly affect the non-uniform carrier distribution. Discontinuing the p-doping 1000 Å prior to the SCH should cause there to no longer be a field across the active region so that the strong dependence on barrier thickness observed using structures 7 - 10 will, according to the model presented in chapter 4, no longer exist. Doping an additional 700 Å into the SCH should, according to our model, make the barrier thickness dependence substantially stronger.

Many experimental studies can be designed to examine the effects of different doping profiles, different SCH dimensions and different QW and barrier dimensions and compositions. When designing structures to be used for TCL experiments it is absolutely critical that the devices be designed to have a TCL. If the wavelength separation between two transitions is large then the long wavelength transition will be absorbing at the wavelengths corresponding to the high energy transition. The high energy QWs must then be designed to produce enough gain to be able to overcome the absorption of the low energy transition QWs and reach threshold or else the low energy wells will always dominate and the TCL will not exist. For example, in chapter 4, Fig. 4-5 we demonstrated the origin of the TCL using structure 7 and assuming a uniform carrier distribution. In Fig. 4-5 the thin QWs take over for high carrier densities because they are adding to the gain of the thick QWs. If the wavelengths were separated further then the thick QWs

would still be absorbing at wavelengths corresponding to the thin QWs and the gain peak would not switch to the thin QWs.

7.1.5 Other Methods for Studying the Non-uniform Carrier Distribution

The TCL method has provided quantitative experimental information about the degree to which the non-uniform carrier distribution affects the net gain of QWs at different locations in the active region. To the best of my knowledge the TCL method is the only existing experimental technique for quantitatively studying the non-uniform carrier distribution. Since the development of the TCL method two new methods have been suggested/attempted for directly experimentally studying the non-uniform carrier distribution.

The first technique has not yet been experimentally implemented but was suggested by Ban *et. al.* [63] at CLEO 2000. The technique does not involve AMQW structures or mirror image structures. Ban *et. al.* [63] have suggested that the ratio of TE and TM light emitted from a conventional MQW device could be used to study the non-uniform carrier distribution as the two optical modes provide spatially different samples of the gain in the active region. It would be interesting to perform such an experiment on the AMQW structures we have tested to see if the two methods yield similar experimental results.

The second technique involves measuring the electroluminescence (EL) from mirror image AMQW structures. Newell *et. al.* [23] examined the electroluminescence emitted from the top of two mirror image AMQW laser structures. Using a spontaneous emission model Newell *et. al.* [23] fit to the EL spectra measured from the top of the two mirror image structures at a single cavity length and applied bias current. They fit the two structures independently. QW carrier density was used as a fitting parameter and extracted from the fits for each structure

independently. The method presented by Newell *et. al.* [23] is not a comparative method meaning two structures are fit independently and the two mirror image structures are not compared in order to extract the carrier density. A non-comparative approach of this type has the advantage that the mirror image structure is unnecessary so that less growth and processing are required to carrier out an experimental study. Non-comparative studies do however have two distinct disadvantages. First, extracting the carrier distribution from the experimental data must be done using a theoretical model and the results are dependent on the validity of the model. Second, the results extracted from the data are dependent on the accuracy with which the devices are fabricated or the accuracy with which structural parameters can be measured. In my opinion it is best to use a comparative experimental technique so that the results are independent of theoretical work and only dependent on the relative values of material parameters.

Newell *et. al.* [23] showed that the electroluminescence spectra measured from the top of AMQW lasers are substantially different for mirror image structures with the same cavity lengths and bias currents. This difference in EL emitted from the top of mirror image AMQW structures may be used to develop a comparative experimental technique for studying the non-uniform carrier distribution. Such an approach may have several advantages over the TCL method. One advantage is that EL is being measured instead of laser threshold so it may be possible to carry out carrier density studies by fabricating LEDs instead of lasers which requires fewer processing steps. EL studies may allow one to measure the non-uniform carrier distribution at different applied biases for the same device. Experimental data of this type would provide an excellent test for theoretical Poisson/continuity equation solvers and other carrier transport models.

7.1.6 Properties

Many of the observed properties of AMQW lasers are still not well understood. The above threshold characteristics need to be studied more extensively experimentally. The above threshold characteristics also need to be modeled and explanations must be developed for the interesting switching and simultaneous lasing behaviour we have observed.

AMQW lasers have not been tested under high speed modulation conditions. The high speed modulation properties of these devices need to be studied experimentally. AMQW lasers may provide a new means of studying the physics of MQW lasers under high speed modulation.

7.2 Conclusion

After four years of working with AMQW lasers I can say that they are fascinating devices. Under certain conditions they exhibit interesting above threshold spectral properties such as large shifts in lasing wavelength, lasing on modes across a wide range of wavelengths, and what appears to be simultaneous lasing on transitions of different energies. These above threshold properties are not yet well understood but explaining them will no doubt lead to a deeper understanding of the operation of MQW lasers and in addition these properties may prove useful in future applications. One could for example envision a device with a DFB grating of two different periods which operates on either of two wavelengths depending on the control current or temperature.

The QWs of different thickness and/or composition in AMQW lasers in general emit at different wavelengths making them distinguishable. This property of AMQW lasers makes them useful for experimentally probing the physical properties of MQW active regions. In this thesis we have demonstrated one approach to studying the non-uniform carrier distribution using

AMQW lasers. The TCL method has already provided experimental data on the non-uniform carrier distribution and provided information not previously available nor predicted. The potential studies that could be carried out using the TCL method are endless. But the TCL method is only one possible technique and other methods may be developed which employ AMQW lasers to study not only the non-uniform carrier distribution and its dependencies, but other properties of MQW lasers.

If designed properly AMQW lasers can have very broad gain and spontaneous emission spectra. There is currently a great deal of interest in manufacturing broadly tunable lasers for testing wavelength division multiplexed (WDM) systems in the telecommunications industry. AMQW lasers have the potential to be the key component in the next generation of commercially available broadly tunable lasers. There are many degrees of freedom in the design of AMQW lasers which allow one to create extremely broad gain peaks and tailor the shape of the gain profile and spontaneous emission spectrum to specific applications.

In my opinion the most important result of this thesis is that the behaviour of AMQW lasers varies greatly with cavity length and cavity loss. An understanding of the dependence of AMQW lasers on cavity length and cavity loss is critical when designing experiments which employ AMQW lasers to probe the physics of the active region, designing broadly tunable AMQW lasers, and observing, studying, or exploiting the above threshold wavelength shifts and simultaneous lasing we have observed.

8. APPENDIX I

Here the raw data for threshold current and wavelength are presented. All cavity lengths are in μm, currents are in mA and wavelengths are in nm.

Structure 1													
Lcav	Laser #	1	2	3	4	5	6	7	8	9	10	11	12
400	I	79.7	103	91.6	96.9	106.4	105	82.5					
	lambda	1456	1452	1456	1457	1456	1455	1458					
500	I	89	82	76.4	76	79.5	79.3	122	83.9	86	83.5	83	85.8
	lambda	1465	1464	1465	1465	1466	1466	1466	1466	1464	1466	1466	1465
600	I		57.5	63.5	59.5	58.2	62	59.6	75				
	lambda		1514	1514	1515	1515	1512	1513	1507				
	I2	133		238			112	181					
	lambda2	1459		1460			1463	1461					
700	I	53.6	53.2	50.3	50	53.3	55.7	53.7	51.9				
	lambda	1521	1520	1521	1521	1520	1519	1521	1521				
	I2	181.5	179.8	199.2	195	178		184.1	192.9				
	lambda2	1470	1471	1471	1472	1473		1481	1485				
1000	I	71.9	78	58.4	55.8	58.4	57.6	54.8	58.3				
	lambda	1539	1540	1537	1537	1537	1538	1537	1535				

Structure 2											
Lcav	Laser #	1	2	3	4	5	6	7	8	9	10
500	I	145.2	125.5	155.6	97.6	117.6	119	124.7	137.2	116.5	142.9
	lambda	1472	1469	1457	1460	1456	1457	1457	1458	1459	1459
1000	I	235.7	247.8	239.9	226.8	246.3	243.6	242	240.9		
	lambda	1491	1491	1490	1491	1491	1493	1492	1492		
1200	I	234	197	168.5	166	174	137.8	133	189.2	180.3	
	lambdath	1522	1522	1521	1521	1522	1522	1521	1521	1523	
	lambda	1490	1488	1486	1490	1488	1489	1489	1491	1495	
1400	I	183.5	185	171.6	177.6	173.4	197.9	232.1			
	lambda	1525	1524	1523	1524	1524	1523	1517			

Structure 3												
Lcav	Laser #	1	2	3	4	5	6	7	8	9	10	11
600	I	87.4	75.2	72.3	68.5	71.4	73.9	71.3	74.8	128.3	72.2	70.4
	lambda	1462	1462	1463	1463	1463	1462	1462	1461	1462	1462	1462
800	I	80.8	76.8	74.5	79.6	90.3	82.9	Immediate shift - right at TCL				
	lambdath	1480	1486	1488	1486	1472	1483					
	lambda	1473	1473	1477	1474	1472	1470					
1000	I	86.9	90.7	76.9	92.7	75.5	73.1	76	71.8	72.6	shift to 1475	
	lambda	1501	1496	1498	1492	1499	1499	1501	1500	1500		
1200	I	79.8	70.8	73.1	75.8	72.3	73.4	75.3	74.1	76.3	88.3	76.6
	lambda	1503	1503	1503	1503	1503	1503	1503	1503	1503	1502	1504
1400	I	79.7	75.7	78.3	69.4	70.1	69.5	70.4	69.6	88.5	71.4	73.2
	lambda	1505	1505	1507	1505	1506	1505	1505	1506	1506	1506	1506

Structure 4													
	Laser #	1	2	3	4	5	6	7	8	9	10	11	12
500	I	84.5	84	85.7	87.9	88.7							
	lambda	1451	1453	1451	1449	1449							
800	I	119.4	119.6	104.2	104.3	109.7	96.7	141.7	118.5	130			
	lambda	1461	1460	1463	1463	1463	1466	1461	1464	1463			
1000	I	130	107.3	103.4	102.7	114	105.8	108.1	112.6	107.2			
	lambda	1469	1484	1488	1484	1475	1481	1481	1478	1485			
	lambda2	43	755.4	755.4									
1200	I	111.1	99.4	98.3	97.7	99.5	100.9	106.9	100	97.3	104.9	103.7	103.7
	lambda	1493	1496	1496	1496	1496	1497	1497	1496	1498	1496	1497	1496
	I2	235.9	230	235.8		251			249.3	250.3	246.8	251	232.8
	lambda2	1458	1459	1461		1464			1464	1465	1465	1456	1462
1400	I	135	200	124	128								
	lambda	1493	1473	1500	1500								

Structure 5												
Lcav	Laser #	1	2	3	4	5	6	7	8	9	10	11
1000	I	100	92	89.6	93.3	89	92.1	96.6	99.6			
	lambda	1542	1541	1541	1541	1540	1540	1542	1542			
1500	I	101.2	108	124.6	107.4	128.2	114.9	107.9	119.4	105.2		
	lambda	1552	1552	1547	1553	1549	1552	1553	1552	1552		
1700	I	127.5	127.3	125.8	119.3	126.7	148.7					
	lambda	1560	1560	1556	1569	1556	1563					
1900	I	107.9	102.9	116.4	93.4	94	simultaneous lasing					
	lambda	1593	1592	1595	1598	1597						
2000	I	125.3	93.1	100.4	115.6							
	lambda	1599	1605	1601	1598							
	I2	219	183.2	165.7								
	lambda2	1555	1552	1554								
2400	I	106.6	109	102.2	103.5	98.6	105.5					
	lambda	1608	1606	1607	1604	1606	1606					
	I2	216.3	242.3	249.8		230.7	224.7					
	lambda2	1563	1560	1562		1568	1568					
3000	I	113	131.4	96.8	103.1	103.4	102.6	102.6	100	104.2	105.4	106.8
	lambda	1612	1612	1610	1610	1610	1610	1611	1610	1613	1610	1610

Structure 6													
Lcav	Laser #	1	2	3	4	5	6	7	8	9	10	11	12
1000	I	79.8	75.4	71.5	69.6	69.9	66	65.8	71.2	65.2	63.4	65.1	65.2
	lambda	1538	1537	1536	1535	1537	1535	1535	1536	1535	1536	1535	1535
1500	I	84.6	83.8	82.8	86.9	86.7	94.9	86.2	84.7	126.9			
	lambda	1545	1541	1544	1543	1544	1545	1544	1544	1544			
2000	I	154.1	104.4	95.4	93.9	119	100						
	lambda	1538	1556	1555	1556	1552	1555						
2200	I	103.4	191.7	120	102	103.3							
	lambda	1555	1539	1557	1558	1560							
2400	I	109.7	106	103.7	102.8	116.4	immediate shift						
	lambda	1596	1596	1599	1598	1609							
3000	I	120.2	142.4	109.5	107.7	114.9	112.5	120.4	127.7				
	lambda	1601	1593	1602	1602	1603	1603	1603	1593				
	I2	215.2	158.6	236.7	237.1	239.8	237.2	237.8					
	lambda2	1550	1561	1553	1554	1552	1554	1552					

Structure 7												
Lcav	Laser #	1	2	3	4	5	6	7	8	9	10	11
500	I	103	100.4									
	lambda	1565	1565									
600	I	62	75.5	51	63.2							
	lambda	1614	1605	1612	1619							
1000	I	53.7	52.8	52	48.4	61.3	51.5	50.1	53.1	53.3	100.2	89.8
	lambda	1625	1625	1623	1624	1626	1628	1626	1626	1626	1626	1628

Structure 8						
Lcav	Laser #	1	2	3	4	5
500	I	110.6	68	65.4	75.6	65.6
	lambda	1559	1554	1553	1553	1552
800	I	86.5	91.4	82.6	81.6	
	lambda	1568	1568	1569	1567	
900	I	83.2	84.1	86.1	84.8	
	lambda	1572	1570	1572	1571	
1000	I	92.3	93.8	92	Shift above threshold	
	lambda	1603	1602	1602		

Structure 9										
Lcav	Laser #	1	2	3	4	5	6	7	8	9
500	I	91.7	110							
	lambda	1576	1569							
600	I	67	73.7	104	89.7	104	102.5	126.7		
	lambda	1610	1608	1598	1618	1598	1599	1595		
700	I	81.2	76.2	72.2	73.4	107.6	83.3	99	119.3	
	lambda	1616	1619	1619	1619	1615	1621	1618	1617	
800	I	66.6	71.9	74.9	82.2	80.5	103.7	128.5	124.1	
	lambda	1623	1621	1619	1621	1623	1623	1625	1624	
	I2				265					
	lambda2				1582					
900	I	68.7	74.1	79.4	88.4	99.5	124.3	114.9	134.2	131.1
	lambda	1625	1627	1628	1627	1630	1631	1629	1630	1630

Structure 10											
Lcav	Laser #	1	2	3	4	5	6	7	8	9	10
400	I	60	53.1	57.7	57.2	60.7	56.4	58.3	58.1	64.1	
	lambda	1543	1543	1543	1542	1542	1543	1542	1542	1543	
500	I	58.8	54.4	54	87.6	80	86	60.2	62.3	57.3	55.7
	lambda	1545	1548	1548	1541	1535	1539	1545	1545	1547	1547
600	I	114	85.8	61.4	75.6	97.8	125	66.9			
	lambda	1544	1534	1560	1534	1546	1543	1554			
700	I	91.5	61.7	58.7	57.9	93.9	76	91	58.3	65.8	102.9
	lambda	1556	1601	1603	1601	1547	1561	1556	1600	1599	1539
800	I	55.1	55.6	55.6	57.3	57.8	55.2	55.4	108		
	lambda	1607	1607	1608	1608	1607	1607	1607	1558		
900	I	54	54.9	54.1	54.4	58.2	57.7	57.1	57	62.8	
	lambda	1611	1611	1611	1611	1610	1611	1611	1610	1609	
	I2			120.3							
	lambda2			1580							
1000	I	55.7	56.3	55.3	56.9	55.1	54.5	55.9			
	lambda	1613	1613	1613	1613	1612	1613	1614			

Structure 11									
Lcav	Laser #	1	2	3	4	5	6	7	8
600	I	94							
	lambda	1613							
700	I	70.4	91.9	103.5					
	lambda	1615	1621	1608					
800	I	140							
	lambda	1624							
900	I	99	92.6	116	132.6				
	lambda	1628	1626	1626	1627				
1000	I	76.5	82.8	90.4	94.7	101.5	122.9	124.8	118.8
	lambda	1626	1626	1628	1627	1629	1630	1630	1628

Structure 12										
Lcav	Laser #	1	2	3	4	5	6	7	8	9
400	I	58.2	61.7	57.1	70.2	74.2	68.9	64.9	68	
	lambda	1547	1547	1545	1546	1544	1545	1545	1547	
500	I	64.3	69	105	57.4	61.6	68.6	61.2	67.1	68.1
	lambda	1566	1557	1545	1569	1567	1560	1570	1566	1566
600	I	52.1	56.2	55.4	98.7	53.4	52	53.1	60.7	
	lambda	1591	1587	1588	1566	1589	1591	1590	1586	
700	I	65.8	52.2	50.8	50	50.9	50.3	51.4	54.7	
	lambda	1581	1601	1600	1600	1600	1600	1601	1599	
800	I	51.7	47.2	48.4	49.1					
	lambda	1609	1608	1609	1609					
	l2	209.3	192	212	149.4					
	lambda2	1574	1576	1565	1574					
900	I	46.3	46.6	47.6	49.4	47.9	48.2	46.9	60.6	
	lambda	1611	1611	1611	1611	1612	1611	1611	1611	
	l2	135.4	133.5	134.4	124.4	126.1	104	109.2		
	lambda2	1581	1580	1581	1582	1583	1585	1587		
1000	I	50.3	49.6	50.4	48.8	49.4	55	48.9	51.3	
	lambda	1613	1614	1613	1613	1613	1612	1615	1615	

9. APPENDIX II

In this appendix expressions are derived for the conduction band and valence band effective densities of states for the 3-D unconfined states and the n = 1, 2-D confined states in a QW layer. The analysis shown here follows the procedure outlined in Appendix IV of Streetman's text [41] which shows the calculation of the effective density of states for bulk material.

A. Effective Density of States for the 3-D Unconfined States

Fig. A1 shows the density of states for bulk material with bandgap E_{gw} and for the 3-D unconfined states of a QW with a QW material band gap of E_{gw} and a barrier layer band gap of E_{gb}. Zero on the energy axis has been selected to be at the bottom of the conduction band of the QW material. The density of states for the 3-D unconfined states in a QW layer is zero for energies below E_{bm} and is that of bulk material with energy gap E_{gw} for energies greater than E_{bm}. Expressed mathematically,

$$\rho^{3D}(E) = \begin{cases} \dfrac{\sqrt{E}}{2\pi^2}\left(\dfrac{2m^*}{\hbar^2}\right)^{3/2} & E \geq E_{bm} \\ 0 & E < E_{bm} \end{cases} . \qquad \text{(A1)}$$

where m^* is the effective mass, E is the energy, $\hbar$ is Planck's constant, and E_{bm} is the material barrier height for the valence band or conduction band QW. For the valence band $E_{bmv} = 0.6(E_{gb} - E_{gw})$ and for the conduction band $E_{bmc} = 0.4(E_{gb} - E_{gw})$ where E_{gb} is band gap of the barrier material and E_{gw} is the band gap of the well material. Note that $E_{bmc,v}$ are defined differently from $E_{bc,v}$ in Chapter 5. $E_{bmc,v}$ are the energy difference between the energy gap of the QW and barrier

while $E_{bc,v}$ are the energy differences from the n = 1 energy level of the QWs to the tops of the barriers.

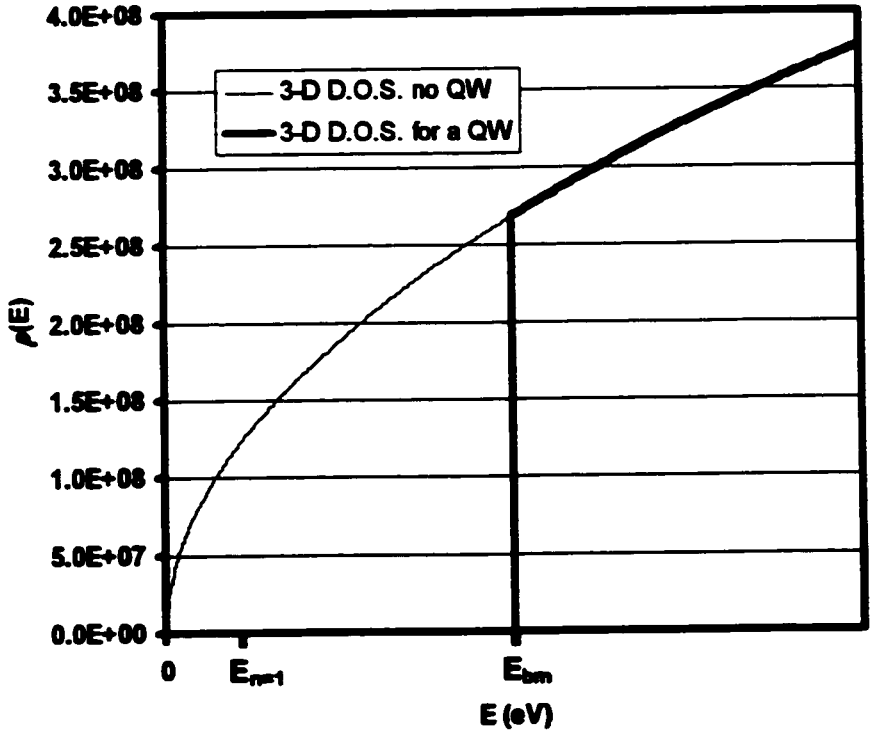

Fig. A1 The density of states for the 3-D unconfined states in a QW.

Next we determine the effective density of states for the 3-D unconfined states in the conduction band of the QW layer. The carrier density in the 3-D unconfined states in the conduction band is given by,

$$n_{3D} = \int_{E_{bc}}^{\infty} \rho^{3D}(E) f(E) dE = \frac{4\pi}{h^3}(2m_c)^{3/2} \exp\left[\frac{E_F}{kT}\right] \int_{E_{bmc}}^{\infty} E^{1/2} \exp\left(-\frac{E}{kT}\right) dE. \qquad (A2)$$

We have approximated the Fermi function f(E) using Eq. 5-12. Performing the integrations gives,

$$n_{3D} = \frac{4\pi}{h^3}(2m_c)^{3/2} \left\{ E_{bmc}^{1/2} kT + \frac{\sqrt{\pi}(kT)^{3/2}}{2} \left[1 - \text{erf}\left(\sqrt{\frac{E_{bmc}}{kT}}\right)\right] \exp\left[\frac{E_{bmc}}{kT}\right] \right\} \exp\left[\frac{E_F - E_{bmc}}{kT}\right]. \qquad (A3)$$

The effective density of states is then defined as,

$$N_{c3D} = \frac{4\pi}{h^3}(2m_c)^{3/2}\left\{E_{bmc}^{1/2}kT + \frac{\sqrt{\pi}(kT)^{3/2}}{2}\left[1 - erf\left(\sqrt{\frac{E_{bmc}}{kT}}\right)\right]exp\left[\frac{E_{bmc}}{kT}\right]\right\}. \quad (A4)$$

A similar analysis for the valence band yields,

$$N_{v3D} = \frac{4\pi}{h^3}(2m_v)^{3/2}\left\{E_{bmv}^{1/2}kT + \frac{\sqrt{\pi}(kT)^{3/2}}{2}\left[1 - erf\left(\sqrt{\frac{E_{bmv}}{kT}}\right)\right]exp\left[\frac{E_{bmv}}{kT}\right]\right\}. \quad (A5)$$

B. Effective Density of States for a Quantum Well

The density of states for the n = 1, 2-D confined states in a QW layer is given by [3],

$$\rho^{2D}(E) = \frac{m^*}{\pi\hbar^2 L_w}. \quad (A6)$$

To determine the conduction band effective density of states for the n = 1, 2-D confined states in the QW layer we begin by writing the carrier density in the conduction band,

$$n_{2D} = \int_{E_{c2D}}^{\infty}\rho^{2D}(E)f(E)dE = \frac{m_c}{\pi\hbar^2 L_w}exp\left[\frac{E_F}{kT}\right]\left[\int_{E_{c2D}}^{\infty}exp\left(-\frac{E}{kT}\right)dE\right]. \quad (A7)$$

We have again approximated the Fermi function f(E) using Eq. 5-12. Performing the integration gives,

$$n_{2D} = \frac{kTm_c}{\pi\hbar^2 L_w}exp\left[\frac{E_F - E_{bc}}{kT}\right]. \quad (A8)$$

The effective density of states is then defined as,

$$N_{c2D} = \frac{kTm_c}{\pi\hbar^2 L_w}. \quad (A9)$$

A similar analysis for the valence band yields,

$$N_{v2D} = \frac{kTm_v}{\pi\hbar^2 L_w}. \tag{A10}$$

C. Ratio of Effective Densities of States

The relation between capture and escape time uses the following ratio of effective densities of states,

$$N_{ratio} = \sqrt{\frac{N_{c2D}N_{v2D}}{N_{c3D}N_{v3D}}}.$$

Let's examine some of the key dependencies of N_{ratio}. First, N_{ratio} is dependent on the QW thickness, L_w. The 3-D effective densities of states have no L_w dependence but the 2-D effective densities of states are proportional to $1/L_w$. Thus N_{ratio} is proportional to $1/L_w$,

$$N_{ratio} \propto \frac{1}{L_w}$$

Also of critical importance is the dependence of N_{ratio} on barrier height. Fig. A2 shows the dependence of N_{ratio} on barrier height. Plotted for comparison are the functions $\exp[-E_{barc}/kT]$ and $\exp[-E_{barv}/kT]$ which approximately give the exponential dependencies with E_{bc} and E_{bv} of Eq. 5-18 and Eq. 5-19. Fig. A2 demonstrates that the exponential dependencies with E_{bc} and E_{bv} of Eq. 5-18 and Eq. 5-19 are much stronger than the dependency of N_{ratio} with E_{bar}.

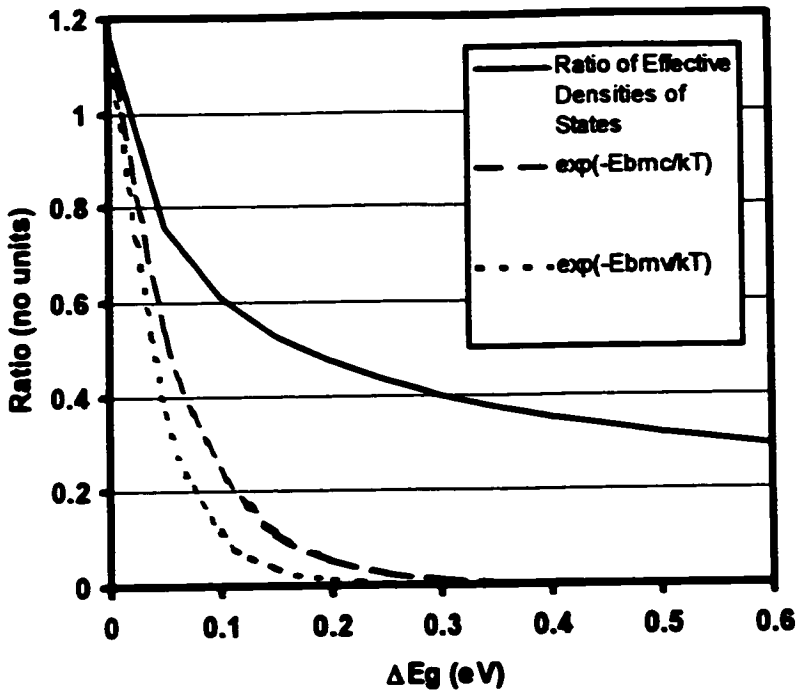

Fig. A2 A plot of N_{ratio} as a function of material barrier height, E_{bm}. Plotted for comparison are exp[-E_{bmc}/kT] and exp[-E_{bmv}/kT].

10. REFERENCES

[1] R. Serway, C. Moses, and C. Moyer, 1989, *Modern Physics*, (Toronto, ON: Harcourt Brace Jovanovich College Publishers).

[2] R. P. Feynman, R. B. Leighton, M. Sands, 1965, *The Feynman Lectures on Physics*, Vol. III, Chapter 16, (Reading, Mass: Addison-Wesley).

[3] S. W. Corzine, R. Yan, L. A. Coldren, 1993, *Quantum Well Lasers*, ed. P. S. Zory Jr., (San Diego, CA: Academic Press).

[4] Milonni, P. W., Eberly, J. H., 1988, *Lasers* (New York, NY: John Wiley & Sons).

[5] Agrawall, Dutta, 1986, *Long Wavelength Semiconductor Lasers*, (New York, NY: Van Nostrand Reinhold Company Inc.).

[6] S. Ikeda, A. Shimizu, T. Hara, "Asymmetric dual quantum well laser-wavelength switching controlled by injection current," *Appl. Phys. Lett.*, vol. 55, pp. 1155-1157, 1989.

[7] S. Ikeda, A. Shimizu, Y. Sekiguchi, M. Hasegawa, K. Kanekop, T. Hara, "Wide-range wavelength tuning of an asymmetric dual quantum well laser with inhomogeneous current injection," *Appl. Phys. Lett.*, vol. 55, pp. 2057-2059, 1989.

[8] S. Ikeda, A. Shimizu, "Evidence of wavelength switching caused by a blocked carrier transport in an asymmetric dual quantum well laser," *Appl. Phys. Lett.*, vol. 59, pp. 504-506, 1991.

[9] A. Shimizu, S. Ikeda, "Theory of asymmetric dual quantum well lasers," *Appl. Phys. Lett.*, vol. 59, pp. 765-767, 1991.

[10] S. Ikeda, A. Shimizu, "Theoretical analysis of dynamic response of asymmetric dual quantum well lasers," *Appl. Phys. Lett.*, vol. 61, pp. 1016-1018, 1992.

[11] P. Evans, P. Blood, J. Roberts, "Carrier distribution in quantum well lasers," *Semicond. Sci. Technol.*, vol. 9, pp. 1740-1743, 1994.

[12] J. Huang, C. Yang, D. Huang, "Carrier capture competition between two different quantum wells in dual-wavelength semiconductor lasers," *IEEE Photon. Technol. Lett.*, vol. 8, pp. 752-754, 1996.

[13] H. Gingrich, D. Chumney, S. Sun, S. Hersee, L. Lester, S. Brueck, "Broadly tunable external cavity laser diodes with staggered thickness multiple quantum wells," *IEEE Photon. Technol. Lett.*, vol. 9, pp. 155-157, 1997.

[14] V. Kononenko, I. Manak, S. Nalivko, V. Shevtsov, D. Shulyaev, "Gain and luminescence spectra of broadband emitters based on asymmetric quantum-well heterostructures," *J. Appl. Spectroscopy*, vol. 64, pp. 234-241, 1997.

[15] T. Krauss, G. Hondromitros, B. Vögele, R. De La Rue, "Broad spectral bandwidth semiconductor lasers," *Electron. Lett.*, vol. 33, pp. 1142-1143, 1997.

[16] H. Yamazaki, A. Tomita, M. Yamaguchi, Y. Sasaki, "Evidence of nonuniform carrier distribution in multiple quantum well lasers," *Appl. Phys. Lett.*, vol. 71, pp. 767-769, 1997.

[17] X. Zhu, D. Cassidy, M. Hamp, D. Thompson, B. Robinson, Q. Zhao, M. Davies, "1.4-μm InGaAsP-InP strained multiple-quantum-well laser for broad-wavelength tunability," *IEEE Photon. Technol. Lett.*, vol. 9, pp. 1202-1204, 1997.

[18] B. Lee, C. Lin, "Wide-range tunable semiconductor lasers using asymmetric dual quantum wells," *IEEE Photon. Technol. Lett.*, vol. 10, pp. 322-324, 1998.

[19] M. J. Hamp, D. T. Cassidy, Q. C. Zhao, B. J. Robinson, D. A. Thompson, M. Davies, J. D. Bewsher, "Analysis of two asymmetric multiquantum well InGaAsP laser structures," *CLEO '98 Technical Digest*, pp. 236-237, 1998.

[20] B. Lee, C. Lin, J. Lai, W. Lin, "Experimental evidence of nonuniform carrier distribution in multiple-quantum-well laser diodes," *Electron. Lett.*, vol. 34, pp. 1230-1231, 1998.

[21] M. J. Hamp, D. T. Cassidy, B. J. Robinson, Q. C. Zhao, D. A. Thompson, M. Davies, "Effect of barrier height on the uneven carrier distribution in asymmetric multiple-quantum-well InGaAsP lasers," *IEEE Photon. Technol. Lett.*, vol. 10, pp. 1380-1382, 1998.

[22] M. J. Hamp, D. T. Cassidy, B. J. Robinson, Q. C. Zhao, D. A. Thompson, "Nonuniform carrier distribution in asymmetric multiple-quantum-well InGaAsP laser structures with different numbers of quantum wells," *Appl. Phys. Lett.*, vol. 74, pp. 744-746, 1999.

[23] T. Newell, M. Wright, H. Hou, L. Lester, "Carrier distribution, spontaneous emission and gain engineering in lasers with nonidentical quantum wells," *IEEE J. Select. Topics Quant. Elect.*, vol. 5, pp. 620-626, 1999.

[24] V. K. Kononenko, I. S. Manak, S. V. Nalivko, "Design and characteristics of widely tunable quantum-well laser diodes," *Spectrochimica Acta A*, vol. 55, pp. 2091-2099, 1999.

[25] M. J. Hamp, D. T. Cassidy, B. J. Robinson, Q. C. Zhao, D. A. Thompson, "Effect of Barrier Thickness on the Carrier Distribution in Asymmetric Multiple Quantum Well InGaAsP Lasers," *IEEE Photon. Technol. Lett.*, vol. 12, pp. 134-136, 2000.

[26] M. J. Hamp, D. T. Cassidy, "Experimental and theoretical study of the influence of quantum barrier thickness on the carrier distribution in InGaAsP MQW lasers," *CLEO 2000 Technical Digest*, pp. 173-174, 2000.

[27] S. Wallace, M. Brennan, P. Mascher, H. Haugen, "Short-pulse asymmetric quantum well InGaAs/InGaAsP/InGaP lasers," *CLEO 2000 Technical Digest*, pp. 181-182, 2000.

[28] S. C. Woodworth, M. J. Hamp, D. T. Cassidy, "Performance of a diffractive optical element external cavity diode laser," *DOMO 2000 Technical Digest*, pp. 60, 2000.

[29] M. J. Hamp, D. T. Cassidy, "Critical design parameters for engineering broadly tunable asymmetric multiple quantum well lasers," *J. Quantum Electron.*, Accepted for publication August, 2000.

[30] M. J. Hamp, D. T. Cassidy, "Experimental and theoretical analysis of the carrier distribution in asymmetric multiple quantum well InGaAsP lasers," *J. Quantum Electron.*, submitted for publication, December, 1999.

[31] M. J. Hamp, D. T. Cassidy, "On carrier capture and escape processes in semiconductor quantum wells," *J. Quantum Electron.*, to be submitted for publication, 2000.

[32] M. J. Hamp, D. T. Cassidy, B. J. Robinson, Q. C. Zhao, D. A. Thompson, "Broad wavelength shifts and simultaneous lasing of wells of different thicknesses in an asymmetric multiple quantum well InGaAsP laser structure," *J. Quantum Electron.*, to be submitted for publication, 2000.

[33] J. F. Hazell, J. G. Simmons, J. D. Evans, C. Blaauw, "The effect of varying barrier height on the operational characteristics of 1.3-μm strained-layer MQW lasers," *IEEE J. Quantum Electron.*, vol. 34, pp. 2358-2363, 1998.

[34] A. Champagne, R. Maciejko, T. Makino, "Enhanced carrier injection efficiency from lateral current injection in multiple-quantum-well DFB lasers," *IEEE Photon. Technol. Lett.*, vol. 8, pp. 749-751, 1996

[35] G. B. Morrison, D. M. Adams, D. T. Cassidy, "Extraction of gain parameters for truncated well gain coupled DFB lasers," *IEEE Photon. Technol. Lett.*, December, 1999

[36] N. Tessler, G. Eisenstein, "On carrier injection and gain dynamics in quantum well lasers," *IEEE J. Quantum Electron.*, vol. 29, pp. 1586-1595, 1993.

[37] R. Nagarajan and J. E. Bowers, 1999, *Semiconductor Lasers I - Fundamentals*, ed. E. Kapon, (San Diego, CA: Academic Press).

[38] P. A. Evans, P. Blood, J. S. Roberts, Semicond. Sci. Technol., vol. 9, pp. 1740-1743, 1994.

[39] S. L. Chuang, 1995, *Physics of Optoelectronic Devices*, (New York, NY: John Wiley & Sons).

[40] "LASTIP reference manual," Crosslight Software Inc., P.O. Box 27102, Gloucester, ON, K1J 9L9, Canada.

[41] B. Streetman, 1995, *Solid State Electronic Devices*, (Upper Saddle River, NJ: Prentice Hall Inc.).

[42] R. P. Feynman, R. B. Leighton, M. Sands, 1965, *The Feynman Lectures on Physics*, Vol. III, Chapter 14, (Reading, Mass: Addison-Wesley).

[43] R. Nagarajan, M. Ishikawa, T. Fukushima, D. S. Geels, J. E. Bowers, "High speed quantum-well lasers and carrier transport effects," *IEEE J. Quantum Electron.*, vol. QE-28, pp. 1990, 1992.

[44] D. A. Kleinman, "The forward characteristic of the PIN diode," *Bell Syst. Tech. J.*, vol. 35, pp. 685, 1956.

[45] N. R. Howard, and G. W. Johnson, "P^+IN^+ silicon diodes at high forward current densities," *Solid State Electron.*, vol. 8, pp. 275-284, 1965.

[46] S. L. Chuang, 1995, *Physics of Optoelectronic Devices*, Appendix K, (New York, NY: John Wiley & Sons).

[47] S. L. Chuang, 1995, *Physics of Optoelectronic Devices*, Chapter 10, (New York, NY: John Wiley & Sons).

[48] S. L. Chuang, 1995, *Physics of Optoelectronic Devices*, Chapter 9, (New York, NY: John Wiley & Sons).

[49] L. A. Coldren, S. W. Corzine, 1995, *Diode Lasers and Photonic Integrated Circuits* (New York, NY: John Wiley & Sons).

[50] S. L. Chuang, 1995, *Physics of Optoelectronic Devices*, Chapter 7, (New York, NY: John Wiley & Sons).

[51] S. L. Chuang, 1995, *Physics of Optoelectronic Devices*, Chapter 2, (New York, NY: John Wiley & Sons).

[52] T. Fukushima, T. Namegaya, Y. Ikegami, H. Nakayama, N. Matsumoto, A. Kasukawa, M. Shibata, "Carrier transport and its effect on the turn-on delay time in strained GaInAsP/InP multiple quantum well lasers," *Optical Quant. Electronics*, vol. 26, pp. S843-S855, 1994.

[53] H. Schneider, K. v. Klitzing, "Thermionic emission and Gaussian transport of holes in a GaAs/$Al_xGa_{1-x}As$ multiple-quantum-well structure," *Phys. Rev. B*, vol. 38, pp. 6160, 1988.

[54] N. Tessler, R. Nagar, D. Abraham, G. Eisenstein, U. Koren, G. Raybon, "Coupling between barrier and quantum well energy states in a multiple quantum well optical amplifier," *Appl. Phys. Lett.*, vol. 60, pp. 665-667, 1992.

[55] T. Ishikawa, R. Nagarajan and J. E. Bowers, "Analysis of the effects of doping and barrier design on the small-signal modulation characteristics of long wavelength multiple quantum well lasers," *Optical Quant. Electronics*, vol. 26, pp. S805-S816, 1994.

[56] X. Zhu and D. T. Cassidy, "Liquid detection using InGaAsP semiconductor lasers with multiple short external cavities," *Appl. Opt.*, vol. 35, pp. 4689-4693, 1996.

[57] D. Mehuys, M. Mittelstein, A. Yariv, R Sarfaty, J. E. Ungar, "Optimized Fabry-Perot (AlGa)As quantum-well lasers tunable over 105 nm," *Electron. Lett.*, vol. 25, pp. 143-145, 1989.

[58] H. Tabuchi, H. Ishikawa, "External grating tunable MQW laser with wide tuning range of 240 nm," *Electron. Lett.*, vol. 26, pp. 742-743, 1990.

[59] D. T. Cassidy, M. J. Hamp, "Diffractive optical element used in an external feedback configurations to tune the wavelength of uncoated Fabry-Pérot diode lasers," *J. Mod. Opt.*, vol. 46, pp. 1071-1078, 1999.

[60] D. T. Cassidy, "Comparison of rate-equation and Fabry-Perot approaches to modeling a diode laser," *J. Appl. Opt.*, vol. 22, pp. 3321-3326, 1983.

[61] D. T. Cassidy, "Analytic description of a homogeneously broadened injection laser," *IEEE J. Quantum Electron.*, vol. QE-20, pp. 913-918, 1984.

[62] G. B. Morrison, D. T. Cassidy, "A probability-amplitude transfer matrix model for distributed-feedback laser structures," *IEEE J. Quantum Electron.*, vol. QE-36, pp. 633-640, 2000.

[63] D. Ban, E. H. Sargent, "Polaraization-dependence in multiquantum well lasers and semiconductor optical amplifiers: probing interwell transport effects," *CLEO 2000 Technical Digest*, pp. 179, 2000.